Max-Planck-Institut für Polymerforschung

Max Planck Institute for Polymer Research

Silver Sulfide Compounds, Their Optical and Mechanical Properties and Charge Carrier Dynamics

Dissertation

Zur Erlangung des Grades

"Doktor der Naturwissenschaften" (Dr. rer. nat.)

im Promotionsfach Chemie

am Fachbereich Chemie, Pharmazie, Geographie und Geowissenschaften

der Johannes Gutenberg-Universität in Mainz

Junren Wang

geboren in Liaoning, China

Mainz, 2021

Diese Arbeit wurde in der Zeit von September 2018 bis November 2021 am Max-Planck-Institut für Polymerforschung unter der Betreuung von Frau Prof. Dr. Katharina Landfester, Herrn Dr. Andreas Riedinger und Herrn Dr. Calum Ferguson durchgeführt.

Erster Gutachterin: Prof. Dr. Katharina Landfester

Zweiter Gutachter: Prof. Dr. Andreas Walther

Erklärung:

Hiermit versichere ich, die vorliegende Arbeit selbstständig und ohne Benutzung anderer als der angegebenen Hilfsmitte angefertigt zu haben. Alle Stellen, die wörtlich oder sinngemäß aus Veröffentlichungen oder anderen Quellen entnommen sind, wurde als solche eindeutig kenntlich gemacht. Diese Arbeit ist in gleicher oder ähnlicher Form noch nicht veröffentlicht und auch keiner anderen Prüfungsbehörde vorgelegt worden.

Junren Wang

Mainz, November 2021

Acknowledgments

Firstly, I would like to express my gratitude towards Prof. Dr. Katharina Landfester for giving me the opportunity to work at the Max Planck Institute for Polymer Research as a doctoral researcher. During my Ph.D. study, she offered critical advice in my research direction, paper writing and created a friendly, colorful, and international working atmosphere. I am also grateful to her for the support for the German courses so that I could expand my knowledge about German culture and relieve some confusion in my daily life.

As for my daily supervisor, Dr. Andreas Riedinger, was always giving me constructive directions on my experiments and taught me how to write a paper. I am deeply grateful to him. I also thank Dr. Calum Ferguson for receiving me in his group and taking me together for his group activities in my last year at MPIP.

I would also like to thank my collaborators who offered me help with my samples in various aspects so that I could approach my subject in different ways. I am grateful especially to Shuai Fui for terahertz measurements and Dr. Hai Wang for terahertz spectroscopy discussions and his assistance and revision on our paper.I am also grateful to Dr. Robert Graf for the NMR measurements and analyses, and Dr. Kaloian Koynov for mechanical property discussions.

The achievements of my Ph.D. study would not be possible without the help of our professional and experienced technicians, Christoph Sieber for TEM training and XRD measurements, Gunnar Glasser for SEM measurements, Michael Steiert for XRD measurements, Katrin Kirchhoff for HRTEM measurements, Petra Räder for DSC measurements, Leon Prädel for XPS measurements, and Andreas Hanewald for tensile tests.

I am glad to have been part of the Landfester group, and I am particularly thankful for the help received by fellow group members Dr. Rebecca Momper, Dr. Henry Halim and Shuai Chen. Their insights, advices and discussions concerned to both my work in the institute and my daily life.

I also want to express my gratitude towards all the members of the AK Landfester during my time in the group. We had many great moments for the past 3 years and I will always remember my time here.

Finally, I would like to thank my parents and grandfather for their support and understanding during my studies in China and especially abroad.

Mainz, November 2021

Junren Wang

List of abbreviations

Atomic force microscopy	AFM
Body centered cubic	BCC
Chemical bath deposition	CBD
Diethylene glycol	DEG
Dimethyl sulfoxide	DMSO
Direct current	DC
Dimethylformamide	DMF
Drude-Smith	DS
Ethylene glycol	EG
Equivalent	eq
Face centered cubic	FCC
Fast Fourier transformation	FFT
Fourier-transform infrared spectroscopy	FTIR
Highest occupied molecular orbital	HOMO
High-resolution transmission electron microscopy	HRTEM
Indium tin oxide	ITO
Ligand-to ligand charge transfer	LLCT
Ligand-to-metal charge transfer	LMCT
Ligand-to-metal-metal charge transfer	LMMCT
Low molecular-weight gelators	LMWGs
Lowest unoccupied molecular orbital	LUMO
Magic angle spinning	MAS
Metal to ligand charge transfer	MLCT
Metal to metal charge transfer	MMCT
3-mercaptopropionic acid	MPA
Nuclear magnetic resonance spectroscopy	NMR
Nanoplatelets	NPLs
Optical pump-THz probe	OPTP

Photoluminescence	PL
Polycarbonate	PC
Phenyl-C61-butyric acid methyl ester	PCBM
Poly(3-hexylthiophen-2,5-diyl)	P3HT
Powder X-Ray diffraction	PXRD
Quantum dots	QDs
Root mean square	RMS
Scanning electron microscopy	SEM
Transition metal chalcogenide	TMC
Transmission electron microscopy	TEM
Three-dimension	3D
Terahertz	THz
X-ray photoelectron spectroscopy	XPS

Content

Zusammenfassung

Silberthiolat-Koordinationspolymere mit vielseitigen Eigenschaften ziehen aufgrund der hohen Tendenz der weichen Lewis-Säure Ag(I) zur Koordination mit dem weichen Lewis-Basen-Schwefel und der unterschiedlichen Koordinationszahlen von Ag(I) viel Aufmerksamkeit auf sich. In dieser Arbeit wurden neue lamellare Silberthiolate (Ag-MPA) mit einzigartigen reversiblen optischen Eigenschaften flexibler Strukturen hergestellt und mittels NMR, XRD, DSC und XPS charakterisiert. Die polymerähnliche Natur von Ag-MPA macht eine Hochskalierung der Reaktion möglich und ermöglicht eine einfache Verarbeitung, kombiniert mit den reversiblen optischen Übergängen, die viele neue Möglichkeiten für Anwendungen von der Bio-Bildgebung bis zur Optoelektronik eröffnen. Darüber hinaus kann bei einer hohen eingesetzte Konzentration Ag-MPA zur Bildung von in situ-Gelierungen führen. Durch weitere Modifikation wurde ein supramolekulares Silberthiolat-Gel mit verbesserter NIR-Fluoreszenz, Ungiftigkeit und guter Wasserlöslichkeit erhalten. Die mechanischen Eigenschaften kann durch die Mischung von Poly(vinylalkohol) verbessert und abgestimmt werden. Dieses starke Biokompatibilitätsgel kann in vielen biomedizinischen Bereichen angewendet werden, wie Wirkstoffabgabe, Bildgebung in vivo, photodynamische Therapie und 3D-Druck.

Dank der guten Wasserlöslichkeit dieses Silberthiolats lässt es sich gleichmäßig auf Substraten verteilen kann, um daraus einen dünnen Film zu bilden. Darüber hinaus lässt sich Silberthiolat-Koordinationspolymerfilem durch thermische Behandlung Silbersulfid herstellen. Daher kann es als ideale Vorstufe zur Herstellung von monoklinen α-Ag_2S-Filmen dienen, einer vielversprechenden Klasse duktiler Übergangsmetallchaldogenide für flexible Optoelektronik und Thermoelektrik. In dieser Arbeit wurde eine nasschemische Synthesestrategie entwickelt, die unterstützte und freistehende α-Ag_2S-Dünnschichten mit lateraler Wafergröße ermöglicht. Mit ultraschneller Terahertz (THz)-Spektroskopie ließ sich verfolgen, dass sich die photogenerierten Ladungsträger in α-Ag_2S-Dünnfilmen einem bandartigen Transportmechanismus mit intrinsisch hoher Mobilität und Diffusionslänge folgen. Diese Ergebnisse ebnen den Weg für die Verwendung von α-Ag_2S-Dünnfilmen als flexible und leitfähige Bausteine für tragbare optoelektronische und thermoelektrische Geräte.

Abstract

Silver thiolates coordination polymers with versatile properties attract a lot of attention due to the high tendency of soft Lewis acid Ag(I) to coordinate with soft Lewis base sulfur and the various coordination number of Ag(I). In this work, new lamellar silver thiolates (Ag-MPA) with unique reversible optical properties and flexibility structures were designed and characterized by NMR, XRD, DSC, and XPS. The polymer-like nature of Ag-MPA makes up-scaling the reaction feasible and allows for facile processing, combined with the reversible optical transitions, which opens up many new possibilities for applications ranging from bio-imaging to optoelectronics. Furthermore, high reacted concentration can lead Ag-MPA to the formation of *in situ* gelations. With further modification, silver thiolate supramolecular gel was obtained with enhanced NIR fluorescence, non-toxicity, and good water solubility. The mechanical properties can be improved and tuned by blending with poly(vinyl alcohol). This strong bio-compatibility gel can be applied in biomedical fields, such as drug delivery, imaging in vivo, photodynamic therapy, and 3D printing.

According to the good water solubility of this silver thiolate, it can distribute uniformly on substrates to form a thin film. Moreover, the stable product after thermal treatment of silver thiolate coordination polymer is silver sulfide. Therefore, it can act as an ideal precursor to prepare monoclinic α-Ag_2S films, a promising ductile transition metal chalcogenide for flexible optoelectronics and thermoelectrics. In this thesis, a solution-processed synthetic strategy enabling supported and free-standing α-Ag_2S thin films with a lateral wafer size was prepared. As evidenced by ultrafast terahertz (THz) spectroscopy, the photogenerated charge carriers migrate in supported α-Ag_2S thin films following band-like transport mechanism, with intrinsically high mobilities and diffusion length. These results pave the way for utilizing α-Ag_2S thin films as flexible and conductive building blocks towards wearable optoelectronic and thermoelectric devices.

1. Introduction

Coordination polymers are hybrid inorganic/organic structures formed by metal cation centers linked by organic ligands in the form of one-, two-, or three-dimensional architectures. The coordination polymers typically have these three characteristics: the center ion acts as Lewis acid with empty electron orbitals; the ligand acts as Lewis base with lone pair electrons; the central ion combines with the ligand to form a coordination entity with a certain composition and spatial configuration. The first manufactured coordination polymer is Prussian Blue, a dark blue pigment synthesized by Diebach in 1704. The correct structure for coordination compounds and the basis for modern coordination chemistry was proposed by Alfred Werner in 1893. Influenced by the nature of the central transition metal ion, different coordination numbers, the metal to ligand ratio and the nature of ligands,[1-2] metal coordination polymers exhibit fascinating structural topologies, ranging from linear, to honeycomb, to square planar, to diamondoid, and polycatenanes.[3-4] In recent decades, coordination polymers were proposed as potential materials for molecular storage, luminescence, catalysis, electrical conductivity, and magnetism.[5]

Due to the hard-soft-acid-base theory, silver as a soft acid tends to coordinate with soft base sulfur and exhibits a high affinity for sulfur. Silver (I) has a flexible coordination number from 2 to 7,[6] and binds strongly to various sulfur compounds, which offer the possibility to design silver-sulfide coordination polymers with desired characteristics, for example photoluminescence. Here, the ligand can tune to metal charge transfer, the metallophilic interaction and the metal-centered electronic states. Compared to other metals, such as copper(I) and gold(I), a relatively small number of publications deals with the luminescence silver (I) coordinate complex.[7,8] The thermal instability and light sensitivity of silver(I) increases the challenging task of such analyses. However, due to the anti-bacterial and biocompatibility of silver(I),[9] designing luminescence and stable silver(I) coordination polymers is still an exciting prospect. Various silver thiolate coordination polymers were synthesized in this work, and their unique optical and rheology properties were studied. Moreover, based on this silver thiolate coordination polymer, high quality thin semiconductor silver sulfide films were prepared, which showed a high photoconductivity.

2. State of the art

This chapter introduces the crystal structure and property of silver sulfide (Section 2.1.1), different coordination states of silver(I) and properties of silver(I) coordination polymers (Section 2.1.2), different kinds of interaction forces of supramolecular gels and polymer gels (Section 2.2), and the principle of charge carrier dynamics resolved by terahertz spectroscopy (Section 2.3).

2.1 Silver sulfide and silver(I) coordination polymer

2.1.1 Ag_2S

In 1833, Michael Faraday discovered that the electrical conductivity of silver sulfide increases with increasing temperature, which is the opposite compared to metallic conductors, where the electrical conductivity decreases with the increasing temperature.[10 11] This is the first observation of one of the defining characteristics of a semiconductor.[12] A semiconductor is a substance with conductivities between an insulator and a conductor with unique properties[13], widely used in electronic devices, optical sensors, and light emitters.[14-15] In the following decades, more important and unique properties of semiconductors were discovered. In 1839, Edmond Becquerel discovered the photovoltaic effect of semiconductors.[16] In 1873, Willoughby Smith discovered the photoconductivity effect of semiconductors.[17] In 1874, Ferdinand Braun observed the rectification effect of semiconductors.[18] Since 1947, three scientists Bardeen, Brattain and Shockley in Bell labs managed to make the first working transistor -- the point-contact transistor.[19] Various new semiconductor devices have been invented with more advanced technology, materials, and applications. In the 1980s, the semiconductor quantum dots (nanocrystals within a few nanometers) were found by Alexey I. Ekimov,[20] which helped achieve high-speed electronic devices and high-performance luminescence detectors, such as quantum dot photovoltaic solar cell and quantum dot display.[21-23] The unique properties of silver sulfide, such as low toxicity, low production cost, narrow band gap, and the tunable luminescence range of Ag_2S quantum dots (QDs) should be explored.[24-27]

2.1.1.1 Crystal forms of Ag_2S

Ag_2S has three polymorphous modifications (α-Ag_2S, β-Ag_2S, and γ-Ag_2S) with significantly different structures and properties.[28-29] At low temperature (below 450 K), acanthite α-Ag_2S exists as a semiconducting phase with a monoclinic crystal structure. Under equilibrium conditions, from 452 to 859 K, argentite β-Ag_2S exists as superionic conductivity with a body-centered cubic (bcc) crystal structure. At high temperatures (from 860 K to melting point 1115K), γ-Ag_2S have a face-centered cubic (fcc) crystal structure. The homogeneity range of Ag_2S is shown in Figure 2.1.[24, 28]

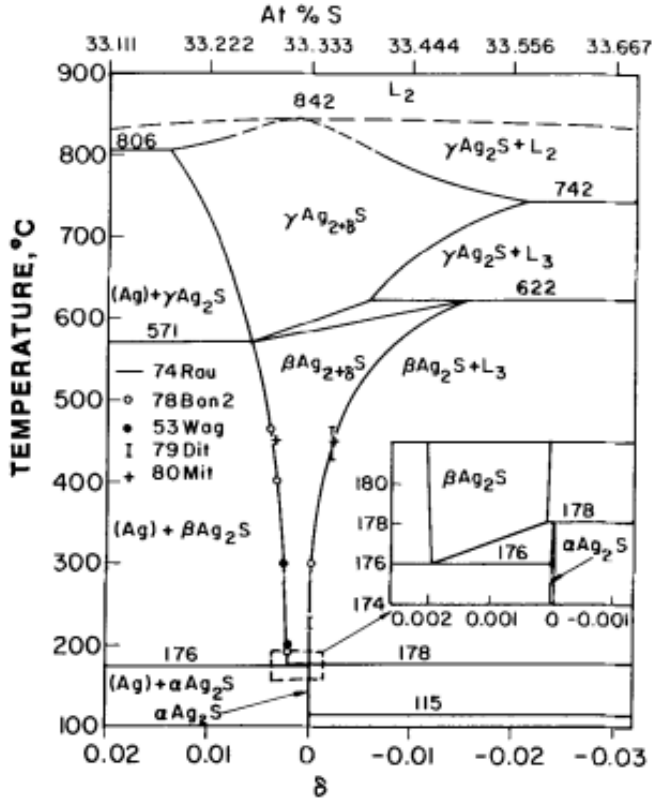

Figure 2.1. Homogeneity range of Ag_2S. Figure is adapted with permission from Bulletin of Alloy Phase Diagrams 1986, 7, 263-269.[28]

The unit cell of α-Ag_2S belongs to the space group $P2_1/c$ with parameters a = 0.4231 nm, b = 0.6930 nm, c = 0.9526 nm and β = 125.5°,[30] the structure is displayed in Figure 2.2.[31] The α-Ag_2S phase is generally to be regarded as stoichiometric, while cubic β-$Ag_{2\pm\delta}S$ and γ-$Ag_{2\pm\delta}S$ ($\delta \tilde{=} 0.002$) is a non-stoichiometric phases. The non-stoichiometric β-$Ag_{2\pm\delta}S$ ($\delta \leq 0.002$) phase has high electronic conductivity of about 1.3×10^5 $S\cdot m^{-1}$, while the α-Ag_2S phase has low electronic

conductivity from 0.09 to 0.16 Sm^{-1} at 300 K.[32-33] According to the report of Sadovnikov et al., Ag_2S nanocrystals with diameter less than 50 nm are non-stoichiometric with ~$Ag_{1.93}S$ composition.[34]

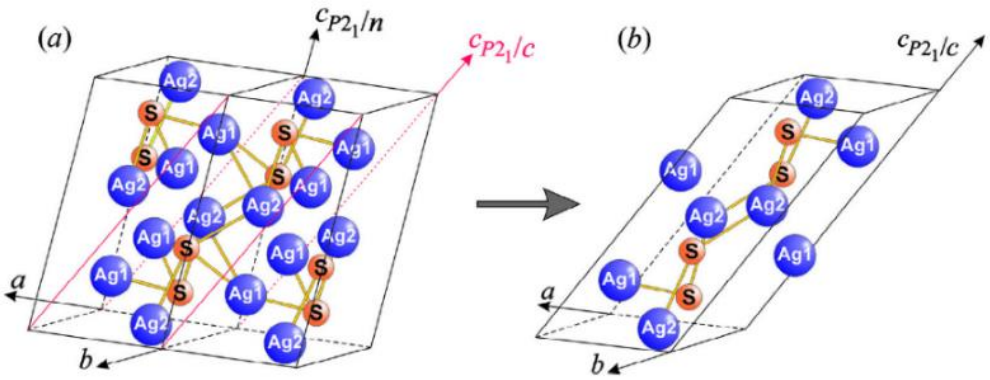

Figure 2.2. The arrangement of Ag and S atoms in α-Ag_2S (space group $P2_1/c$): (a) the contour of doubled unit cell, (b) monoclinic unit cell. The lengths of Ag1-S is 0.2511 nm, and Ag_2-S is 0.2548 nm. Figure is adapted with permission from Superlattices and Microstructures 2015, 83, 35-47.[31]

In another article from Sadovnikov et al.[35], the in-situ acanthite α-Ag_2S - argentite β-Ag_2S phase transformation was explained. When the temperature decreases below 450 K, the β-Ag_2S phase transforms to α-Ag_2S. During the transformation process S atoms in the bcc sublattice will distort to monoclinic sublattice. Silver atoms in the positions of the argentite (bcc) will concentrate in the position of acanthite (monoclinic) (shown in Figure 2.3). The occupations of Ag in α-Ag_2S is almost 1 (shown in Table 2.1).

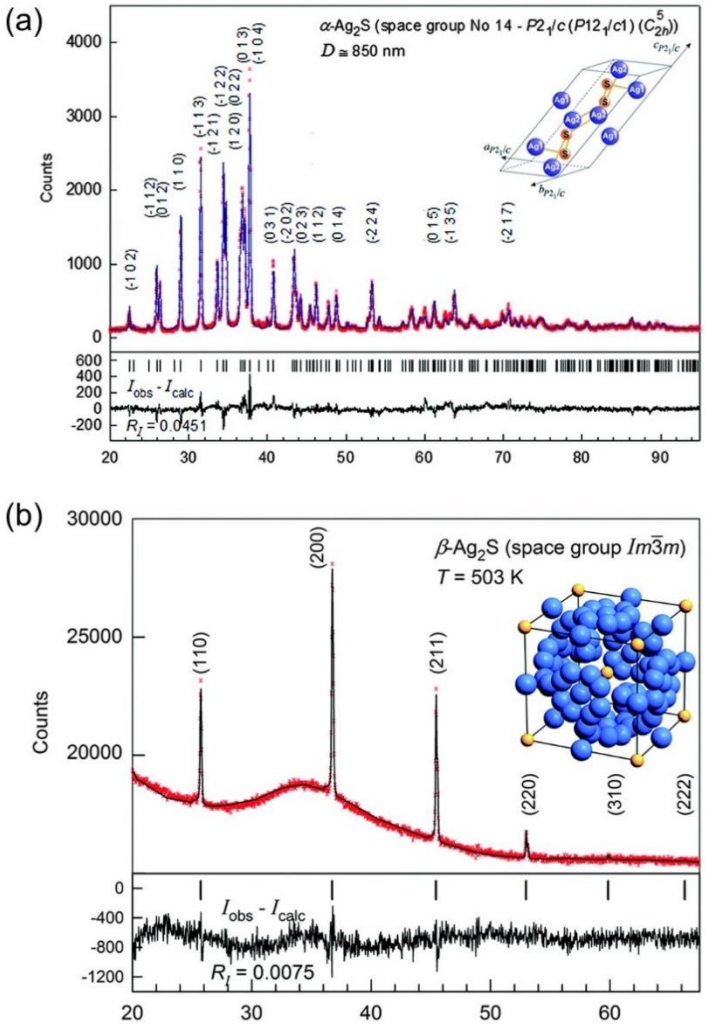

Figure 2.3. (a) The experimental (blue) and calculated (red) XRD patterns of α-Ag_2S (space group $P2_1/c$), the difference between them is shown in the lower spectra. (b) The experimental (blue) and calculated (red) XRD patterns of β -Ag_2S (space group $Im\bar{3}m$), the difference between them is shown in the lower spectra. Figure is adapted and modified with permission from Physical Chemistry Chemical Physics 2015, 17, 20495-20501.[35]

Sadovnikov et al. explained the superionic conductivity of the β-Ag_2S phase as well.[29] When the temperature is above 433 K, Ag_2S exhibits argentite β-Ag_2S phase. However, the occupations of these two positions are very low, 0.0978 and 0.0711 (shown in Table 2.2). Therefore, to maintain the structure's stability, the mobility of Ag or Ag^+ should be very high. Moreover, the vacant site concentration is more than 92%, which provides the possibility of jumping cations. This makes the β-Ag_2S phase a superionic conductor.

Table 2.1. Refined crystal structure of monoclinic (space group No. 14-$P2_1/c(P12_1/c1)$) silver sulfide with α-Ag_2S acanthite type structure: Z = 4, a = 0.42264(2) nm, b = 0.69282(3) nm, c = 0.95317(3) nm, and β = 125.554(2)°.[31]

Atom	Position and multiplicity	Atomic coordinates			Occupancy
		x	y	z	
Ag1	4(e)	0.0715(7)	0.0151(3)	0.3094(3)	1.00
Ag2	4(e)	0.7264(7)	0.3241(4)	0.4375(3)	1.00
S	4(e)	0.492(2)	0.234(1)	0.1321(7)	1.00

Table 2.2. Refined crystal structure of cubic (space group No. 229 – Im3m(I4/m32/m)) silver sulfide with β-Ag2S argentite type structure: Z = 2, $a = b = c$ = 0.4874(1) nm.[29]

Atom	Position and multiplicity	Atomic coordinates			Occupancy
		x	y	z	
Ag1	6(b)	0	0.5	0.5	0.0978(7)
Ag2	48(j)	0	0.3306(5)	0.4122(7)	0.0711(0)
S	2(a)	0	0	0	1.00(0)

Table 2.3. Refined crystal structure of cubic (space group No. 225 –Fm3m(F4/m32/m)) silver sulfide with γ-Ag2S argentite type structure: Z = 4, $a = b = c$ = 0.62831(8) nm.[36]

Atom	Position and multiplicity	Atomic coordinates			Occupancy
		x	y	z	
Ag1	8(c)	0.25	0.25	0.25	0.088(7)
Ag2	32(f)	0.303(4)	0.303(4)	0.303(4)	0.15(1)
Ag3	48(i)	0.5	0.381(4)	0.381(4)	0.027(3)
S	4(a)	0	0	0	1

Similar to the β-Ag_2S phase, the γ-Ag_2S phase also has superionic conductivity. Because in the γ-Ag_2S phase, the occupancies of these positions are 0.88, 0.15, and 0.027,[36] Ag atoms are in constant motion over all possible positions, which provides the superionic conductivity (shown in Table 2.3).

For acanthite-type α-Ag_2S the band gap is ~1 eV at room temperature[37,38], the temperature coefficient is $dE_g/dT = 1.2 \times 10^{-3}$ eV/K. The optical gap changes from 0.85 eV to 0.75 eV at the transition point. For argentite type β-Ag_2S, the temperature coefficient is $dE_g/dT = 3 \times 10^{-4}$ eV/K (shown in Figure 2.4).

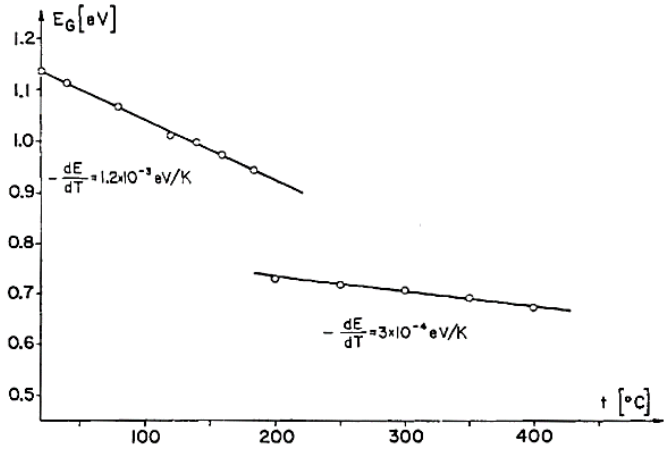

Figure 2.4. Optical absorption of Ag_2S at different temperatures. Figure is adapted with permission from Philosophical Magazine 1977, 36, 941-958.[37]

α-Ag_2S has a small carrier concentration (about 10^{14}-10^{15} cm^{-3}) and a large negative Seebeck coefficient at room temperature. These properties indicate that α-Ag_2S is an intrinsic semiconductor and electrons are the dominant charge carriers (carrier mobility is 86.87 $cm^2V^{-1}s^{-1}$).[32]

2.1.1.2 Ag_2S quantum dots (QDs)

The band gap between conduction band and valence band is a fixed value related to the material for bulk semiconductors.[39] When the size of the material becomes sufficiently tiny (less than ~10 nm), the bandgap increases and more discrete energy levels appear as the size of the nanoparticle decrease, which is known as the quantum confinement effect.[40-41] This phenomenon results when the movement of an exciton is impeded, and the total energy of exciton does not change. Therefore, the required energy increases to create exciton-hole pair when the particle size decreases to the exciton Bohr radius,[42-43] which can be defined as the separation distance between electrons and holes (shown in Figure 2.5). The optical wavelength corresponding to a given bandgap energy E_g can be calculated according to the Planck-Einstein relation.[44]

$$E_g = h\nu = \frac{hc}{\lambda} \qquad Equation\ 2.1$$

c: the speed of light, 3.0×10^8 m/s;

h: Planck's constant, 6.63×10^{-34} J·m.

For semiconductor nanocrystals, also called quantum dots (QDs), the optical wavelength decreases with the decreasing particle size due to the increase of E_g.

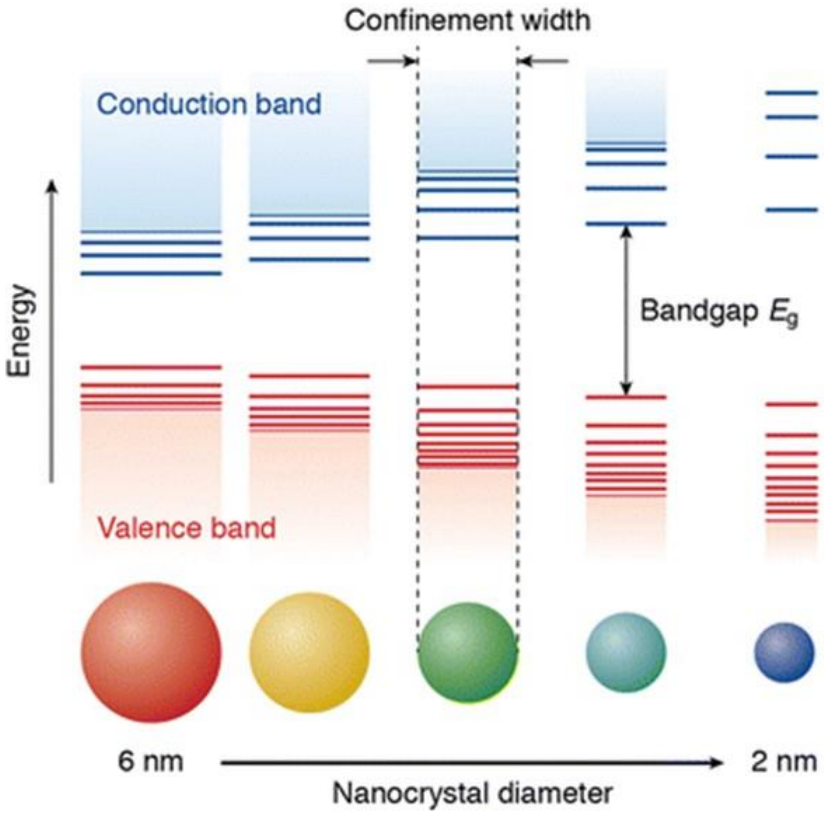

Figure 2.5. Scheme of quantum confinement effect. Figure is adapted with permission from the Photoactive Semiconductor Nanocrystal Quantum Dots 2017, 1-30.[45]

Because of the narrow band gap, high absorption coefficient (~10^4),[46] and low toxicity in organisms[47], Ag_2S QDs are a promising material with near infrared (NIR) emission. Wang's group synthesized Ag_2S QDs with NIR emission in 2010.[48] Their Ag_2S QDs emit at 1058 nm under 785 nm excitation with the size of 10.2 nm. In their further work in 2014, they obtained a series of uniform Ag_2S QDs sizing from 2.4 to 7 nm with emissions from 975 to 1175 nm (as shown in Figure 2.6).[42]

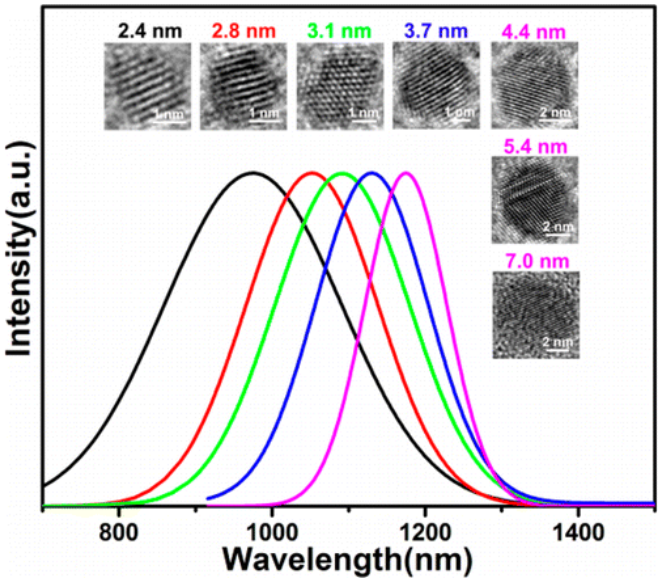

Figure 2.6. PL emission spectra under an excitation of 785 nm and TEM image of different size Ag_2S QDs. Figure is adapted with permission from the Journal of Physical Chemistry C 2014, 118, 4918-4923.[48]

2.1.2 Ag-S coordination polymer

2.1.2.1 Coordination chemistry of silver cations

Silver is the 47th element in the periodic table. Its electron configuration is [Kr]4d^{10}5s^{1}. In group IB, silver has the lowest first ionization energy (731.0 KJ·mol^{-1}) and higher second (2070 KJ·mol^{-1}) and third ionization energy (3361 KJ·mol^{-1}) than copper (1st ionization energy is 745.5 KJ·mol^{-1}, 2nd ionization energy is 1957.9 KJ·mol^{-1}, 3rd ionization energy is 3555 KJ·mol^{-1}) and gold (1st ionization energy is 890.1 KJ·mol^{-1}, 2nd ionization energy is 1980 KJ·mol^{-1}). Because of the low first ionization energy and high second ionization energy, the +1 oxidation state is the predominant state of silver, and the range of the increasing oxidation states is limited. Resulting from its full d-subshell, silver(I) (+1 oxidation state) is stable and tends to form coordination complexes, such as $Ag(NH_3)_2OH$, a typical linear silver coordination complex, where the sp hybridization of Ag^+ forms two hybrid orbitals filled by the electrons of NH_3 molecules. Fox et al. [49] studied the coordination chemistry of silver cations in the mixed solvent system based on the simple water model. The optimized structures of $Ag^+(H_2O)_n$ with n=1-4, derived with the B3LYP method described by Becke[50] are shown in Figure 2.7.

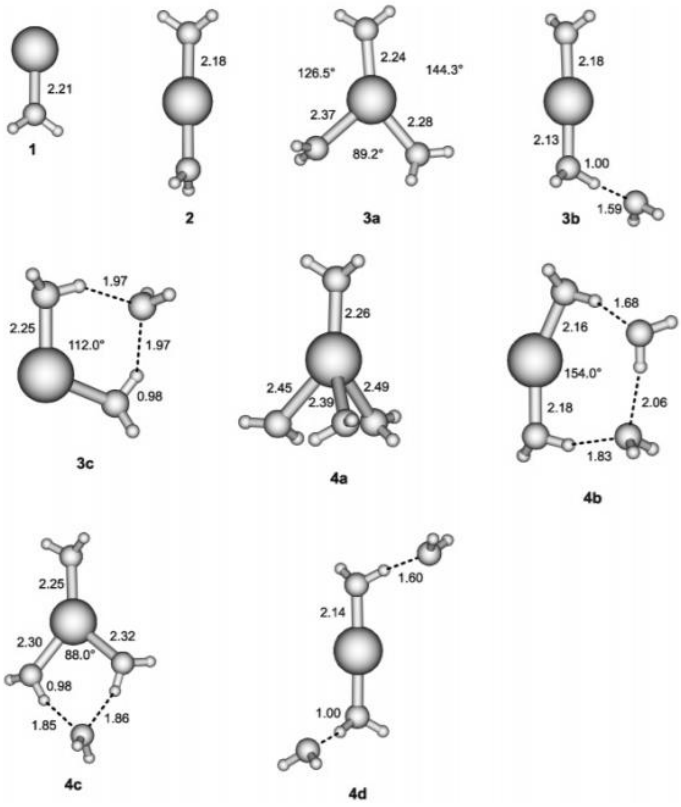

Figure 2.7. Fully optimized structures of $Ag^{+}(H_2O)_n$, n=1-4, derived with the B3LYP model (the three-parameter hybrid Hartee-Fock/density functional). Bond lengths are in Å. Figure is adapted with permission from Journal of the American Chemical Society 2002, 124, 13613-13623.[49]

The most common coordination numbers of silver(I) complexes are two, three, and four.[51-54] A Cambridge Structural Database CSD search yields 3319 crystal of silver(I) coordination complexes.[55] In these reported solid-state structures of silver(I) complexes, 24.2% are two-coordinate, 22.7% are three-coordinate, 43.9% are four-coordinate, 4.7% are five-coordinate, 3.9% are six-coordinate, and the remaining 0.6% have coordination numbers greater than six.[56]

2.1.2.2 Silver(I)-thiolate coordination polymer

Ag(I) exhibits a high affinity for sulfur and can coordinate and complex with various kinds of sulfur sources, such as mercaptans, thioacids, thioethers (single bond to carbon), thioketones, thioamides and dithiocarbamates (double bonded).[57-64] The stability of these complexes are

related to log K_f (stability constant of formation).[65] Table 2.4 shows log K_f for some typical silver(I) complexes. With the value of log K_f ~13, mercaptans have very strong binding. Thioethers have similar log K_f value to amines ~3. The log K_f value of carboxylates are very low.[66] Silver(I)-thiolate coordination polymers exhibit multiple properties, such as luminescence, photothermal, thermochromic and semiconductivity.[67-68]

Table 2.4. Log K_f value for some typical silver-organosulfur, silver-amino and silver-carboxylato complexes. (Table is adapted with permission from the Environmental Toxicology and Chemistry: An International Journal 1999, 18, 9-22.[69])

Compound	pK_f
2-Mercaptoethanol $HOCH_2CH_2SH$	13.2
Cysteine $^-OOCCH(NH_3^+)CH_2SH$	11.9
Dimethyl sulfide CH_3SCH_3	3.7
Thiourea H_2NCSNH_2	7.11
Methylamine CH_3NH_2	3.06
Tetraethyl pentamine $NH_2(CH_2CH_2NH)_3CH_2CH_2NH_2$	7.4
Acetic acid CH_3COOH	0.73
Butylmalonic acid $CH_3(CH_2)_3CH(COOH)_2$	0.74
Ethylenediaminetetraacetic acid $(HOOC)_2CH_2N(cH_2)_2N(COOH)_2$	7.22
Phenol C_6H_5OH	0.34

Li et al.[70] synthesized layered silver(I) dithiocarboxylate coordination polymer $[Ag(Py\text{-}4\text{-}CSS)]_n$ with the ligand sodium pyridine-4-dithiocarboxylate (Py-4-CSSNa) (shown in Figure 2.8). Each Ag(I) ion coordinates two sulfur atoms and one nitrogen atom specifically shown in Figure 2.8 c. The short Ag···Ag distance indicates the existence of argentophilicity and the $[Ag(Py\text{-}4\text{-}CSS)]_n$ layers stack along the c axis promoted by weak Ag···S interactions between the layers. $[Ag(Py\text{-}4\text{-}CSS)]_n$ has a photothermal conversion efficiency of 22.1%, two times higher than for pure Ag_2S.

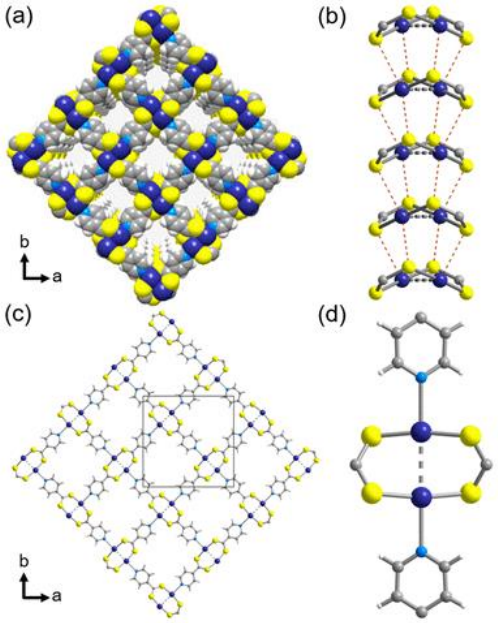

Figure 2.8. (a) Packing scheme, (b) interlayer Ag···S interactions, (c) the single layer, and (d) the secondary building unit of [Ag(Py-4-CSS)]$_n$. Color codes: silver, dark blue; sulfur, yellow; nitrogen, light blue; carbon, gray; hydrogen, white. Figure is adapted with permission from Inorganic chemistry 2019, 58, 6601-6608.[70]

2.1.2.3 Lamellar structure of Ag(I) thiolate

In 1991, Dance et al.[71] exhibited a series of alkane thiolates to calculate the X-ray diffraction patterns of polycrystalline Ag(I) thiolate, shown in Figure 2.9 a (*b* is defined as the axial direction normal to the layers; *kd* as the large interlayer repeat distance *b*). They presented a model that Ag and S atoms comprised parallel slabs with the substituents distributed on both sides of each slab (Figure 2.9 b). Figure 2.9 c displays the network of a slab, a quasi-hexagonal network with trigonal-planar coordination of Ag by three SR moieties and RS coordinated by three Ag atoms.

(a)

Table I. Observed Interlayer Spacing (*kd* Values) from the Pronounced (0*k*0) Reflections

compound	interlayer spacing $b = kd$ values, Å							
	$k = 1$	$k = 2$	$k = 3$	$k = 4$	$k = 5$	$k = 6$	$k = 7$	$k = 8$
$AgS(CH_2)_2CH_3$ (**1**)	12.38	12.52	12.51	12.55	12.58			
$AgS(CH_2)_3CH_3$ (**2**)	15.45	15.47	15.42	15.42	15.49	15.66		
$AgS(CH_2)_5CH_3$ (**3**)	19.59	19.87	20.06	20.11	20.10			
$AgS(CH_2)_7CH_3$ (**4**)	24.8	24.0	24.76	24.81	24.95	25.00	24.96	24.98
$AgSC_6H_5$ (**5**)	14.06	14.01	14.06	14.04	14.05	14.06	14.08	14.22
$AgSC_6H_4$-4-F (**6**)	14.67	14.66	14.66	14.67	14.68	14.68	14.69	14.70
$AgSC_6H_4$-4-Cl (**7**)	16.35	16.40	16.28	16.33	16.34	16.32	16.44	
$AgSC_6H_4$-4-Br (**8**)	16.88	16.93	16.89	16.87	16.86	16.84	16.67	
$AgSC_6H_4$-4-CH_3 (**9**)	16.38	16.43	16.37	16.36	16.38	16.38	16.49	16.39
$AgSC_6H_4$-4-OCH_3 (**10**)	17.12	16.93	17.04	17.10	17.13	17.13	17.15	17.15

(b)

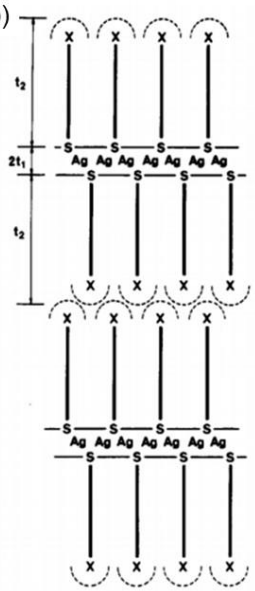

(c)

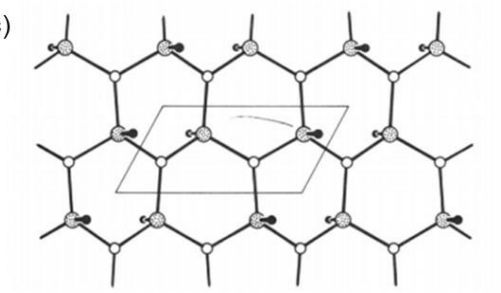

Figure 2.9. (a) Interlayer spacings from the pronounced (0k0) reflections. (b) Scheme of the layered crystal structure. The thickness of the central Ag-S slab is labeled as $2t_1$. The total thickness of one layer is labeled as $2t_1 + 2t_2$ (see (b)). (c) The scheme of the central slab of AgSR. Ag: white circle; S: gray circle; R: black circle. Figure is adapted with permission from Inorganic Chemistry 1991, 30, 183-187.[71]

In 2019, Veselska et al.[72] synthesized new lamellar silver thiolate coordination polymers $[Ag(p\text{-}SPhCO_2H)]_n$, with emission wavelengths at 484, 528, and 700 nm, when excited at 324, 352, 368, and 396 nm at 93 K. The crystallographic data and Rietveld refinement parameters of $[Ag(p\text{-}SPhCO_2H)]_n$, and the structure is shown in Figure 2.10, similar to the model established by Dance et al.[71], with distorted hexagons of Ag_3S_3. Ag(I) atoms in trigonal geometry are connected to three bridging μ_3-sulfur atoms. Because of the similar structure of $[Ag(p\text{-}SPhCO_2H)]_n$ and $[Cu(p\text{-}SPhCO_2H)]_n$, the heterometallic material $[Ag_{0.85}Cu_{0.15}(p\text{-}SPhCO_2H)]_n$ can be obtained.[72] When excited at 344 nm at 93 K, $[Ag_{0.85}Cu_{0.15}(p\text{-}SPhCO_2H)]_n$ has an emission at 485, 524, and 560 nm. When excited at 372 nm at 93 K, it has an emission at 690 nm. Therefore, the emission range can be tuned by the excitation range.

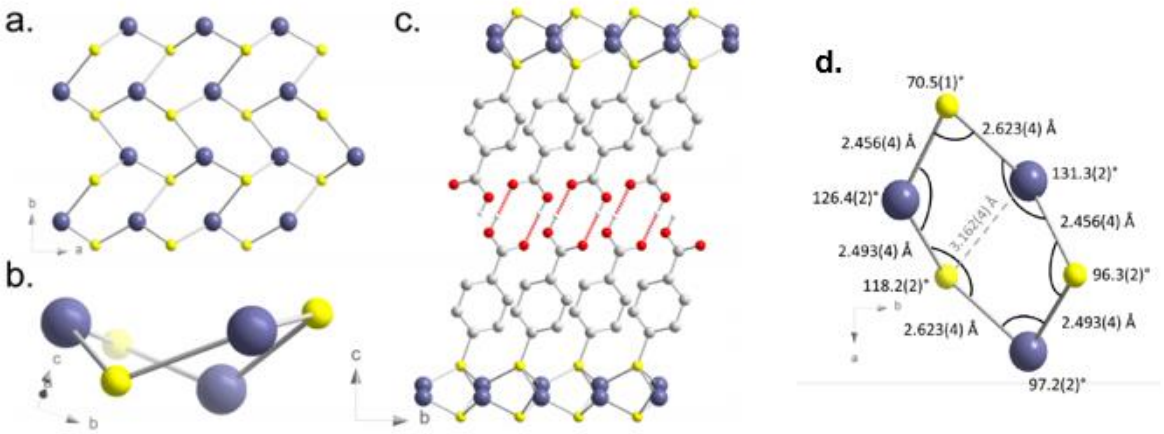

Figure 2.10. Structure of [Ag(p-SPhCO$_2$H)]$_n$,(a) representation of the Ag_3S_3 network on the (ab) plane, (b) view of the distorted Ag_3S_3 cycle, (c) view of the lamellar structure with the hydrogen bonds between the carboxylic acids (dotted red lines), and (d) bond distances and angles in the Ag_3S_3 hexagons. Blue: Ag(I); yellow: S; red: O; and gray: C. Hydrogen atoms are omitted for clarity. The figure is adapted and modified with permission from Inorganic chemistry 2018, 58, 99-105.[72]

2.1.2.4 The subsequent reaction of silver(I) thiolate

In their review, Bell et al.[69] not only systematically introduced the structural chemistry and geochemistry of silver sulfur compounds, but also presented an overall scheme for the environmental cycle of Ag(I), showing that formation of Ag_2S is the most probable outcome for Ag(I) in silver thiolates in a sulfur-rich environment (shown in Figure 2.12).

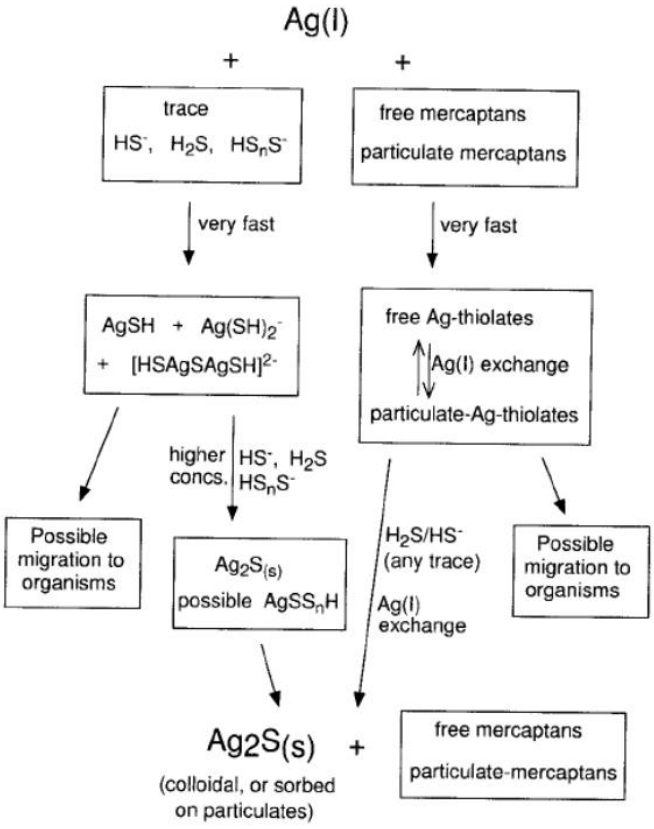

Figure 2.12. Schematic of possible outcomes for silver(I) in an environment rich in sulfur as S(II⁻) or as organic mercaptans (RSH). Figure is adapted with permission from Environmental Toxicology and Chemistry: An International Journal 1999, 18, 9-22.[69]

Chen et al.[73] used silver the thiolate $AgSC_{12}H_{25}$ as melt precursor for the synthesis of Ag nanodisks. The intense narrow reflections of layered $AgSC_{12}H_{25}$ shown in Figure 2.13 d, which has the same structure of lamellar silver(I) thiolate as we shown in Figure 2.9 a,b, the interlayer distance is 34.9 Å, and the in-plane Ag-Ag distance is ~4.5Å. After heating $AgSC_{12}H_{25}$ under nitrogen flow at ~200 °C, Ag nanodisks are obtained (TEM shown in Figure 2.13 b,c, XRD shown in Figure 2.13 e) with an average diameter of ~16 nm and thickness of ~2.3 nm. This reaction is based on Ag^+ which is reduced by SR^-, the two SR^* radicals yield disulfide. The reaction equation is shown in Figure 2.13 a. Two processes can explain the formation of this morphology: the first process is nucleation, $AgSC_{12}H_{25}$ decomposes to small metallic silver clusters by heating; the second process involves thiol ligand sterically hindering the Ag interplanar diffusion of Ag. Therefore, Ag atoms tend to aggregate in-plane. This simple method offers ample possibilities for shape control.

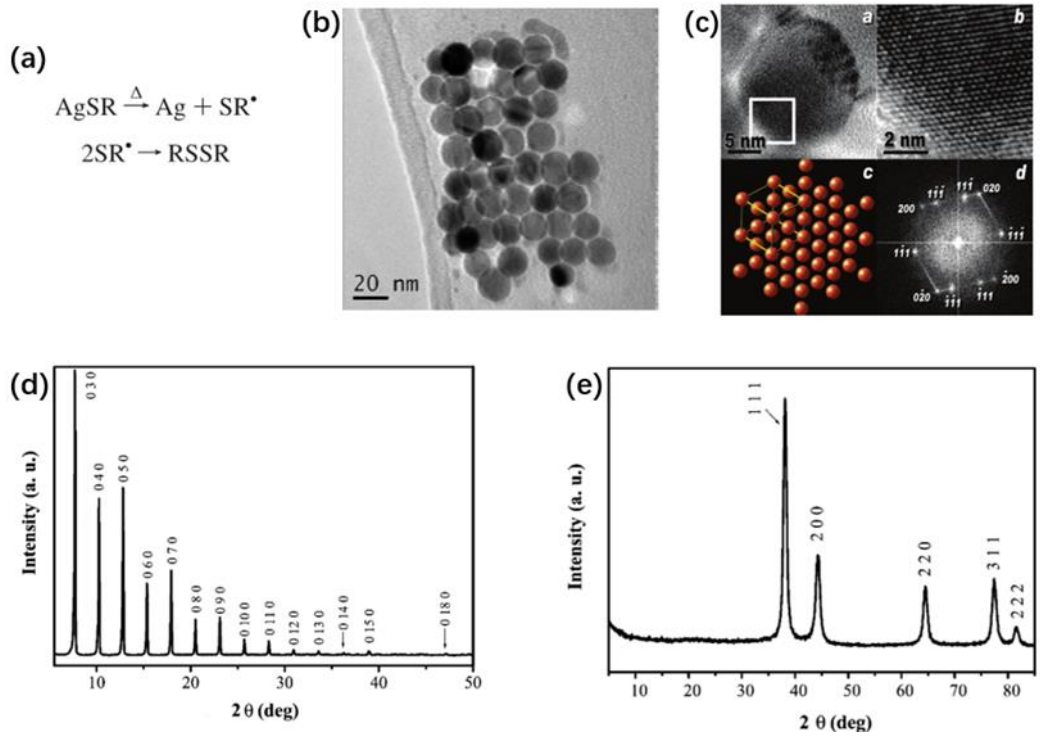

Figure 2.13. (a) The equation for the reaction of $AgSC_{12}H_{25}$ to silver nanodisks; (b) TEM image of a Ag nanodisk; (c) HRTEM image of a nanodisk witha [111] projection of the cubic silver structure with the unit cell marked, and the fast fourier transformation (FFT) of the Ag nanodisks micrograph; (d) XRD pattern of $AgSC_{12}H_{25}$; (e) XRD pattern of Ag nanodisks produced at 180 °C for 2 h. Figure is adapted and modified with permission from Inorg. Chem. 2005, 44, 9817-9822.[73]

2.1.2.5 Luminescent silver(I) complexes

In metal complexes, the metal-ligand bonds are generally polar because the electron density is dominantly located on the metal side or the ligand side. Therefore, the electronic transition can be classified as metal-centered, ligand-to-metal charge transfer (LMCT), metal-to-ligand charge transfer (MLCT), ligand-to-ligand charge transfer (LLCT), metal-to-metal charge transfer (MMCT), and ligand-centered.[74] For d^{10} metal ions, there are several more possible electron transition states for luminescence.

For multinuclear d^{10} metal complexes and d^{10} metal ions with donor ligands, the lowest-energy transition contains contributions from the metal center or LMCT. It is almost not possible to distinguish these two kinds of transitions. Therefore, the emission state may be due

to both the metal centered and LMCT and possibly also modified by metallophilic interactions.[75-76]

Silver (I) chalcogenid clusters with long-lived green to orange luminescence was taken here to show the possible change transfer for silver(I) complexes.[77] The photophysical data of $[Ag_4(\mu\text{-dppm})_4(\mu_4\text{-E})]^{2+}$ (E = S, Se, Te) is shown in Table 2.5, the structure is shown in Figure 2.14.[78] The molecular orbital diagrams are shown in Figure 2.15. The highest occupied molecular orbital (HOMO) is mainly from the bonding interaction between the chalcogen atom and silver atoms. The lowest unoccupied molecular orbital (LUMO) mainly contributes from silver atoms. Therefore, the emission originate mainly from LMCT [$(E^{2-})\rightarrow Ag_4$], probably with mixing of metal centered (d-s/s-p) silver states. The Ag-Ag interaction mainly contributed form 5s and 5p orbitals.

Table 2.5. Photophysical data for $Ag_4(\mu\text{-dppm})_4(\mu_4\text{-E})]^{2+}$ (E = 1-S, 2-Se, 3-Te). (Table is adapted with permission from Inorganic Chemistry 1996, 35, 5116-5117[78]).

cluster	abs[a] λ/nm (ϵ/dm^3 mol^{-1} cm^{-1})	medium (T/*K*)	emission λ/nm (τ_o/μs)
1	246 sh[b] (91 745)	solid (298)	516 (1.0 ± 0.1)
	400 sh (970)	solid (77)	536
		$(CH_3)_2CO$ (298)	628 (1.2 ± 0.1)
		CH_3CN (298)	628 (1.5 ± 0.2)
2	256 sh (53 985)	solid (298)	527 (0.9 ± 0.1)
	402 sh (1445)	solid (77)	552
		$(CH_3)_2CO$ (298)	570 (1.3 ± 0.1)
		CH_3CN (298)	572 (3.4 ± 0.3)
3	254 sh (67 075)	solid (298)	574 (3.1 ± 0.2)
	440 sh (1475)	solid (77)	588
		$(CH_3)_2CO$ (298)	615 (1.4 ± 0.1)
		CH_3CN (298)	626 (3.3 ± 0.3)

[a] All UV−vis absorption spectra were recorded in acetonitrile solutions. [b] The absorption shoulders were determined from the derivatives of the UV−vis absorption spectra.

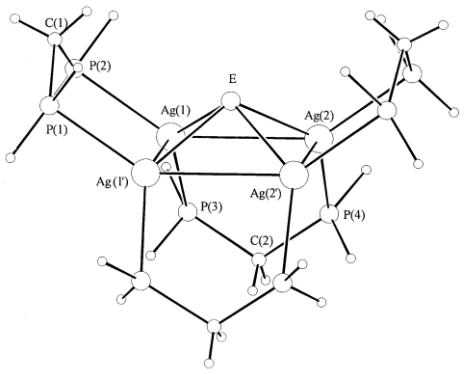

Figure 2.14. A perspective scheme of $[Ag_4(\mu\text{-dppm})_4(\mu_4\text{-E})]^{2+}$ (E = S, Se, Te) with the atomic numbering scheme. Figure is adapted with permission from Dalton Transactions 1997, 227-230.[79]

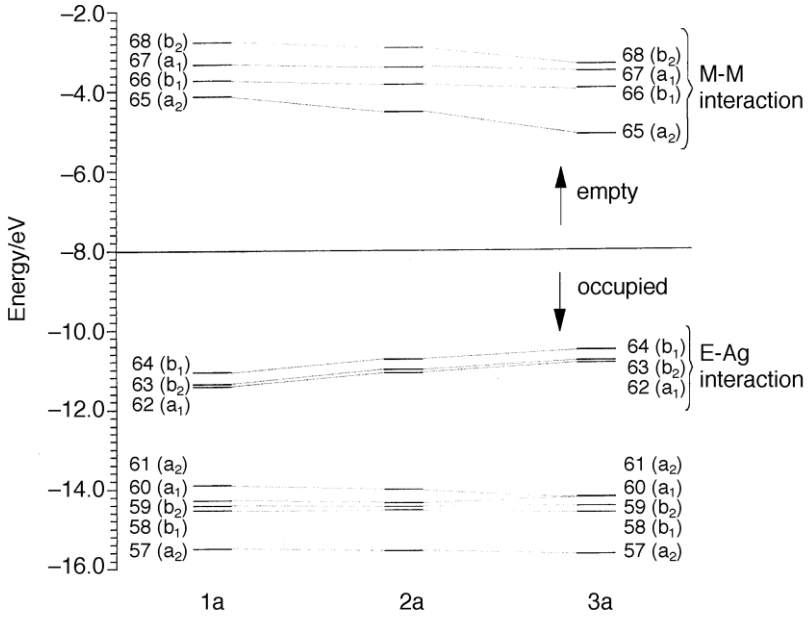

Figure 2.15. Molecular orbital diagrams of complexes $[Ag_4(\mu\text{-dppm})_4(\mu_4\text{-E})]^{2+}$ (E = S-1a, Se-2a, Te-3a). Figure is adapted and modified with permission from Dalton Transactions 1997, 227-230.[79]

2.1.2.6 Argentophilic interaction

The metallophilic interaction is a weak electrostatic attractive force between two metal cations,[80] which tend to have attractive interactions rather than repulsion when their distances are smaller than the sum of the van der Waals radii.[81]

Metallophilic interaction occurs mainly between low-valent closed-shell [$(n-1)d^{10}ns^0$] and pseudo-closed shell [$(n - 1)d^8ns^0$] metal ions,[82-83] such as Cu(I), Ag(I), Au(I), Hg(II), Pd(II), Pt(II). In 1987, Martin Jansen summarized possible bonding interactions between metal cations with a closed-shell electronic configuration.[84,85-87]

When the distance between two or more low-coordinated silver cations with a $[Kr]4d^{10}$ electronic configuration is shorter than the van der Waals contact of ~3.44 Å, argentophilic interactions should be considered.[88] Depending on whether ligands connect Ag(I) cations or not, the argentophilic interactions are categorized as supported and unsupported (as shown in Figure 2.16). In the unsupported situation (shown in Figure 2.16 1a-1c), the Ag-Ag contact is the closest distance between independent molecules, which is easy to evaluate. In the supported situation (shown in Figure 2.16 2a-2g), ligand bridges can shorten or elongate the Ag-Ag distance. Therefore, the Ag-Ag contact is hard to evaluate in the supported situation.

The argentophilic interactions can occur between pairs of silver atoms and multinuclear units such as chains and layers. When silver exhibits multi-argentophilic interactions, there is no significant change in length compared to the standard distance and argentophilic interactions without directionality.

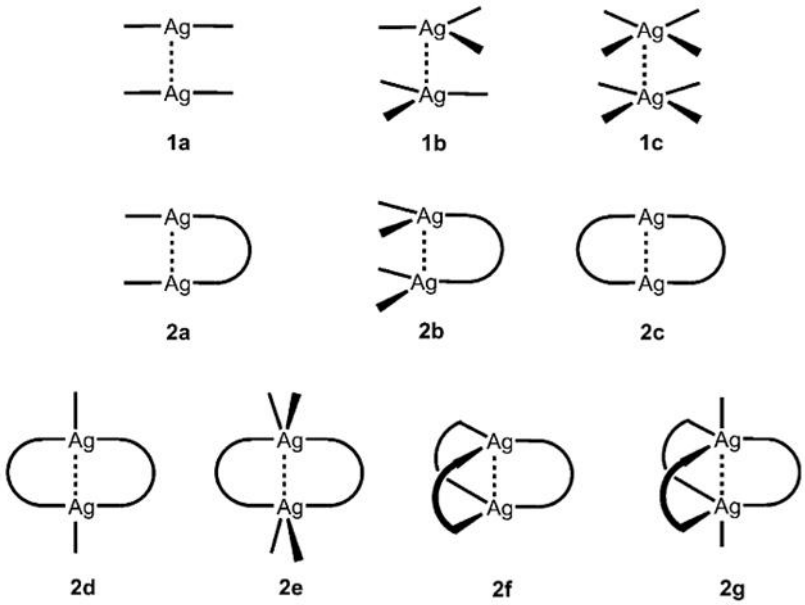

Figure 2.16. The scheme of supported (1a-c) and unsupported (2a-g) silver(I) cations. Figure is adapted with permission from Angewandte Chemie International Edition 2015, 54, 746-784.[88]

Since in the molecules and aggregates the internal molecular motions will be affected by argentophilic interactions, the vibrational spectra such as Raman spectra can be used to measure and confirm the effect (with a proper reference system in hand).

Che et al.[89] published the spectroscopic evidence for argentophilicity in binuclear silver (I) complexes. The molecular structure of $[Ag_2(\mu\text{-dcpm})_2](CF_3SO_3)_2$ (dcpm=bis(dicyclohexylphosphino)methane) is shown in Figure 2.17. The Ag-Ag separation distance is 2.948 Å as revealed by X-ray structural analyses. The 261 nm UV absorption band for $[Ag_2(\mu\text{-dcpm})_2](CF_3SO_3)_2$ in acetonitrile is assigned to a $4d\sigma^* \rightarrow 5p\sigma$ transition. originating from Ag(I)−Ag(I) interactions. In the Raman spectra, the entire intensity appears in the Ag−Ag stretch fundamental (80 cm^{-1}) and overtone bands.

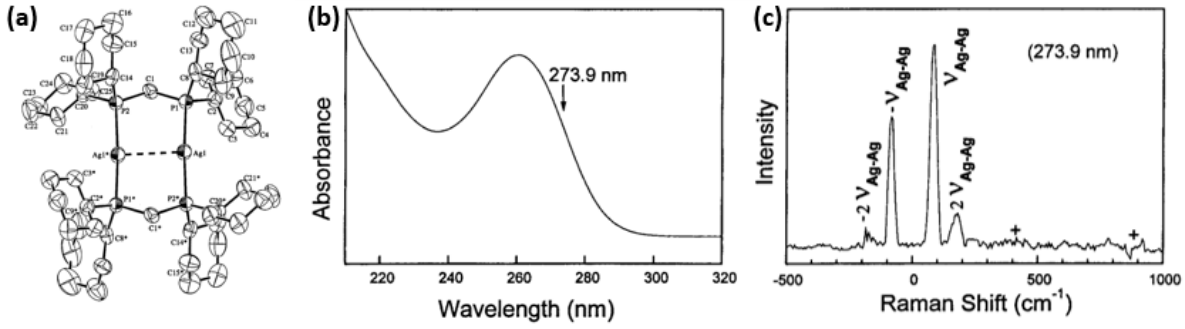

Figure 2.17. (a) Perspective view of $[Ag_2(\mu\text{-dcpm})_2](CF_3SO_3)_2$; (b) UV-vis absorption spectra; (c) Raman spectra for $[Ag_2(\mu\text{-dcpm})_2](CF_3SO_3)_2$ in acetonitrile (solvent subtraction artifacts are marked by (+). Figure is adapted with permission from Journal of the American Chemical Society 2000, 122, 2464-2468.[88]

Since silver(I) complexes can exhibit various photoluminescence phenomena, their absorption and photoluminescence characteristics are extensively studied for mononuclear and multinuclear silver(I) complexes. There are several possible electronic transfers between metal and ligand associated with the optical properties, which has been discussed in the previous section. The argentophilicity affects the photoluminescence properties mainly by ligand-to-metal-metal charge transfer (LMMCT) and metal-to-metal transfer (MMCT). If ligands have suitable HOMOs, the absorption and emission properties are mainly determined by LMMCT.

Huang et al.[90] synthesized a metal-organic framework $[Ag_3(BTC)(pyz)]_n \cdot (H_2O)_n$ (pyz = pyrazine), which is a repeated Ag_3 unit sustained by 1,3,5-benzenetricarboxylic acid (1,3,5-H_3BTC) and argentophilic interactions (as shown in Figure 2.18 a). The temperature dependent luminescence property was studied. When the temperature decreased from 298 K to 77 K, the emission intensity sharply rose, with redshift of ~6 nm due to the stronger self-association of the silver(I) ions through argentophilic interactions (as shown in Figure 2.18 b).[91]

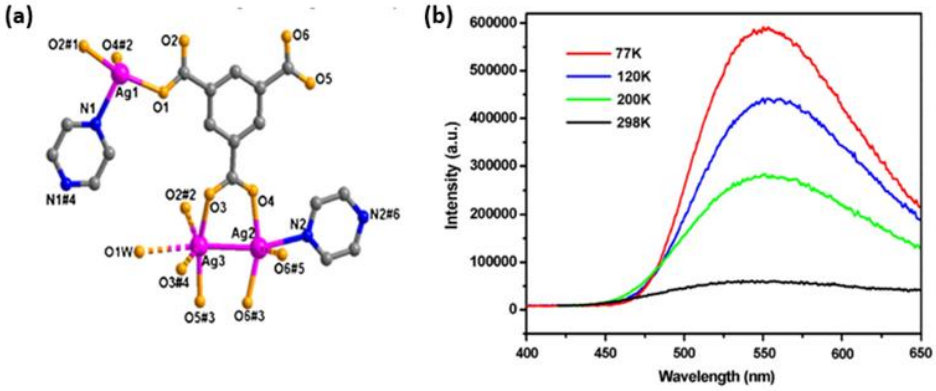

Figure 2.18 .(a) The scheme of $[Ag_3(BTC)(pyz)]_n \cdot (H_2O)_n$; (b) Emission spectra collected with excitation at 363 nm in the solid state at different temperatures. Figure is adapted with permission from Inorganic Chemistry Communications 2013, 33, 38-42.[90]

If instead suitable ligands are not part of the structure, the absorption and emission properties are related to MMCT. Rawashdeh Omary et al.[92] studied the concentration dependence of the absorption spectra of a $K[Ag(CN)_2]$ aqueous solution. $K[Ag(CN)_2]$ aqueous solution exhibits new longer wavelength features when the concentration increases (shown in Figure 2.19). It illustrates the oligomerization of $Ag(CN)^{2-}$ anions in water. According to their calculation, when the oligomer size (n) increases, the HOMO becomes destabilized which is responsible for the Ag-Ag antibonding character. However, when the oligomer size (n) increases, the LUMO becomes stabilized and is responsible for the Ag-Ag bonding character.[93-95]

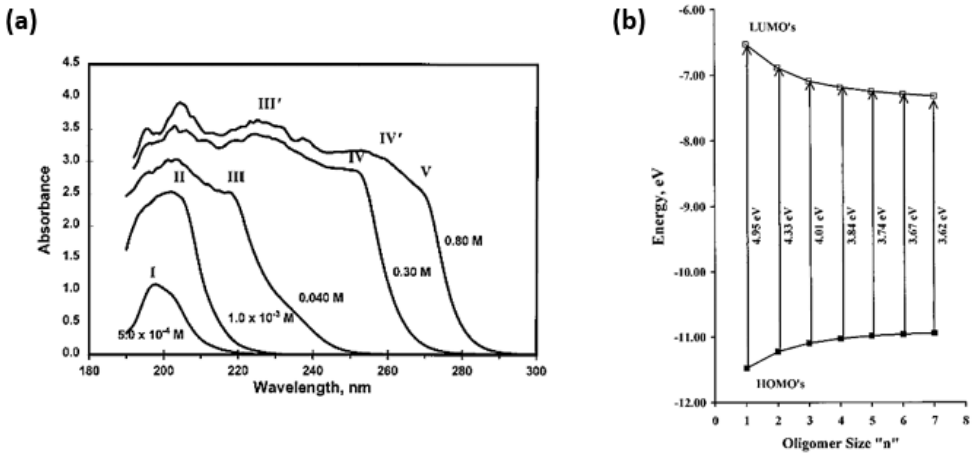

Figure 2.19. (a) Absorption spectra of different concentration $K[Ag(CN)_2]$ aqueous solutions at ambient temperature; (b) Energies of HOMO and LUMO for $[Ag(CN)_2^-]_n$ oligomers with $n=1-7$. Figure is adapted with permission from Journal of the American Chemical Society 2000, 122, 10371-10380.[92]

2.2 Gels

According to Kramer's definition, a gel is a soft solid or solid-like material consisting of two or more components, one of which is a liquid, present in substantial quantity,[96] the remaining is the solid network to immobilize the flow of the liquid.[97-98]

Possible gelators and driving forces for gel formation[99] are listed in Figure 2.20. Traditional covalent bonding is a relatively stable and strong chemical structure involving sharing pairs of electrons. Dynamic covalent bonding is covalent bonding as well, with reversible breaking and reformation capability.[100] Metal-organic bonds form through Lewis acid-base interactions following the hard-soft interaction principle. Hydrogen bonding, a popular non-covalent interaction to construct supramolecular architectures, is much stronger than van der Waals interactions and weaker than covalent bonds. π- π interaction exists among aromatic and other π-delocalized moieties. Van der Waals, halogen bonding, cation-π, metallophilic interactions, and solvophobic effect also play essential roles in forming supramolecular gels.

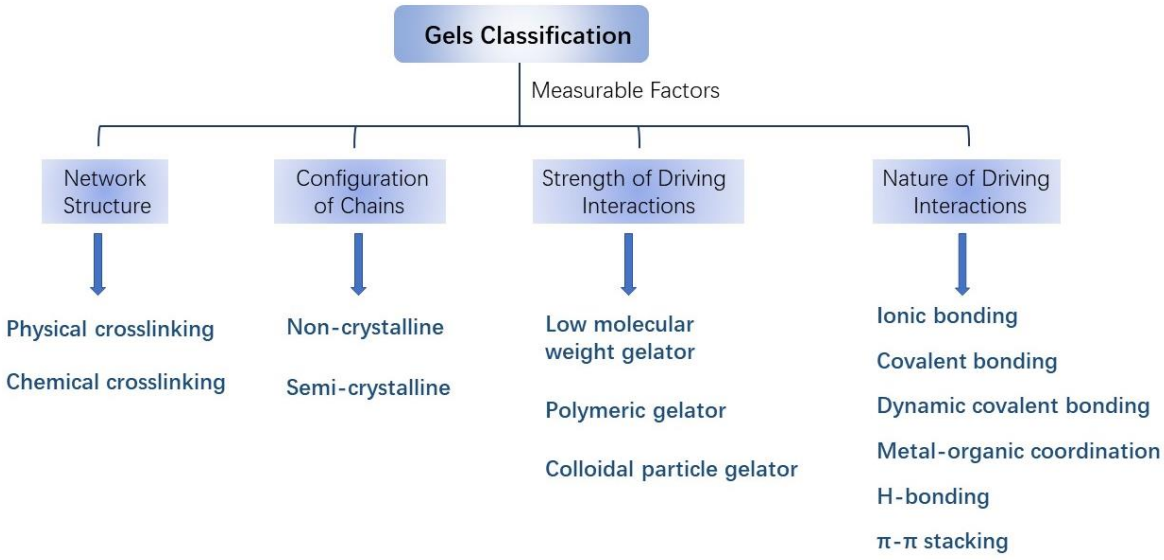

Figure 2.20. Classification of gels by different measurable factors.

2.2.1 Supramolecular gel

Supramolecular gels assemble via non-covalent interactions between low molecular-weight gelators (LMWGs) with molecular mass less than 3,000 Da.[101] Through hierarchical self-assembly LMWGs can form bulk gels. On application of an appropriate trigger, individual gelator molecules assemble through non-covalent interactions to form fibrils, which subsequently bundle together to form wider nanofibers. Nanofiber entanglement results in the formation of a solid-like network, stable towards gravitational force when it is put upside down (as shown in Figure 2.21).[102]

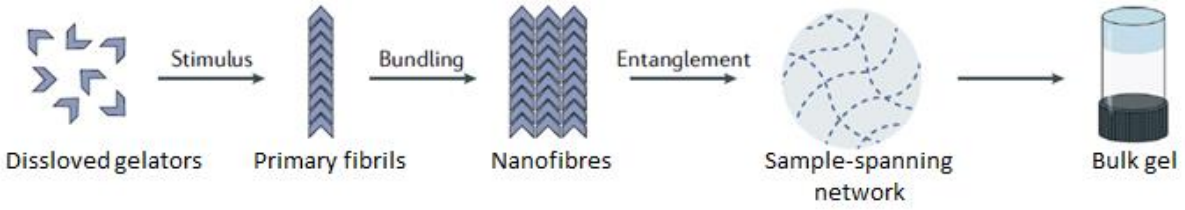

Figure 2.21. Schematic of supramolecular gel assembly. Figure is adapted with permission from Nature Reviews Materials 2019, 4, 463-478.[102]

The common preparation method of gels is to warm the gelator molecules in a particular solvent or a mixture of solvents until all the solids are completely dissolved (sol form). Upon cooling, the gelator molecules would undergo supramolecular assembly to form three-dimensional nano- or microstructures to immobilize solvent molecules so that a stable gel is formed.[103] This sol-gel phase transition process is usually reversible under external stimuli. Thermo-reversibility is the common property, and lots of supramolecular gels are responsive to mechanical stress, light, pH value, chemicals and ionic strength.[104-108]

He et al.[109] used ferrocene as a pendant structure introduced into dicholesteryl derivatives to from a series of cholesterol gel. They named these compounds according to the hydrogen bonding sites number. Compound 2 shows the reversibility of sol-gel phase transition under several external stimuli (as shown in Figure 2.22), such as $CH_3(CH_2)_4COOH/NH_3$, shear stress, and ultrasound treatment. Here, NH_3 was necessary for the recovery process after heating. This phenomenon can be explained by the protonation of a tertiary amine, which makes the gelator molecules become ionic and increase the repulsion, resulting in the collapse of the gel network.

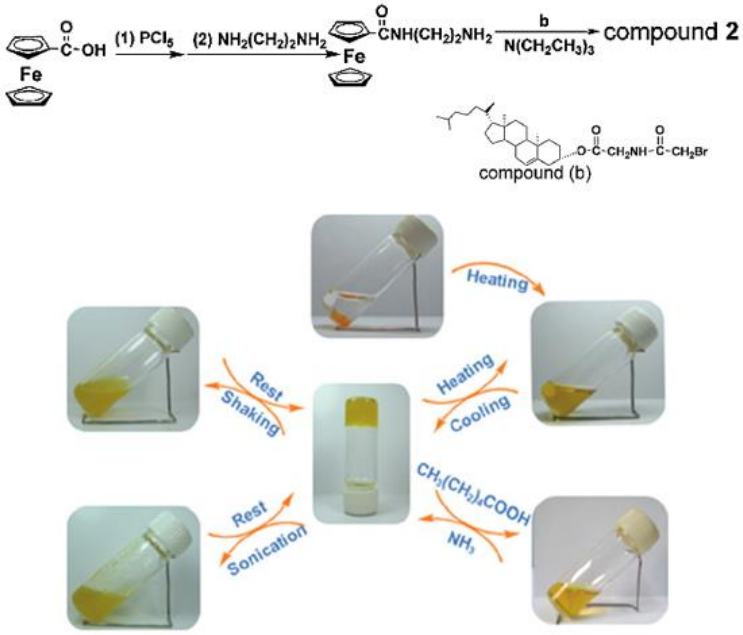

Figure 2.22. Schematic representation of the synthesis of compound 2 and the reversible sol-gel phase transition triggered by differet factors. Figure is adapted with permission from Physicochemical and Engineering Aspects 2010, 362, 127-134.[109]

2.2.1.1 Hydrogen-bonded supramolecular gel

Hydrogen bond, an electrostatic attraction between hydrogen atoms, is a covalent bond to a molecule or functional group of higher electronegativity. Pauling mentioned the hydrogen bond firstly in 1912.[110-111] In the past decades, lots of LMWGs were synthesized and studied, in which hydrogen bonds play an important role. Some typical hydrogen donor···acceptor pairs are shown in Figure 2.23.

Donor ····· Acceptor
F — H ····· :F
O — H ····· :N
O — H ····· :O
N — H ····· :N
N — H ····· :O
S — H ····· :S
F — H ····· :F

Figure 2.23. Typical hydrogen donor···acceptor pairs.

Based on the hydrogen bonding between amino acid and carboxylic modified compounds, Li et al.[112] prepared four (-)-menthol derivate compounds 1-4 (structures shown in Figure 2.24) and characterized their gelation behavior. Compound 1 and compound 2 can gelate because amino acid modification plays a crucial role in it. Compound 3 and 4 only can dissolve in the organic and protic solvent. The main driving force for the good hydrogelator compound 2 is the generation of dimer structure, because of the hydrogen bonding between C=O and N-H. These dimers accumulate lengthways on the fibrils to form fibers. In the end, under the interaction of hydrophobic menthol groups, these fibers cross-link to create gelation networks (shown in Figure 2.24).

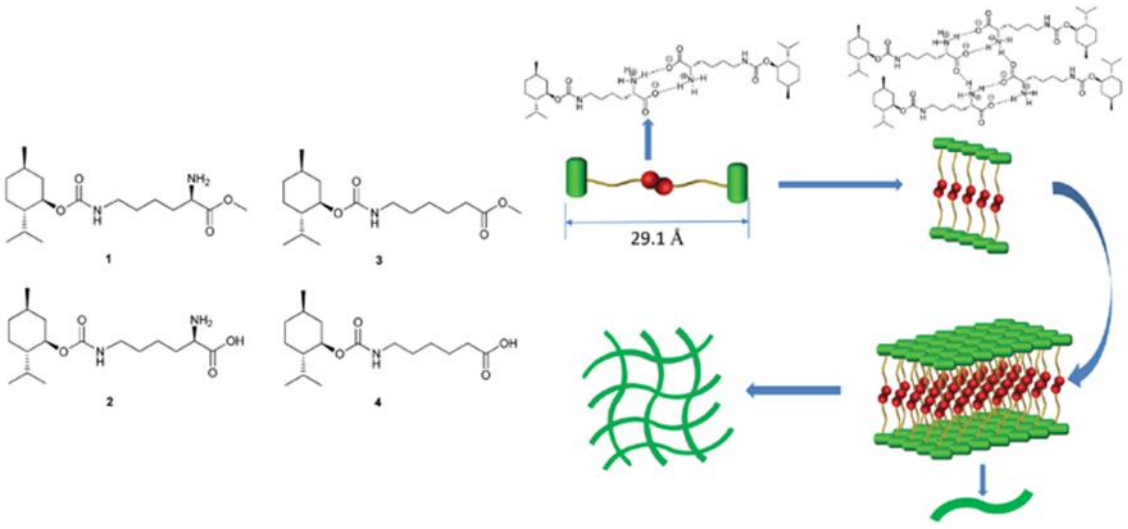

Figure 2.24. Structures of (-)-menthol derivate compounds 1-4 and the simulative diagram of the self-assembly process of molecules of compound 2. Figure is adapted with permission from Soft Matter 2014, 10, 3077-3085.[112]

2.2.1.2 Metallogels

The functionalized metal complexes can self-assemble with proper functional groups and non-covalent interactions based on metal-ligand coordination chemistry. For coinage metals, metallophilic interaction also plays an essential role in stabilizing the network and increasing exciting properties.[113]

Shen et al.[114] designed an Ag(I)- glutathione (GSH) coordination polymer supramolecular hydrogel. The PL spectra of the Ag(I)-GSH hydrogel blue shifts from 545 nm to 435 -420 nm compared with bulk Ag(I)- GSH solution. This was attributed to the rigidochromic effect (shown in Figure 2.25 b).[115] This phenomenon is related to LMMCT transitions because of argentophilicity. When adding 1 eq. iodine into the hydrogel, the gel-to-sol transition can be triggered, making it a facile and selective method to visualize the presence of iodine. Upon subsequent addition of 1 eq. Ag^+, the solution can transform again into a gel state (shown in Figure 2.25 a). The mechanism of this iodine-triggered gel-sol transition is related to the stability constant of AgI ($1.08\times10^{16}\,M^{-1}$), which is higher than AgF ($2.09\,M^{-1}$), AgCl ($1.05\times10^{10}\,M^{-1}$), AgBr ($1.35\times10^{11}\,M^{-1}$) [116], and AgSR ($10^{13}\,M^{-1}$ order of magnitude).[117] Due to the high stability constant of AgI, iodine can displace -SR in the coordination polymer structure resulting in the depolymerization of the structure and the release of entrapped solvent molecules.

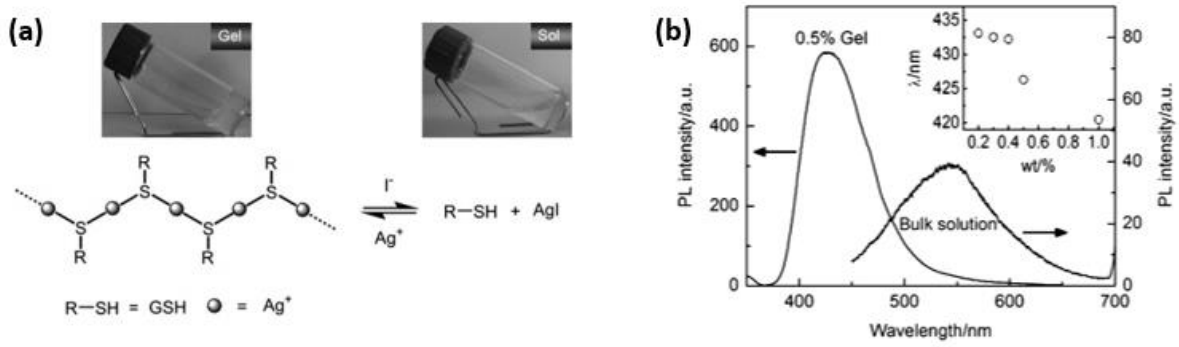

Figure 2.25. (a) Illustration of reversible gel–sol state transition of Ag(I)-GSH coordination polymers triggered by alternately adding iodine into hydrogel and Ag(I) into the resulting sol solution; (b) PL spectra of hydrogel and of bulk solution, λ_{ex}=350 nm. Inset in (b) shows plot of maximum emission wavelength of the hydrogel versus Ag(I)-GSH content. Figure is adapted with permission from Journal of Materials Chemistry 2009, 19, 6219-6224.[114]

Kishimura et al.[118] synthesized a trinuclear Au(I) pyrazolate complex. At room temperature, this Au(I) complex was an organogel luminescing red (gel-form). Upon heating, the gel turned to a transparent solution and lost all luminescence properties (sol-from). This process could be reversed upon cooling. This thermoreversible color change and the sol-gel transition have been attributed to a triplet metal-centered excited-state modified with an Au(I)-Au(I) metallophilic interaction (shown in Figure 2.26). The addition of AgOTF to this Au(I) pyrazolate complex leads to a green luminescing solution in the hot state. This property was attributed to the heterometallic Au(I)-Ag(I) species and blue-luminescent gel at room temperature due to the presence of the original red-luminescent species. This sol-gel transition was also thermoreversible. When using Cl^- to remove Ag^+, it can recover the red-luminescent gel by cooling.

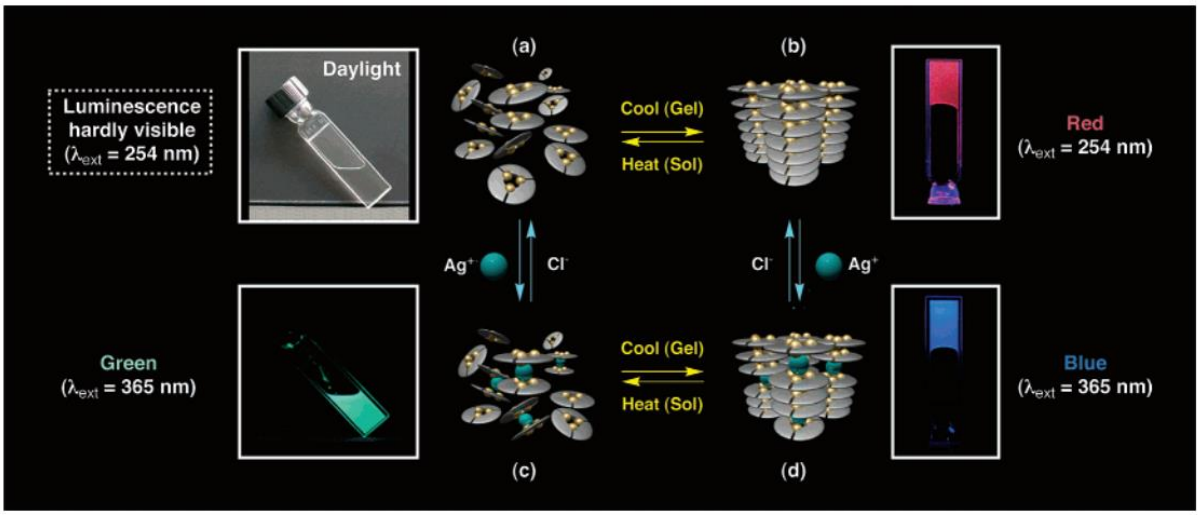

Figure 2.26. Luminescence profiles of Au(I) pyrazolate complex in hexane. Pictures and schematic representation of self-assembled structures; (a) sol, (b) gel, (c) sol containing AgOTf (0.01 eq.), and (d) gel containing AgOTf (0.01 eq.). Figure is adapted with permission from Journal of the American Chemical Society 2005, 127, 179-183.[118]

2.2.2 Poly(vinyl alcohol) hydrogels (PVA)

Poly(vinyl alcohol) (PVA) is a water-soluble synthetic polymer prepared from polyvinyl acetate by hydrolysis. The degree of hydrolysis affects the chemical properties, solubility, and crystallizability of PVA.[119] To make PVA a useful hydrogel, it must be cross-linked, achieved

by either chemical or physical cross-linking. One of the chemical methods is the addition of cross-linking agents (i.g. gluteraldehyde[120] and other monoaldehydes[121-124] with sulfuric acid or acetic acid[125-127]) to the PVA system to form the acetal bridges with the hydroxyl group of PVA. However, eventual residues are hard to remove. These residues might be toxic. This limits the biomedical application of PVA. Another crosslinking method uses irradiation by γ-rays (^{60}Co sources).[86] The advantage of this method is that there are no toxic materials in the system, but there is bubble formation during the crosslinking process.[86] A physical method for crosslinking PVA chains is the freezing-thawing method. The freezing-thawing method is widely used in prepared PVA hydrogel because of the non-toxic and easy to control cross-linking process.[128]

2.2.2.1 Freezing-thawing method

The freezing-thawing process used for the preparation of PVA hydrogel was first reported in 1975 by Peppas.[129] In a typical freezing-thawing process the PVA aqueous solution is frozen at ~20 ºC, then let to thaw at room temperature. These two processes are repeated many times. With the increasing of the freezing-thawing cycles, the mechanical properties of PVA hydrogel can be enhanced.[130] During the water freezing process, PVA is expelled from the ice domains and forms regions of high PVA concentrations, where crystallization and hydrogen bonding occurs between PVA chains.[131] The crystal structure was studied by Bunn et al.[132] and can be described as a double layer of PVA molecules held together by hydroxyl bonds. Between one double layer and the next weaker van der Waals forces operate as shown in Figure 2.27. In the following thawing process, this structure remains to create hydrogel network. There are lots of amorphous chain segments in the gel system as well, because PVA chains and water molecules are bound by the strong hydrogen bonding between hydroxyl groups in PVA chains and water molecules. The model of these three phases are shown on Figure 2.28 [133]: water phase, amorphous phase and PVA crystal phase.

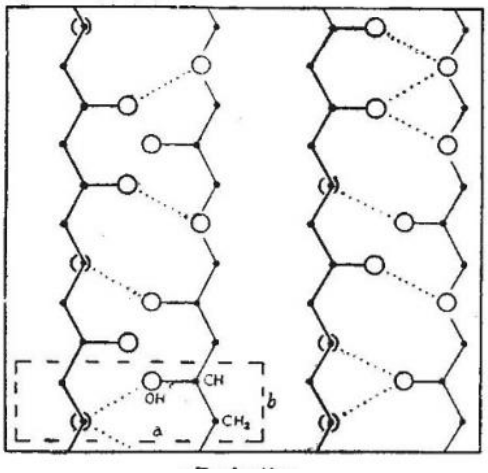

Figure 2.27. Double layer structure of PVA crystals, hydrogen bonds are labeled by dashed lines. Figure is adapted with permission from Nature 1948, 161, 929-930.[132]

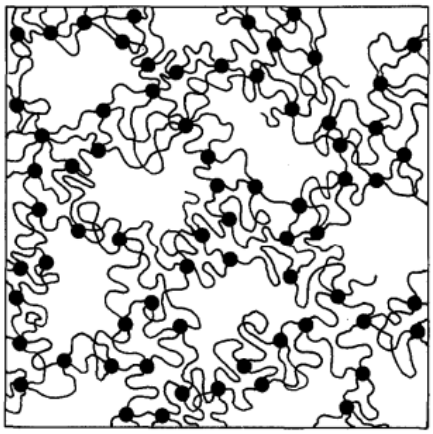

Figure 2.28. Schematic representation of the structural model for PVA hydrogels prepared by repeated freezing-thawing cycles. Solid circles represent PVA crystallites. Figure is adapted with permission from Colloid and Polymer Science 1986, 264, 595-601.[133]

Based on the freezing-thawing process, He's group[134] proposed a freeze-soak method to enhance and tune the mechanism property of hydrogels, based on the Hofmeister effect making use of precipitation induction potential different salts exhibit on proteins from aqueous solutions.[135] To this end, the PVA solution is frozen at -20 °C. During this process, PVA is fixed in a specific shape, and the polymer chains are prepacked in microscopic domains. Then the concentrated salt solution is added to the frozen PVA system and transferred to room temperature. The PVA chains further aggregate and crystallize, induced by added salt ions to form an even more crosslinked hydrogel during the thawing process. This is because the hydration water molecules, which effect the stability of hydrogen bond between PVA chains,

were polarized by SO_4^{2-} and CO_3^{2-} (Figure 2.29 a1). SO_4^{2-} and CO_3^{2-} can also increase the surface tension of the PVA backbone to make it more hydrophilic (Figure 2.29 a2). However, NO^{3-} and I^- can bind with PVA chains to make more PVA dissolve in water to reduce the crystallization of PVA (Figure 2.29 a3).

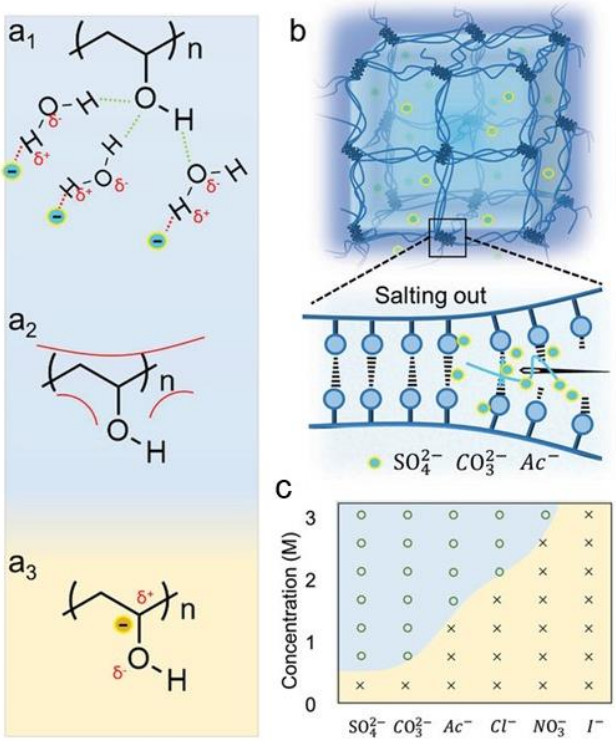

Figure 2.29. (a) The interactions among ions, polymer chains, and water molecules; (b) Hydrogen bonds form between PVA polymer chains induced by ions due to the salting-out effect; (c) Summary of the status of PVA gelation induced by different anions of different concentrations. The circle represents the gelation condition and the cross represents nongelation conditions. Figure is adapted with permission from Advanced Materials 2021, 33, 2007829.[134]

In further work, He's group used the synergistic effects of directional freezing process and the Hofmeister effect to prepare "super strong" PVA hydrogels with both a honeycomb-like micro-network and aligned pore walls.[136] This hierarchical and anisotropic PVA hydrogel can achieve toughness of 175 MJ/m^3, ultimate stress of 11.5 MPa, and ultimate strain of 2900%.[136]

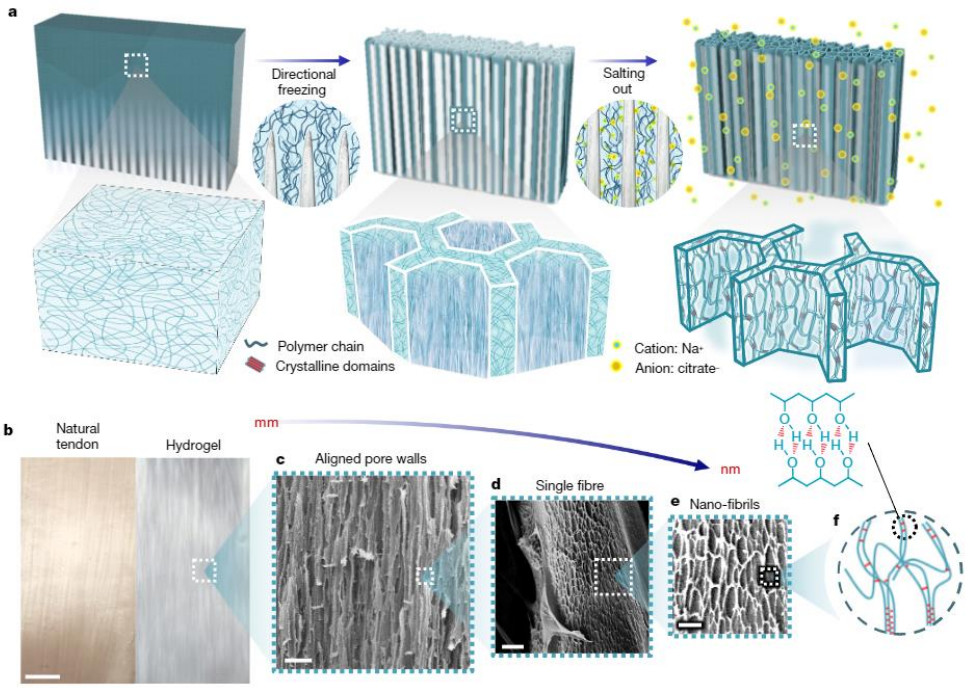

Figure 2.30. (a) The scheme of the structure formation and polymer chain concentration for PVA hydrogel; (b) Macroscopic view of real tendon and of PVA hydrogel. Scale bar is 5 mm.(c)-(e) SEM images showing the microstructure. Scale bars: (c) 50 μm; (d) 1 μm; (e) 500 nm; (f) illustration of polymer chains aggregated into nanofibrils. Figure is adapted with permission from Nature 2021, 590, 594-599.[136]

2.2.2.2 PVA hybrid hydrogels

Other components in aqueous PVA solutions can create a hydrogel with desirable characteristics and enhance the mechanical properties. When other components are added to the PVA hydrogel system as the second network, there is robust chain entanglement between PVA and the second network, resulting in higher toughness and strength.

Li et al.[137] prepared a PVA/polyacrylamide (PVA-PAAm) hybrid hydrogel with the elastic modulus of 5 MPa, a strength of 2.5 MPa, and fracture energy of 14000 $J \cdot m^{-2}$. They prepared PVA-PAAm hydrogel by annealing the PVA/PAAm gel at 120 °C, then re-hydrating this hybrid in distilled water (as shown in Figure 2.31). The aim of this work was to obtain a toughened system by the introduction of covalent cross-links (PAAm), before PVA formed physical cross-

links. Then, during the annealing process, a region of high PVA concentration is generated, which promotes PVA crystallites.

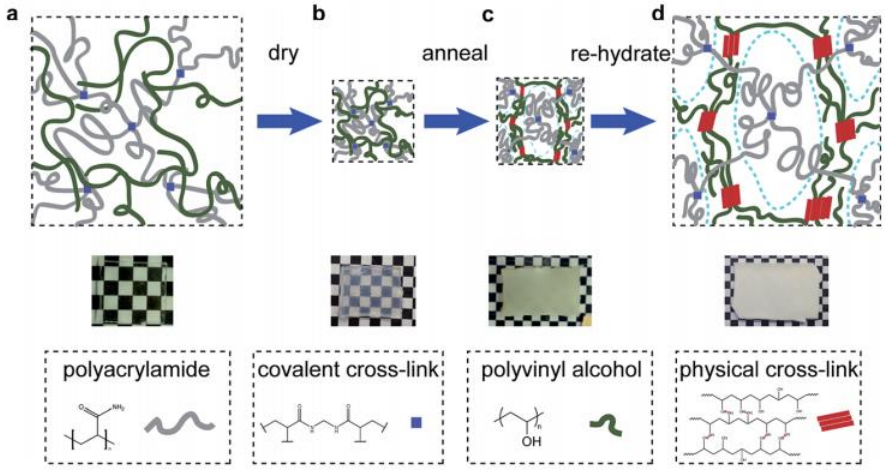

Figure 2.31. Synthesis and structure of the hybrid hydrogel. Figure is adapted with permission from Journal of Materials Chemistry B 2014, 2, 6708-6713.[137]

2.3 Charge carrier dynamics resolved by THz spectroscopy

2.3.1 Optical-pump THz-probe spectroscopy

Terahertz radiation (THz) are electromagnetic waves occupying a middle range of the microwave and infrared light spectrum, with frequencies from 0.1 to 10 THz (1 THz = 10^{12} Hz), or wavelengths ranging from 3 mm to 30 μm (shown in Figure 2.32).[138] Because of the limitation of the generation and detection of THz radiation, historically, it was called the "terahertz gap". New technology needed to be developed to fill this gap.[139] In the 1980s, the "terahertz gap" was filled gradually by the effort of scientists.[140-145] Such as in 1984, Auson et al.[140] designed an integrated circuit version of the Hertzian dipole, using photoconductor as transmitting and receiving dipole antennas. In 1989, Exter and Fattinger et al.[141] improved transmitted beam power by more than 15 times, and the frequency response exceeded 1 THz.

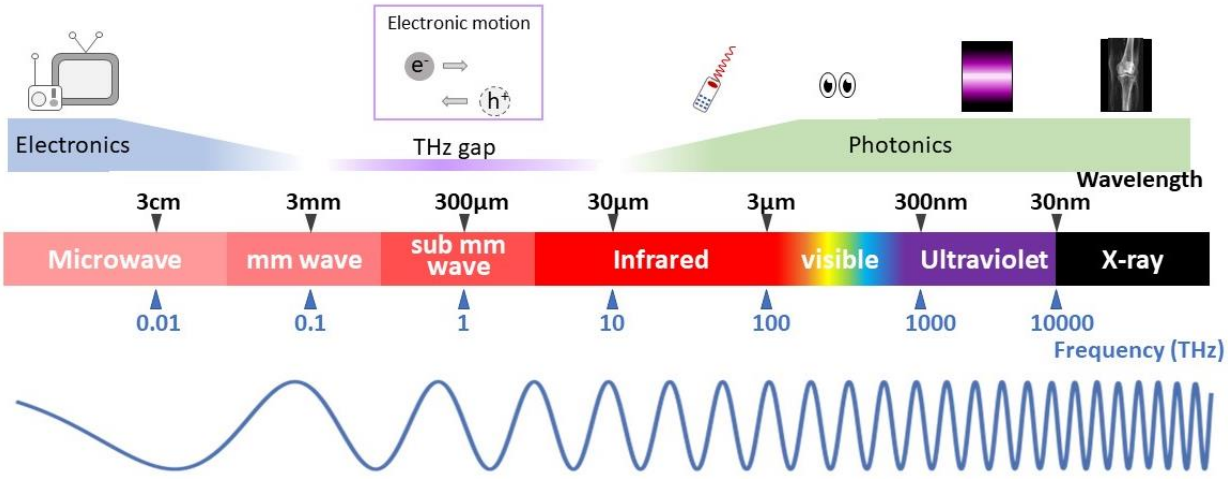

Figure 2.32. Spectrum of electromagnetic waves ranging from microwaves to X-ray waves. (Inserted picture is adapted with permission from European Radiology Experimental 2021, 5, 1-9.[146])

Because the energy of the motion of the charge carrier is in the range of THz frequency, the Thz radiation exhibit a distinct response to this motion. Furthermore, the time-domain THz spectroscopy can characterize the dynamic of charge carriers. The set-up of THz time-domain spectroscopy at MPIP is shown in Figure 2.33.

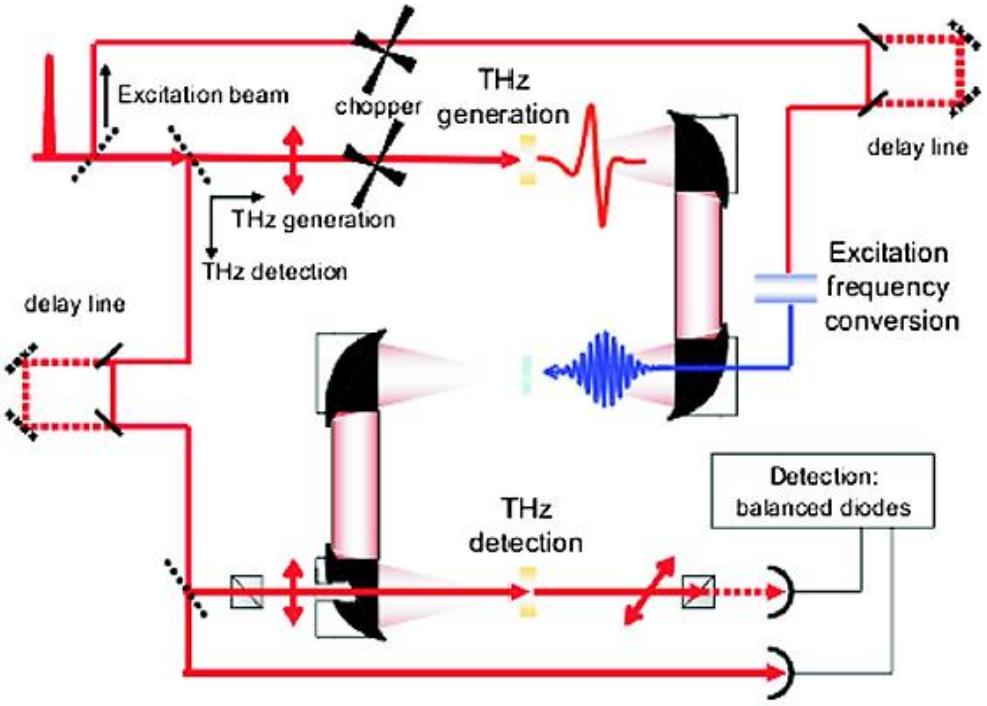

Figure 2.33. Schematic representation of an optical pump-THz probe experimental set-up. Figure is adapted with permission from Reviews of Modern Physics 2011, 83, 543.[147]

A Ti : sapphire laser pulses with the wavelength of 800 nm and duration of 50 fs enters the set-up and is split into three beams:

1. The excitation beam: this beam is used to photoexcited the sample. According to the experiment, it will travel through a chopper and delay stage to control the time of arrival at the sample.

2. The beam used for THz generating pulses: The generation of THz pulses is based on nonlinear optical rectification, a second-order optical process. A quasi-direct current (DC) or different frequency polarization is generated when a femtosecond pulse width laser beam propagates through a non-centrosymmetric media. ZnTe is used at MPIP to generate the 0.3 - 3 THz range. The THz pulses propagate through the sample, then meet the detection beam at the second ZnTe.

3. The beam used for generating detection of THz pulses: the detection of THz electromagnetic transients is based on Pockels electro-optic effect, which changes or produces birefringence in an optical medium induced by an electric field. The electric field related to

THz radiation plays the role of bias field, which induced the polarization change of the optical probe beam. The detector can detect this differential.

2.3.2 Charge carrier dynamics in semiconductor materials

In semiconductor materials, the energy levels of electrons are filled according to Fermi-Dirac distribution. The Fermi level is located in the middle of the valence band and the conduction band. In the fully occupied valence band, the electrons can not move to generate an electric current. When an electron obtains energy larger than band gap, it will be excited to a higher energy state in the conduction band, which is unoccupied. Now, these electrons can freely move and electrical conduction occurs.

Moreover, the created electron-hole pair can flow as charged particles as well. In thermal equilibrium conditions, the generation rate and recombination rates are balanced, resulting in a constant charge carrier density. There are three main types of recombination (as shown in Figure 2.34).

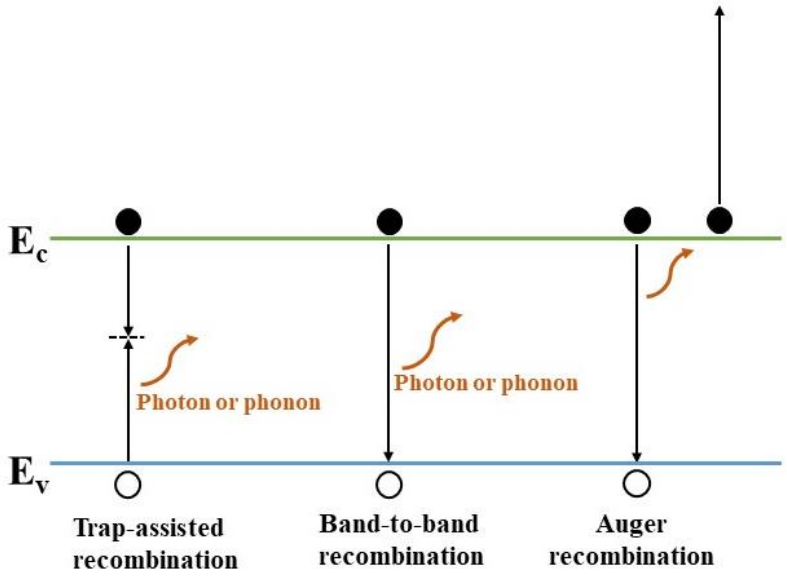

Figure 2.34. Carrier recombination mechanisms in semiconductors.

- Trap-assisted recombination: An electron or a hole is kept in place by a 'trap', an energy level within the bandgap generated by doped atoms or structural defects. The exchange of energy happens via lattice vibration.
- Band-to-band recombination: The electron in the conduction band recombines directly with a hole in the valence band with the energy being released in the form of photons.
- Auger recombination: An electron and hole recombine and give off the excess energy to a third carrier.

The charge recombination rates are related to these different order processes. Trap-assisted recombination is a first-order process, band to band recombination is a second-order process, and Auger recombination is a third-order recombination process. Therefore the charge carrier dynamics can fit Equation 2.2.[148] The relation between photoinduced conductivity and photoinduced charge carrier density is shown in Equation 2.3.[149] A THz pulse, used in the set-up shown in the last section, can only be absorbed by free electrons. Therefore, the relationship between the absorption of the THz electric field and the photoinduced conductivity can fit Equation 2.4.[150]

$$\frac{dn(t)}{dt} = -k_1 n - k_2 n^2 - k_3 n^3 \qquad Equation\ 2.2$$

n: the photoinduced charge carrier density

$$\frac{d\sigma}{dt} = e\mu \frac{dn}{dt} \qquad Equation\ 2.3$$

σ: the photoinduced conductivity;

e: electron charge;

μ: the intrinsic mobility of electrons.

$$\Delta\sigma = -\epsilon_0 c(n_A + n_B)\left(\frac{\Delta E}{E}\right) \qquad Equation\ 2.4$$

E: the amplitude of the THz electric field;

ΔE: the photo-induced transient THz absorption;

n_A, n_B: given refractive indexes of the surrounding materials;

ϵ_0: dielectric constant of vacuum;

c: the speed of light.

Since the mobility in the material can be regarded as constant, ΔE is in direct proportion to Δn. Therefore, we can characterize the carrier dynamics by optical-pump THz-probe spectroscopy and derivate the motion of the charge carrier.

2.4 Motivation and outline

As shown in the introduction, silver(I) has various coordination states and high stability constants with thiols. Therefore silver(I) thiolate coordination polymers can have a variety of structures and unique properties. This thesis aims to reveal new insights of silver(I) thiolate coordination polymers and to connect their optical and mechanical properties and their photogenerated charge carrier dynamics with their structural identity.

In **chapter 3**, the focus is on the synthesis and characterization of silver thiolate coordination polymers utilizing a wide range of mercapto compounds and solvents. The synthesis pathway, structure, chemical state of the elements and optical properties were studied in different stages and discovered that these silver thiolates possess reversible and temperature dependence blue-to-near infrared optical transitions. The analyses revealed that the structural flexibility of Ag-MPA is responsible for these transitions. The synthesis of silver thiolates with various mercapto compounds in a range of hydroxylated solvents was also systematically investigated. We found that the optical properties previously assigned to quantum confinement effects in Ag_2S nanocrystals synthesized by nearly-identical methods stem from silver thiolate coordination polymers.

In **chapter 4**, supramolecular gels were synthesized from highly concentrated silver thiolates (Ag-MPA).Their rheological properties of Ag-MPA were studied and further modifications to the synthesis method were applied in order to improve the quantum yield of NIR photoluminescence. The synthesized supramolecular coordination polymer gel exhibits a thermally reversible sol-gel transition and thixotropical properties. In order to improve their mechanical properties while maintaining their NIR photoluminescence, the supramolecular coordination polymer gels were blended with PVA during production. These hydrogels have the toughness of typical PVA gels and the optoelectronic properties of Ag-MPA. This extends the potential application range of this soft material.

In **chapter 5**, a high-quality Ag_2S film from easy to process Ag-MPA precursors was prepared. Ag_2S semiconductor materials are useful for applications ranging from photovoltaics to thermoelectrics. However, poor processability of Ag_2S makes the preparation of the thin films challenging and/or costly, which limits the research and application in optoelectronics and thermoelectrics. We discovered an innovative synthetic route towards highly uniform Ag_2S films with high crystallinity. Starting from water-based Ag-MPA solutions, These Ag-MPA

films were prepared by utilizing simple thin film techniques. These films were converted into high quality Ag_2S film by thermolysis. Together with my collaborators at MPIP we investigated the charge charrier dynamics in these films, revealing excellent properties even for free standing and flexible Ag_2S films.

.

3. Lamellar silver thiolate coordination polymers with reversibly switchable blue-to-NIR optical transitions.

Chapter 3 is based on an article which was accepted for publication in the journal *Journal of Materials Chemistry C* (DOI: 10.1039/d1tc01983j). The content is reproduced with permission from copyright 2021 Royal Society of Chemistry.

My contributions to the project are the synthesis of Ag-MPA coordination polymers, the purification of the samples, the measurement of the extinction, photoluminescence and FTIR spectra, the characterization by TEM and AFM, and the analysis and interpretation of the data. Robert Graf recorded, analyzed and interpreted the NMR data. The PXRD measurements were done by Michael Steiert, DSC measurements were done by Petra Räder, XPS measurements were done by Leon Prädel.

3.1 Introduction

Quantum dots (QDs) are semiconductor crystallites with diameters in the range of a few nanometers and properties stemming largely from quantum confinement effects. This includes a size-dependent optical band-gap.[151,152] Ag_2S QDs have attracted intense attention in recent years due to their narrow band gap (0.9-1.1 eV at 300K)[37, 38]and good biocompatibility. [153] Ag_2S QDs with tunable photoluminescence feature[27], ultralow cytotoxicity[154], strong emission in the NIR window are promising for biological applications, such as as imaging in vivo[155], drug delivery[156] and biosensors[26], since they allow for deeper tissue imaging than possible with visible light in addition to lower background photoluminescence and thus lower signal-to-noise ratios. [157]

Interestingly in literature, many Ag_2S QDs and nanoplatelets were prepared by nearly identical wet-chemical approaches,[27, 158, 159, 160, 161] utilizing $AgNO_3$ and 3-mercaptopropionic acid (MPA) as precursors and ethylene glycol as solvent, with reaction temperatures between 120-145 °C. According to literature, these protocols yield nanomaterials with a variety of polymorphs, sizes, and shapes while at the same time exhibiting nearly identical optical features such as first absorption peaks at ~800 nm.

These results seem to be at odds with the idea of quantum confinement, since the variety in sizes (e.g. QDs with diameters of ~6.3 nm [12]) and shapes (e.g. nanoplatelets with thicknesses of 0.35 nm[159]) should lead to distinctively different optical properties. Equally puzzling are the reports on nearly identical optical properties for α-Ag_2S[12] and β-Ag_2S[159, 161] nanomaterials, because only the low-temperature monoclinic α-Ag_2S (acanthite) phase exhibits semiconducting properties.[162] In other words, while the optical properties are extremely interesting for a variety of applications, it is unclear to date what kind material really is generated by syntheses utilizing $AgNO_3$ and MPA precursors in ethylene glycol.

We investigated the synthesis systematically by changing the molecular structure of the mercapto compounds and the solvent, while keeping the $AgNO_3$ precursors unaltered. We found out that the materials formed are predominantly lamellar Ag-MPA coordination polymers. Their optical properties are connected to the structural flexibility that can be addressed by temperature. We find that our Ag-MPA coordination polymers display a reversible blue-to-NIR optical transition that is reversible over many cycles. Thus, our study not only reveals that the characteristic optical properties of the materials stemming from the synthesis from $AgNO_3$ and MPA in ethylene glycol are related to an Ag-MPA coordination polymer rather than quantum confinement effects in Ag_2S nanocrystals. It also opens up many new possibilities for applications that can make use of the temperature dependent, fully reversible optical transitions, spanning the blue-to-NIR range. Furthermore, the polymeric nature of Ag-MPA allows for facile scalability to multi-gram syntheses. Due to the polymeric nature of Ag-MPA, we further expect significant advantages in the processing of our Ag-MPA coordination polymers over colloidal quantum dots for solid-state applications.

3.2 Experimental part

Chemicals: All reagents were purchased and used without further purification. Silver nitrate (Sigma-Aldrich, BioXtra, >99%), 3-mercaptopropionic acid (Aldrich, ≥99%), ethylene glycol (Acros organics, 99.5%, for analysis), 1,3-propanediol (VWR, for synthesis), 1,4-butanediol (Merk KGaA, for synthesis), 1,5-pentanediol (Merk KGaA, for synthesis) and 1,6-hexandiol (Alfa Aesar, 97%), glycerol (Alfa Aesar, 99+%), acetone (Fisher Chemical, >=99.8%), 3-mercapto-1-propanol (Aldrich Chem. Co., 95%), methyl 3-mercaptopropinate (Acros organics, 98%), 1-hexanethiol (Aldrich, 95%), 12-mercaptododecanoic acid (Aldrich, 96%), Polyglycerol polyricinoleate (Danisco, Grindsted PGPR 90 kosher), toluene (Fisher, >=99.8%), indocyanine green (ICG, Roth, p.a.), Dimethyl sulfoxide (Merk, dried).

Methods:

Synthesis of Ag-MPA(UV): The Ag-MPA coordination polymer was prepared modifying the procedure published by Jiang et al.[158] and Kubie et al.[159] Briefly, 0.022 g of $AgNO_3$ (0.125 mmol) and 25 mL of ethylene glycol were added into a 100 mL 3-neck-flask. The mixture was degassed under vacuum while stirring at 50 °C for 30 min in order to remove water and oxygen dissolved in ethylene glycol. After stopping the vacuum and putting the flask to argon, 22 μL of 3-mercaptopropionic acid (0.25 mmol) was injected into the flask and the temperature was set to 130 °C. The colorless solution changed to cloudy white immediately, then started to change to orange gradually when reaching around 130 °C. The reaction was allowed to proceed for 10 min at 130 °C. Afterwards, the mixture was cooled to room temperature using a water bath to obtain orange sample Ag-MPA(UV). The subsequent purification steps were described in the purification section below.

Synthesis of Ag-MPA(NIR): In order to obtain stable Ag-MPA(NIR) coordination polymers with the near infrared photoluminescence, the synthesized orange Ag- MPA(UV) sample was kept heating at 130 °C, between the 10 to 25 min, the orange solution changed to brown gradually, if Ag-MPA solution was cooled down to room temperature during this period of time, it would come back to orange state. When keep heating for longer time, ~ 30min, Ag-MPA solution can stay at the brown state with NIR photoflourescence. Then the solution was cooled to room temperature using a water bath. The subsequent purification steps were described in the purification section below.

Synthesis of Ag-MPA at 15 times higher precursor concentration: The synthesis method was almost the same as the one above with increased amount of $AgNO_3$ and MPA. 0.33 g $AgNO_3$ (1.875 mmol) and 330 μL of 3-mercaptopropionic acid (3.75 mmol) were used in this experiment. After the mixed solution reached 130 °C, the reaction was allowed to proceed for 5 min, then cooled to room temperature to obtain orange sample Ag-MPA(UV). When keep heating for longer 5 min, the brown Ag-MPA(NIR) sample can be obtained after cooling to room temperature.

Synthesis of Ag-thiolates from various solvents: The synthesis methods of the reaction in different solvents were similar to the method above. Ethylene glycol was replaced by either 1,3-propanediol, 1,4-butanediol, 1,5-pentanediol, 1,6-hexandiol or glycerol, and the final heating temperature were set to 140 °C, 150 °C, 155 °C, 155 °C, and 130 °C, respectively. The reaction proceeded at the final temperature for ~30 min Then the heating mantel was removed and the mixture was cooled to room temperature with a water bath.

Synthesis of Ag-thiolates with various ligands: The synthesis methods of the reactions with different thiol ligands were similar to the method above. 0.022 g of $AgNO_3$ (0.125 mmol) and 25 mL of ethylene glycol were added into a 100 mL 3-neck-flask. After the mixture was degassed and the flask was put to argon and 0.25 mmol of different thiol ligand was injected. For 3-mercapto-1-propanol, methyl 3-mercaptopropinate, 1-hexanethiol, and 12-mercaptododecanoic acid, the temperature was set to 160 °C, 130 °C, 175 °C and 175 °C respectively. The reaction proceeded for 30 min at the corresponding reaction temperature. The mixture was then cooled to room temperature using a water bath.

Purification: 30 mL of acetone was added to 5 mL of reaction solution in a 50 mL centrifuge tube. After shaking the centrifuge tube, larger fiber-like structure flocculated from the solvent. The mixture was centrifuged for 5 min at 7000 rpm, the clear supernatant was discarded and the precipitated was washed by acetone at least two more times. Then the precipitated was dried in a vacuum oven at 50 °C for 8 h.

When needed for analysis, the purified powder was dissolved in Milli Q water to obtain a clear aqueous solution.

Preparation of Ag-MPA toluene emulsion: 0.5 g of Polyglycerol polyricinoleate (PGPR) was mixed with 30 ml toluene, then mixed with 7 mL of Ag-MPA aqueous solution (~0.1 wt%) under stirring. Then the mixture was pre-emulsified for 2 min with an Ultra-Turrax at 15000

rpm. Finally, the pre-emulsified mixture was passed through a microfluidizer (LM, Microfluidic corp) equipped with a F20Y interaction chamber with channels of 75μm at a pressure of 10000 PSI for two cycles.

Characterization:

Transmission electron microscopy. TEM samples were prepared by drop-casting the aqueous solution onto a carbon coated copper grid. Routine TEM imaging was done using JEOL1400 TEM with an acceleration voltage of 120 kV.

X-ray diffraction. Purified powder was used to perform XRD. Powder XRD patterns were collected on a Rigaku SmartLab Diffractometer, operated with a Cu Kα radiation source (1.540593Å) with increment steps of 0.01° at 0.3°/min.

Absorption measurements. 200 μL original solution was dispersed in 3 mL ethylene glycol to measure the absorption spectra. The absorption spectra were recorded on an Agilent Cary 60 Spectrophotometer.

Photoluminescence measurements. 200 μL original solution was dispersed in 3 mL ethylene glycol to measure the photoluminescence spectra. Photoluminescence spectra were recorded using a J&M TIDAS diodearray pectrometer with an XBO-lamp as excitation source.

Differential scanning calorimetry. Purified powder was used to perform DSC on a Mettler Toledo DSC823 under N_2 flow, cycling from room temperature to 150 °C and back at a heating/cooling rate of 5 °C/min.

X-ray photoelectron spectroscopy. A purified aqueous solution was drop cast on a silicon wafer to perform XPS measurement on an Axis Ultra DLD by Kratos Analytical spectrometer. XPS data were collected with the anode at 10 mA and 15 kV; the analyzer was kept in hybrid mode and the resolutions was 80 eV pass energy for the survey scans and 20 eV pass energy for the high resolution scans. The binding energy (BE) scale was referenced to the value of 284.8 eV for the C 1s peak.

Atomic force microscopy. AFM samples were prepared by drop-casting the water solution onto the a silicon wafer on the heating plate set to 90 °C. AFM was performed on a Dimension Icon FS AFM in tapping mode with a scan rate of 0.595 Hz.

Solid state nuclear magnetic resonance (NMR). Solid state NMR measurements have been performed at 700.25 MHz ^{1}H Larmor frequency and 25 kHz magic angle spinning (MAS) frequency with a Bruker Avance III console using commercial double resonance probe supporting zirconia rotors with 2.5 mm outer diameter. The radio frequency power for signal excitation and decoupling has been adjusted on both frequency channels, ^{1}H and ^{13}C, to a nutation frequency of 100 kHz corresponding to a duration of 90° excitation pulses of 2.5 µs. The ^{13}C CP-MAS NMR measurement have been performed with 10% amplitude variation on the ^{1}H channel and 1-3 ms CP contact time using the swf-TPPM decoupling scheme for high power ^{1}H decoupling during acquisition.[163] All NMR experiments have been performed under ambient conditions, corresponding to a sample temperature 45 °C under the fast MAS conditions which has been determined based on the temperature dependent chemical shift of lead nitrate in separate experiments for temperature calibration.[164,165]

3.3 Results and discussion

3.3.1 Study of the reaction process

A typical synthesis of NIR-photoluminescent materials consist of mixing $AgNO_3$ with ethylene glycol. The process is executed under vacuum conditions and at room temperature. The addition of MPA to the mixture is performed under argon atmosphere with step-wise temperature increase up to 130 °C. The reaction was monitored for a period of 2 hours by means of optical spectroscopy and powder X-ray diffraction (PXRD) (see Figure 3.1).

The synthesis can be divided into four distinct stages. The first stage covered the period immediately after injecting the thiol ligand MPA into the silver nitrate containing ethylene glycol. This led to a change in color of the solution from transparent to cloudy white. The second stage was the gradual increase of temperature to 130 °C and the subsequent change in color of the product to orange. The third stage was focused on continuously heating the product at 130 °C for a period of 10 to 25 minutes. The continuous heating led to another change in color of the product to brown. And the last fourth stage consisted of additional heating of the sample for an extended period of time until the color of the product was black.

A first aliquot, a white dispersion, was removed from the flask during the first stage of the process. This first aliquot did not show any absorption and photoluminescence peaks (see Figure 3.1 a). PXRD measurements revealed regular diffraction signals at 6.6°, 13.3° and 20.1° (see Figure 3.1 b). This diffraction pattern can be interpreted in terms of a crystal structure in which the Ag and S atoms occur in regularly stacked layers with a relatively large interlayer distance.[166] Layered Ag thiolate structures are well known in literature.[71,167] The intra-layer Ag-thiolate ligands arrangement is usually quasi-hexagonal, with the thiolate terminating both sides of the layers.[168-171] Calculated by Bragg's law, the stacking distance of our first aliquot is ~13.3 Å. The ^{1}H MAS NMR spectrum of the first aliquot shows the expected signals of the aliphatic MPA sites and a sharp peak at ~13 ppm (see Figure 3.1 c, first row) assigned to acidic protons, which show a strong auto-correlation signal in ^{1}H double-quantum correlation spectra (see Figure 3.2) indicating the formation of acid dimers. In the ^{13}C CP-MAS NMR spectrum (Figure 1 d, first row), only the three carbon sites of MPA (COOH ~180 ppm, CH_2 ~39 ppm, S-CH_2 ~32 ppm) were observed, while the presence of ethylene glycol in stage I can be safely excluded. The chemical shift value of 39 ppm of the MPA carbon site C(2) indicates that the

central carbon site of all MPA molecules in the stage I aliquot is present in *gauche* conformation, which led to a bent shape of the molecule. Assuming, that the C-S bond of MPA is oriented perpendicular to the Ag-S layer, thus indicates that the formed acid dimers do not connect MPA molecules of neighboring Ag-S layers, but are intra-layer dimers oriented parallel to the Ag-S layer.

When the temperature reached 130 °C, the solution changed to bright orange gradually as a result of the second stage of the reaction. This change led to formation of two absorption shoulders at ~390 nm and ~457 nm in the adsorption spectra [see Figure 3.1 a; this orange material will be referred as Ag-MPA(UV) from now on]. These two absorption bands are associated with a donor-acceptor charge transfer from sulphur atoms to silver ions[173] and metallophilic attraction between silver atoms in Ag-MPA(UV) coordination polymer.[174] Therefore, the absorption spectra are determined by the thiolate ligands and the related ligand-to-metal charge transfer (LMCT) and modified by the presence of the Ag-Ag interactions, leading to ligand-to-metal-metal charge transfer (LMMCT).[88]

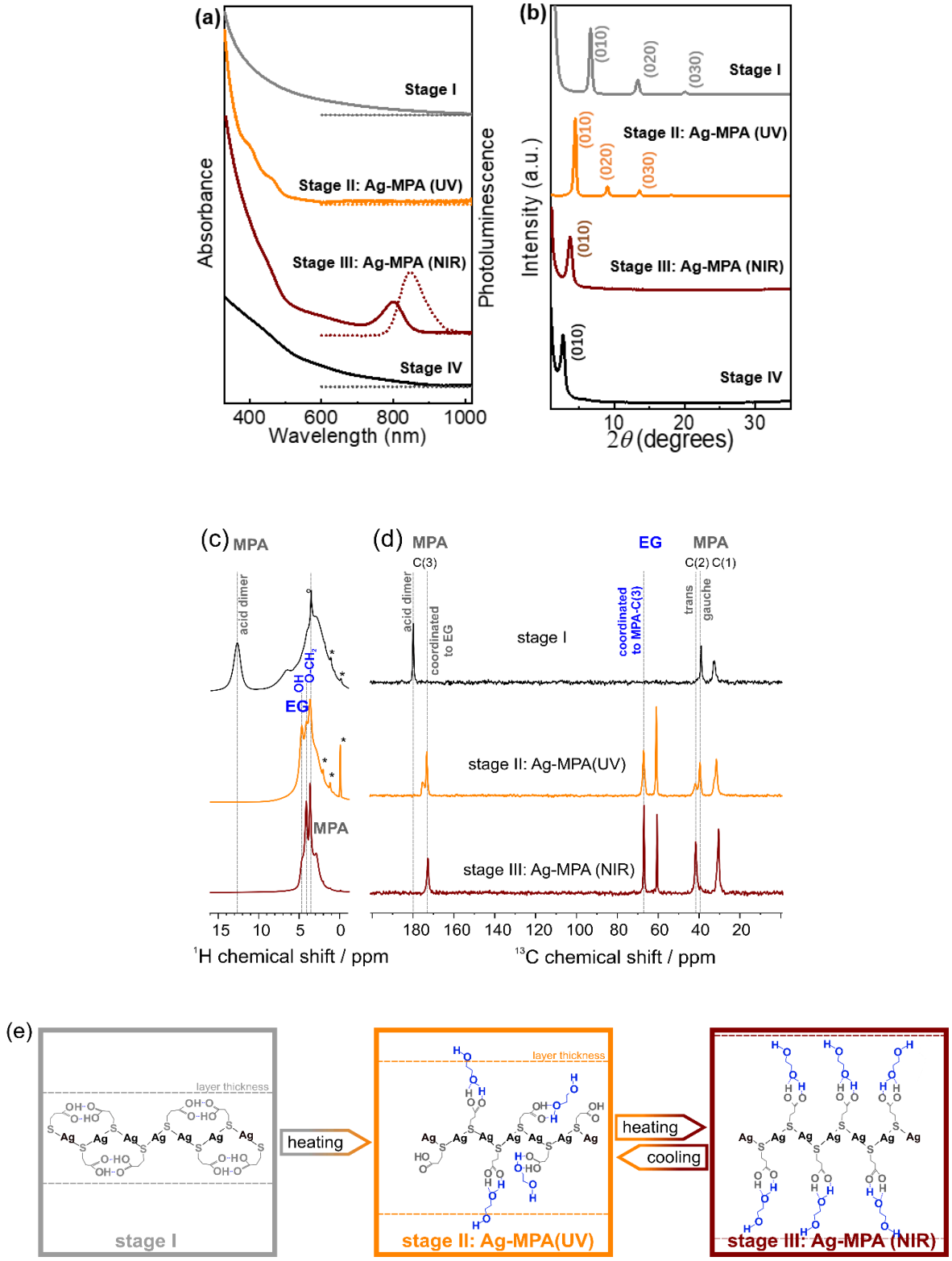

Figure 3.1. (a) Absorption spectra (solid lines) and photoluminescence spectra (dash lines), (excited at 380nm); (b) PXRD patters; (c) ^{1}H MAS NMR spectra (asterisk mark the contamination with silicon grease and residual solvent); (d) ^{13}C NMR spectra; (e) scheme of structures at different reaction stages.

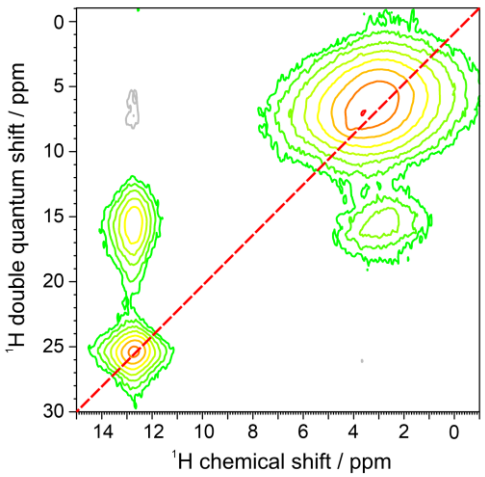

Figure 3.2. 2D ^{1}H double quantum correlation NMR spectrum of the stage I aliquot, recorded at 700 MHz ^{1}H Larmor frequency and 25 kHz MAS using one rotor period of xy16-BABAfor double quantum excitation and reconversion.[172] The intense correlation signal at 12.8 ppm ^{1}H chemical shift and 25.6 ppm ^{1}H DQ shift observed with only 40 µs DQ excitation is a direct proof for the formation of stable acid dimers in the aliquot stage I.

Similar to aliquot I, the PXRD of aliquot II displayed also a layered structure, but the stacking distance increased to ~20 Å (see Figure 3.1 b). In the ^{1}H MAS NMR spectrum of aliquote II, the acid signal at ~13 ppm of MPA dimers disappeared, indicating the opening of the hydrogen bonded MPA dimers during heating, while three distinct signals assigned to ethylene glycol sites are observed in the range from 3.5 – 5 ppm. At the same time, the ^{13}C NMR signal of the acid dimers shifts to higher fields and splits into a broader signal at 175 ppm assigned to free acid groups and a narrow signal at 172 ppm of acid sites coordinated to ethylene glycol. The new methoxy signal of ethylene glycol (EG) in the aliquot II splits as well, into a signal at ~67 ppm of methoxy sites coordinated to MPA-acid groups and free EG methoxy groups at ~60.5 ppm. The signal assigned to MPA C(2) splits as well and shows the signal of the *trans* conformation of MPA at ~42 ppm. The relative intensities of the two signals *gauche : trans* is 2:1 indicating a statistical population of the two conformations. Both the presence of MPA in the elongated *trans*-confirmation as well as the incorporation of EG into the layered structure of Ag-MPA(UV) resulted in an increasing inter-layer distance compared to the structure of stage I as confirmed by PXRD. The TEM micrographs and AFM images revealed a web-like arrangement (see Figure 3.3 and Figure 3.4).

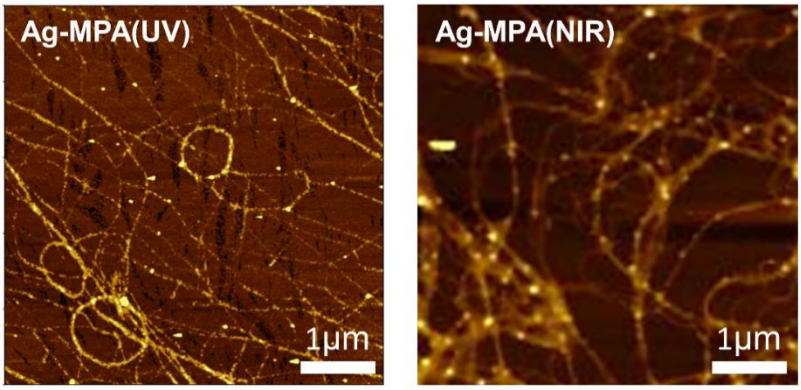

Figure 3.3. AFM images for Ag-MPA(UV) and Ag-MPA(NIR)

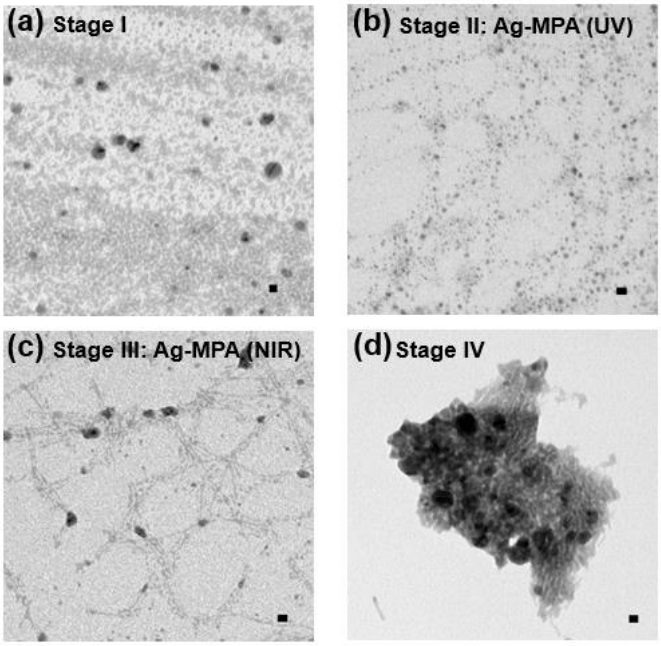

Figure 3.4. TEM micrographs of Ag-MPA samples at the four stages. Scale bars are 10 nm.

When the sample was continuously heated at 130 °C for a period of 10 to 25 minutes, the color changed to brown. In this third stage, the two shoulders in the UV range became weaker and an obvious absorbance peak at ~800 nm appeared with a corresponding photoluminescence at ~840 nm [see Figure 3.1a; this material will be referred as Ag-MPA(NIR) from now on].

The ^{13}C CP-MAS NMR spectra of Ag-MPA(NIR) showed that all MPA molecules have been transferred from lateral space filling *gauche* conformation to the fully elongated *trans* conformation and are coordinated to EG by hydrogen bonding as indicated by the single, narrow carbonyl signal at 172 ppm. Therefore, the interlayer distance increased upon the transformation

of Ag-MPA(UV) to Ag-MPA(NIR). The ^{1}H MAS NMR spectra showed, that the molecular order of coordinated ethylene glycol molecules increases substantially at this transition, going from a disordered state with broad O-CH_2 signals and narrow signals of free OH groups (around ~4 ppm) to an ordered state with sharper O-CH_2 signals and a broad shoulder of hydrogen bonded, less mobile OH groups. The PXRD revealed that the higher order reflections disappeared and the remaining broadened first order peak shifts to ~3.7°, related to the stacking distance of 23.8 Å. This could indicate that the main structure of the layer is maintained, but the long-range periodicity of the stacked lamellar structure is strongly reduced. We assume that the altering of argentophilic interactions was causing a lateral contraction of the Ag-S layer which was the reason for the change of the optical properties. The lateral contraction of the attached ligand forced the MPA molecules into the entropically unfavorable all-*trans* state and led to an increasing inter-layer distance. It is difficult to imagine that this argentophilic lateral contraction of the two-dimensional coordination polymer can occur without any local breaking of the Ag-S layer, and thus reducing its size. The stacking of smaller two-dimensional objects, however, leads to a reduced stacking periodicity as observed by the PXRD.

Importantly, we did not observe any signs of Ag_2S diffraction signals, yet the material displayed the typical absorption and emission features often attributed to quantum confined Ag_2S nanocrystals.[27, 158-161] This indicated, that the characteristic optical properties (absorbance peak at ~800 nm) of materials produced by the reaction of $AgNO_3$ and MPA in ethylene glycol stem from Ag-MPA coordination polymer and not from Ag_2S nanocrystals. Interestingly, TEM and AFM analyses revealed that the web-like structure is even more visible than for aliquot II, the orange Ag-MPA(UV) (see Figure 3.3 and Figure 3.4). We want to emphasize that the obtained Ag-MPA(UV) and Ag-MPA(NIR) materials were all very sensitive to the electron beam, as we observed a gradual increase of particle-like structures with increasing exposure time. This could be the origin of miss-interpretation of the NIR absorbance feature at ~800 nm to stem from Ag_2S nanocrystals as they could form in-situ in the electron microscope. In order to compare our results to the literature[27, 158-161], we also synthesized silver thiolates with different Ag:S ratios (1:2 and 1:20) and reaction temperatures (130 °C and 145 °C). Nearly identical NIR optical features were observed in all cases (see Figure 3.5).

TEM images of Ag-MPA(NIR) synthesized at 145 °C showed some small round particles that might be Ag_2S particles, besides the typical fiber-like structure. However, compared synthesized at 130 °C that do not show these small particles, their optical features are the same.

In order to avoid significant transformation of Ag-MPA to Ag_2S moderate reaction parameters are benefical, such as lower temperatures (130 °C instead of 145 °C) (see Figure 3.5).

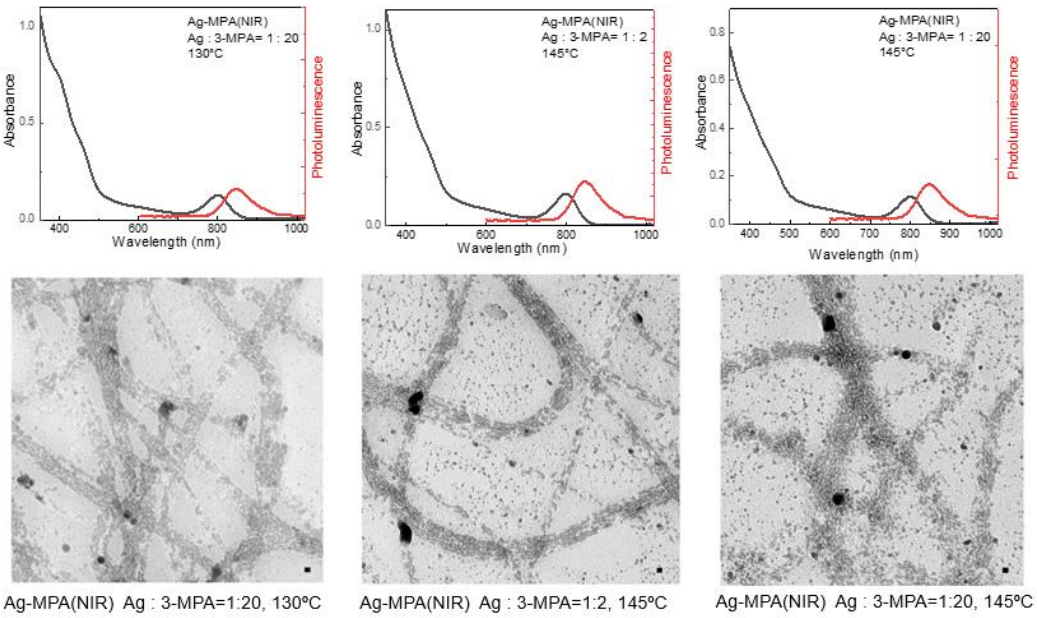

Figure 3.5. Absorption and photoluminescence spectra and TEM micrographs for Ag-MPA(NIR) synthesized at different temperature with different precursor ratios. Scale bars are 10 nm.

When we kept heating at 130 °C for 50 min, the absorption feature at 800 nm and the NIR photoluminescence feature, together with the web-like structure, disappeared (see Figure 3.1). The PXRD showed a single signal at 2.8° and only traces of monoclinic α-Ag_2S around 30-40° (see Figure 3.1 and Figure 3.6).

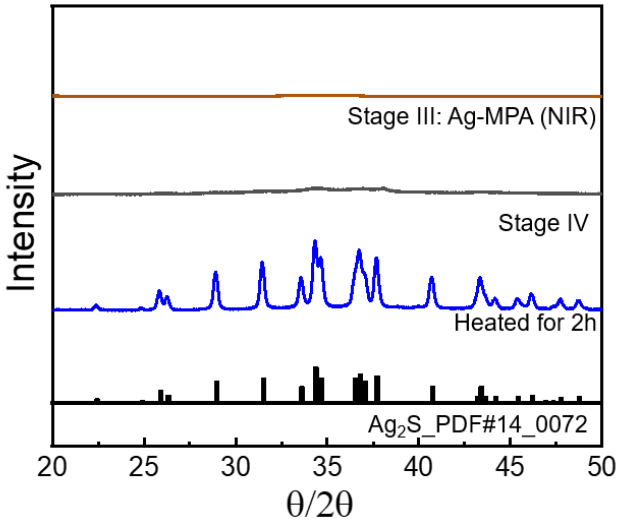

Figure 3.6. PXRD patterns of samples Ag-MPA(NIR), Stage IV, 2 h heated sample and Ag2S_PDF#14_0072.

Only when heated for several hours a black precipitation with the clear diffraction pattern of monoclinic Ag_2S was obtained (see Figure 3.6). The growing Ag_2S nanodisks are shown in Figure 3.7.

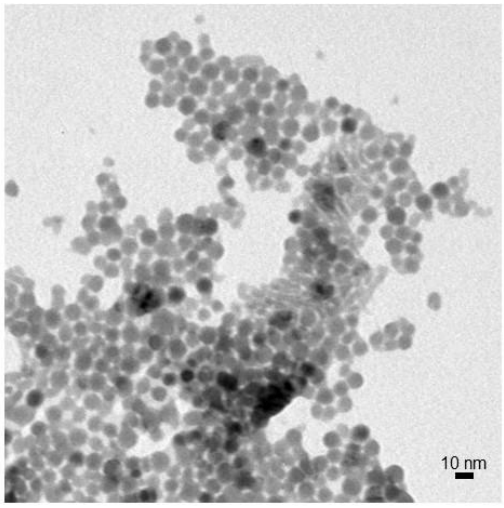

Figure 3.7. TEM micrographs Ag_2S nanodiscs obtained by heating Ag-MPA for 2h at 130 °C.

3.3.2 Reversible optical transition in Ag-MPA

While studying the transition from Ag-MPA(UV) to Ag-MPA(NIR), we noticed that if the heating process was stopped early (between 15 min to 25 min heating at 130 °C), the brown Ag-MPA(NIR) sample would revert back to orange Ag-MPA(UV) during the cool-down to room temperature. This observation is a second indication that the optical properties are most likely not stemming from Ag_2S nanocrystals for which such reversible optical properties are unknown. We followed this transformation optically by absorption spectroscopy during the cool-down process from 130 °C (see Figure 3.8 a). The absorption peak at ~800 nm decreased and blue shifted during the cooling process and ultimately completely disappeared. When heated to 130 °C again, the optical properties of Ag-MPA(NIR) were fully restored. This heating-cooling cycle can be repeated at least five times without any significant loss of the reversibility of the characteristics (Figure 3.8 b). Unfortunately, because of the thermal fluorescence quenching, during the temperature increase, we could not measure the PL spectra for hot Ag-MPA(NIR).

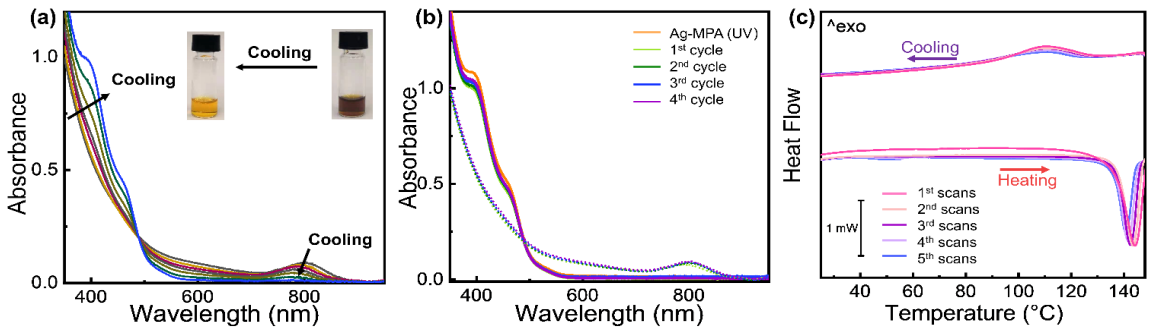

Figure 3.8. Absorption spectra of (a) Ag-MPA continuously measured during the cooling from 130 °C to room temperature. (b) Ag-MPA measured during several cycles of heating and cooling; the solid linse show the room temperature absorbance, the dash lines shows the absorbance at 130 °C. (c) Differential scanning calorimetry (DSC) curves of Ag- MPA(UV) powder for five continuous cycles at heating/cooling rates of 5 K·min^{-1}.

The reversibility of the transition from Ag-MPA(UV) to Ag-MPA(NIR) and back was confirmed by differential scanning calorimetry (DSC) (Figure 3.8 c). We cycled the temperature between 25 °C and 150 °C with heating and cooling rates of 5 °C/min. During the first heating we measured an endothermic peak at ~143 °C with an energy of 195.52 mJ and upon cooling

to an exothermic peak at ~109 °C with an energy of 79.39 mJ (Figure 3.8 c). This indicated that Ag-MPA(UV) converts to Ag-MPA(NIR) at ~143 °C and then partially returns to Ag-MPA(UV) at ~109 °C. This transformation seemed to be kinetically limited, since the exothermic peak was most likely related to the reorganization of the layered Ag-MPA sheets into ordered super structures did not coincide with the endothermic peak at ~143 °C of the transition from Ag-MPA(UV) to Ag-MPS(NIR). We could speculate that this created some structural hysteresis, which might be also the reason that the integrated peak area decreased with every cycle.

We also studied how the pH value affects the solubility of the Ag-MPA(UV) in water (see Figure 3.9). We found out that the solubility is dependent on the pH value. Low pH values led to a lower solubility. When the pH value is 1.2, Ag-MPA precipitates completely and sinks to the bottom of the flask. A possible reason is that the extra protons suppressed the ionization of the carboxyl group in MPA. With the increase of the pH value, the Ag-MPA dissolved much faster, and the solution became clearer. When the pH value reached 12.5, after 3 h, the color of the aqueous solution changed from yellow to brown, and there a peak at 800 nm appeared in the absorption spectra (Figure 3.9). This indicates that the transition from Ag-MPA(UV) to Ag-MPA(NIR) also can be triggered by pH value.

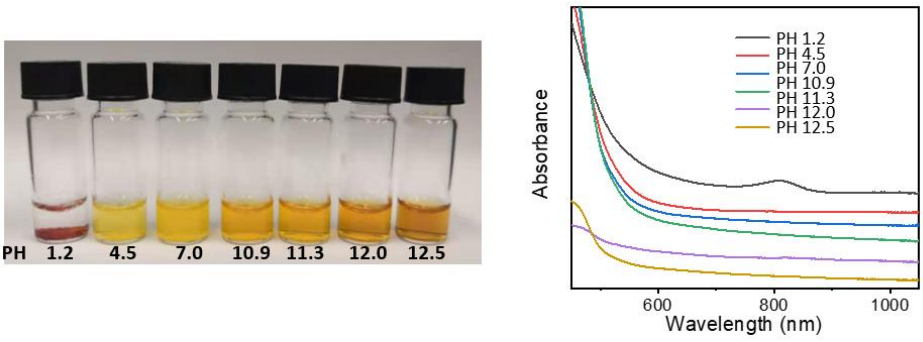

Figure 3.9. The absoption spectra of Ag-MPA(UV) in different pH values.

3.3.3 Chemical states of C, S, and Ag in Ag-MPA(UV)/(NIR)

We further used X-ray photoelectron spectroscopy (XPS) to shed some light on the chemical states of C, S and Ag for Ag- MPA(UV) and Ag-MPA(NIR) (see Figure 3.10 and Figure 3.11

for survey scans). Purified Ag-MPA(UV) water solution was dropped on two pieces of silicon wafers. Then one of the wafers was heated to 130 °C, to obtain Ag-MPA(NIR). For analysis of the data, the standard spin-orbit splitting of 1.18 eV and a branching ratio of 2:1 (S $2p_{3/2}$: S2 $p_{1/2}$) was used to fit the S $2p_{3/2,1/2}$ doublet. S 2p spectra analysis points out three distinct chemical states for both S in Ag-MPA(UV) and Ag-MPA(NIR). The S $2p_{3/2}$ signal occurring at ~162.1 eV is the main contributor of the overall S population, associated with an Ag-S-R structure, which is normally detected in silver thiolate.[170, 175] At lower binding energy the peak at ~161.2 eV can be associated with S $2p_{3/2}$ Ag_2S,[176] which takes around 27% in the whole content of sulfur. We did not observe these Ag_2S traces in the PXRD experiments. This could be due to an amorphous character or because the Ag_2S in the XPS was formed in situ during the high vacuum processing and X-ray exposure during the measurement. Finally, the spin-orbit pair at higher binding energy (S $2p_{3/2}$ ~163.5 eV) is associated with free thiol group.[175,176] In the Ag-MPA(UV), there is a small amount of free thiol groups (~6%), most likely stemming from physical adsorbed, unbound MPA. In the Ag-MPA(NIR), there is more free thiol group (~13%).[177] This could imply that during the heating of Ag-MPA(UV) to obtain the Ag-MPA(NIR), MPA is partially released from Ag-MPA(UV).

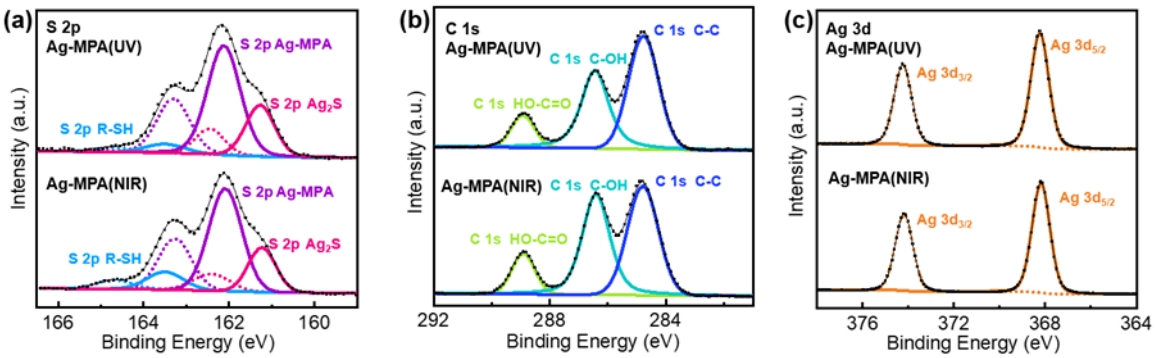

Figure 3.10. High-resolution XP-spectra of Ag-MPA(UV) and Ag-MPA(NIR) (a) S 2p, solid lines represent the signals stemming from S $2p_{3/2}$, dash lines represent the signals stemming from S $2p_{1/2}$,; (b) C 1s; (c) Ag 3d, solid lines represent the signals stemming from Ag $3d_{5/2}$, dash lines represent the signals stemming from Ag $3d_{3/2}$..

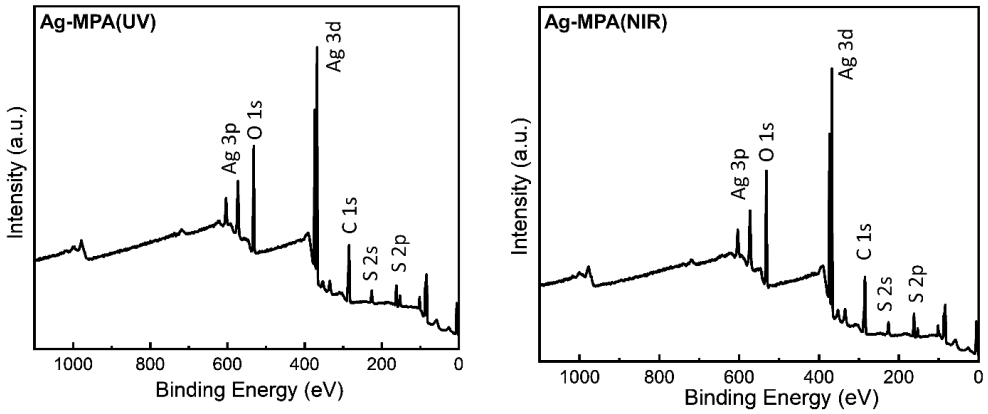

Figure 3.11. Overall XPS survey spectra for Ag-MPA(UV) and Ag-MPA(NIR)

The standard spin-orbit splitting of 6 eV, and branching ratio of 3:2 ($Ag3d_{5/2}$: $Ag3d_{3/2}$) was used to fit the Ag $3d_{5/2,3/2}$ doublet. For the main signal, Ag $3d_{5/2}$ is centered at 368.2 eV, but the peak separation of Ag, Ag-S-R, Ag_2S is too small to be appreciated.[177]

The C 1s spectra exhibit the emission bands at 284.8 eV, 286.4 eV and 288.9 eV. In MPA, there are three types carbon atoms. The signal at ~288.9 eV can be attributed to the carbon atom in the COOH group.[178] The difference in binding energy for the carbon atoms in the position of S-C-C and C-C-C is too small to be appreciated.[179] There is a strong peak in the C 1s spectra at 286.3 eV attributed to C-OH, which stems from ethylene glycol. The ratio of C-OH:COOH in Ag-MPA(UV) is 2.4:1 and in Ag-MPA(NIR) is 2.6:1, which reflects a ratio of ethylene glycol:MPA only slightly larger than 1 (there are two C-OH in EG and one COOH in MPA, the theoretical ratio for ethylene glycol/MPA would be 2:1). This is in agreement with the NMR results that showed a layer of ethylene glycol molecules interconnects to the MPA layer. This interconnection is achieved through hydrogen bonds, and both Ag-MPA(UV) with MPA in mixed conformation and Ag-MPA (NIR) with MPA in pure *trans* conformation had almost the same chemical states of Ag, S, and C.

The XPS results demonstrate that within the material, Ag-MPA(UV) and Ag-MPA (NIR) have almost the same chemical states of Ag, S, and C, but the ratio of bound/unbound MPA changes slightly during the heating process that is required to transform the non-photoluminescent Ag-MPA(UV) into NIR-photoluminescent Ag-MPA(NIR). This result was also confirmed by FTIR spectroscopy (see Figure 3.12). The sharp signal at 1714 cm^{-1} is attributed to the C=O bonds of carboxylic acid groups from MPA and the absence of the S-H signal indicates that MPA is bound to Ag. The broad peak at around 3386 cm^{-1} is attributed to

the -OH from ethylene glycol and only present in samples of stages II-IV (see Figure 3.1 a and b). Thus, in conclusion, the different optical properties in Ag-MPA(UV) and Ag-MPA(NIR) do not stem from differences in the chemical state but most likely is tuned by the (temperature dependent) metallophilic interaction between silver atoms.[88]

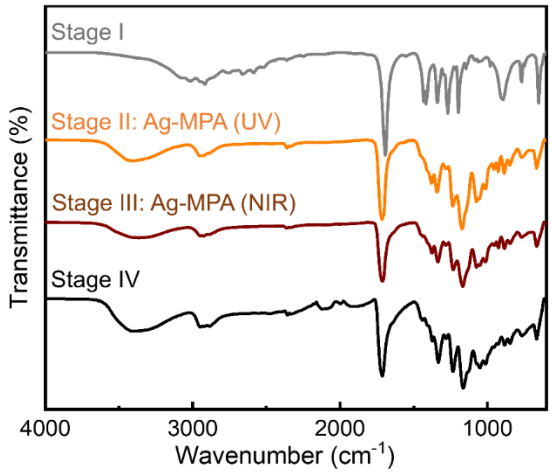

Figure 3.12. FTIR spectra for the four stages samples.

3.3.4 Study of various ligands and solvents

In order to evaluate their importance on the appearance of the NIR feature in Ag thiolate coordination polymers, we assessed a broad range of different ligands and solvents (see Figure 3.13 and Figure 3.14). Our experiments on the various ligands revealed that for a successful synthesis of Ag thiolates with NIR optical properties mainly the proper coordination between Ag^+ and thiol group is crucial. We could show that the group terminating each Ag thiolate layer can be substituted, covering a broad range from CH_3 to COOH. We also found that the lengths of the ligand is not of great importance as Ag-12-mercapotundecanoic acid shows nearly identical optical properties to Ag-3-mercaptoproprionic acid. However, the solubility of the coordination polymers can be conveniently adjusted by the choice of the ligand lengths and end group. Moreover, quantum yield (QY) decreases with the decrease of solubility. The QY of Ag-MPA(NIR) is 5.38%, Ag-3-mercapto-1-propanol is 5.35%, Ag-methyl 3-mercaptopropionate is 2.47%, Ag-12-mercaptododecanoic acid is 1.02% and Ag-1-hexanethiol is 0.53% (see Table 3.1).

Table 3.1. The quantum yield(QY) of Ag thiolate with different ligands.

Sample	Slope	Solvent	$\eta_{solvent}$ (the refractive index of solvent)	QY (%)
ICG	294213	DMSO	1.479	10.6
Ag-MPA(NIR)	159596	EG	1.431	5.38
Ag-3-mercapto-1-propanol	158837	EG	1.431	5.35
Ag-methyl 3-mercaptopropionate	73385	EG	1.431	2.47
Ag-12-mercaptododecanoic acid	30370	EG	1.431	1.02
Ag-1-hexanethiol	15633	EG	1.431	0.53

The QYs in Table 3.1 obtained relative to an ICG standard solution and calculated with Equation 3.1.

$$QY_{sample} = QY_{standard}\left(\frac{Slope_{sample}}{Slope_{standard}}\right)\left(\frac{\eta_{sample}}{\eta_{standard}}\right)^2 \qquad \text{Equation 3.1}$$

The slope is calculated from the linear fit of integrated absorption against integrated photoluminescence of silver thiolate and ICG reference at different sample concentrations. The integration boundaries for the absorption was set to 655nm and 665 nm, based on the excitation at 660 nm and a full-width-half-maximum of the excitation beam of ~10 nm.

As the NMR and XPS data demonstrates, ethylene glycol is not only solvent but also part of the structure in Ag-MPA(UV) and Ag-MPA(NIR). When we replaced ethylene glycol by 1,3-propanediol, 1,4-butanediol, 1,5-pentanediol, silver thiolate products with similar absorbance and photoluminescence feature can still be obtained. However, the reaction temperature had to be increased from 130 °C to a maximum of 155 °C. The higher temperatures could be necessary due to the lower mobility with increasing molecular weights. With 1,6-hexanediol the reaction did not yield a NIR photoluminescent material any more (see Figure 3.13).

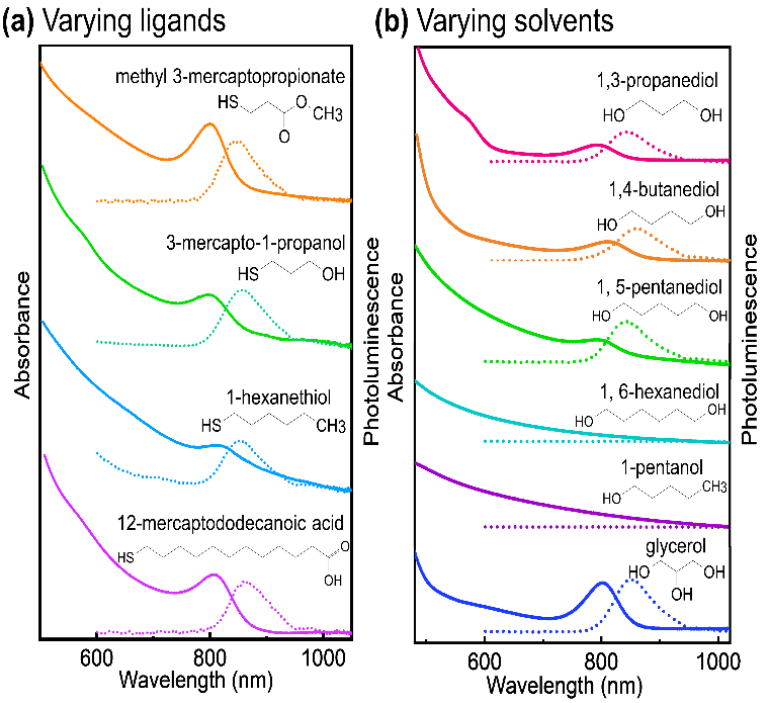

Figure 3.13. Absorption and photoluminescence spectra of (a) silver thiolate synthesized with different thiol ligands in ethylene glycol; (b) Ag-MPA synthesized in different solvents, absorption spectra are plotted with solid lines and photoluminescence spectra with dashed lines.

When we compared solvents with one more (glycerol) or one less hydroxyl group (1-pentanol) than ethylene glycol we found that at least two hydroxyl groups are required to obtain NIR photoluminescent silver thiolates. Thus, an additional hydroxyl group seems not to be problematic for the formation of NIR photoluminescent coordination polymers. This can be related to the number of functional groups needed for "cross-linking" the layers, XRD data shown in Figure 3.14. With two or more OH groups in the solvent molecule, the Ag-MPA layers can be easily inter-connected and stabilized.

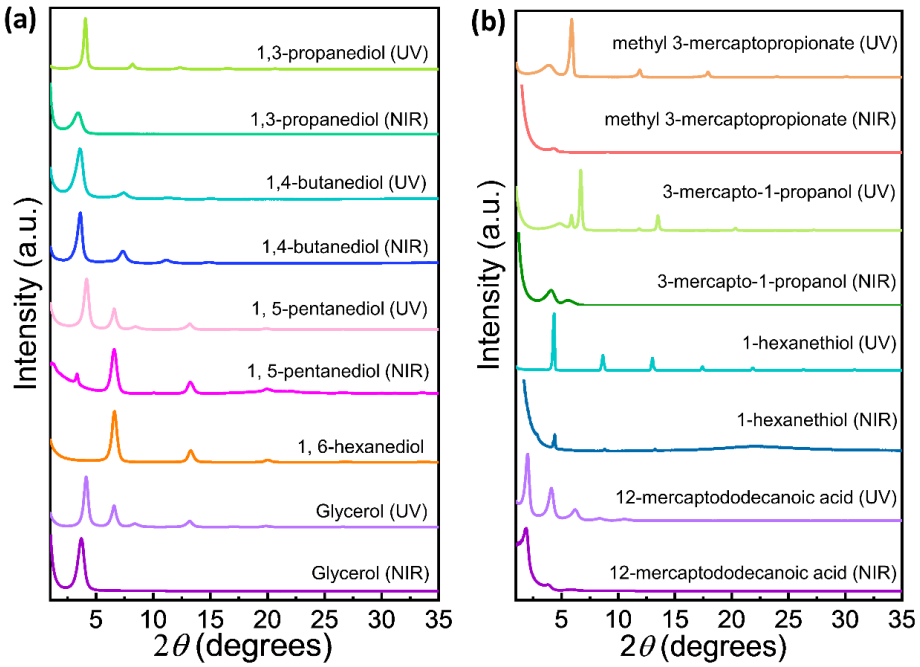

Figure 3.14. PXRD of (a) silver thiolates synthesized with different thiol ligands in ethylene glycol and (b) Ag-MPA synthesized in different solvents.

Since the reaction towards silver thiolate coordination polymers appears to be polymerization-like, we tried to upscale the reaction product by increasing the precursor concentration (see Figure 3.15), without notable differences in the properties of the materials.

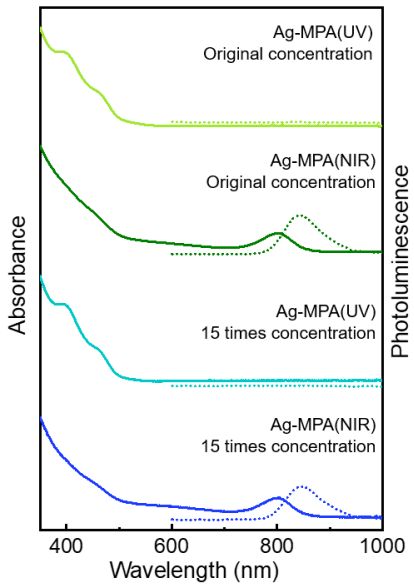

Figure 3.15. Absorption spectra (solid lines) and photoluminescence spectra (dash lines) for Ag-MPA synthesized at different precursor concentrations.

At the same time, we were able to convert aqueous solutions of Ag-MPA(UV) and Ag-MPA(NIR) into 40 nm sized Ag-MPA(NIR) colloids after emulsification in toluene and evaporation of water (see Figure 3.16). The versatile processing of Ag-MPA will allow for versatile integration in various applications ranging from bio-imaging to optoelectronics.

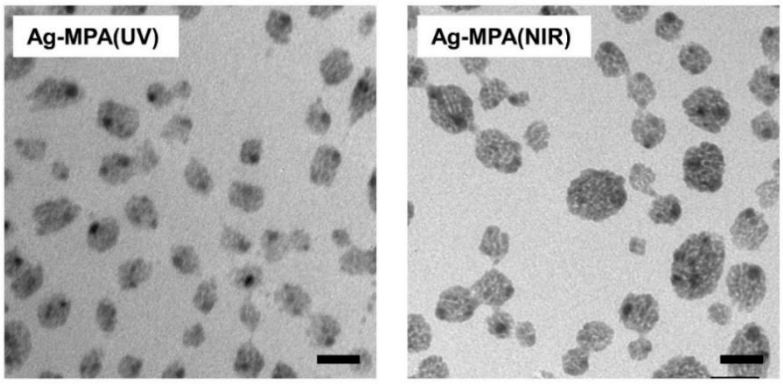

Figure 3.16. TEM images of Ag-MPA(UV) and Ag-MPA(NIR) toluene emulsion. Scar bars are 50 nm.

3.4 Conclusion

In conclusion, we have analyzed the reaction process of $AgNO_3$ and thiolate ligands in ethylene glycol and other hydroxylated solvents during heating. We found that thiol-bearing molecules act as a ligand for silver in the formation of lamellar silver thiolate coordination polymers. Their end group and overall length of the ligand were not limiting the reaction towards NIR photoluminescent silver thiolates. We further found that ethylene glycol is not only the solvent but intercalates in the silver thiolate layers at later stages in the synthesis. Similar materials were obtained with solvents that bear at least two hydroxyl groups (diols and glycerol) and are not too high molecular weight (such as 1,6-hexanediol compared to ethylene glycol). I discovered that the obtained silver thiolate coordination polymers display a reversible blue-to-NIR optical transition, which are linked to structural transformations as evidenced by PXRD, solid state NMR and DSC. Furthermore, the XPS data supports the solid-state NMR results that the chemical state in Ag-MPA(UV) and Ag-MPA(NIR) are very similar.-Thus we conclude that the (temperature-dependent) optical properties of Ag-MPA coordination polymers are modulated by metallophilic interactions between silver atoms in the layered silver thiolates and stabilized in the reversible range by conformational changes of the ligands. The nearly identical absorption feature at 800 nm and the reversibility (under suitable conditions) suggest that syntheses working with $AgNO_3$ and MPA in ethylene glycol yield NIR photoluminescent coordination polymers rather than the Ag_2S nanocrystals that several works of literature linked to the very characteristic optical properties. Therefore, our findings resolve this issue due to the now clarified chemical identity of the NIR photoluminescent material, which opens new avenues for applications. Since the Ag-MPA material forms and can be processed like a polymer material, new possibilities arise for applications ranging from bio-imaging to optoelectronics.

4. Silver thiolate supramolecular gel with near infrared emission and enhanced mechanical properties

Chapter 4 is based on a manuscript under preparation for publication.

My contributions to the project are the synthesis of Ag-MPA coordination polymers, the purification of the samples, the measurement of optical spectra, the characterization by TEM and AFM and the data analysis and interpretation. The PXRD were measured by Christoph Sieber, SEM images were recorded by Gunnar Glasser. Robert Graf measured, analyzed and interpreted the NMR data. Rheology measurements and tensile strength data were collected by Andreas Hanewald.

4.1 Introduction

Supramolecular gels are soft matter materials generated from low molecular weight compounds (M_w<3000 g/mol) and solvents. Small gelator molecules self-aggregate and entangle to form self-assembled fibrillary networks held together by non-covalent interactions, such as hydrogen bonding, π-π stacking, electrostatic interactions, van der Waals forces, and hydrophobic interaction,[180,181] which can be triggered by external stimuli to achieve the gel-sol transition. Among the fields of supramolecular gels, metallogels of coinage metals attract tremendous attention due to unique redox, optical, and electronic properties from the functionalized metal complexes.[182-184]

The Ag(I) ion displays a versatile coordination number (2-6) and diverse coordination geometries, such as linear, trigonal, tetrahedral, square, and octahedral.[185-189] Since Ag(I) is a soft Lewis acid, it exhibits the tendency to strongly coordinate with the soft Lewis base sulfur.[69] These two points offer ample possibilities to build Ag(I)-sulfur supramolecular gels with desirable properties.[55] For instance, Shen et al. reported on an anion-responsive Ag(I)-glutathione coordination polymer hydrogel, where the addition of iodine can trigger the gel-sol state transition, and subsequent addition of Ag(I) leads to a reversible sol-gel transition.[114] Chen et al. prepared injectable, self-healing, antimicrobial, degradable, and superabsorbent hydrogels through Ag coordinated to 4-arm PEG-SH and applied this gel for microRNAs delivery.[190]

These hydrogel systems make use of the general property of silver(I) coordination compounds, such as stronger complexation ability with iodine and antibacterial properties.[191] However, no silver (I) supramolecular gel related to the unique optical property of silver-sulfur complex, near-infrared (NIR) (700-2000 nm) fluorescence property which typically exhibits from Ag_2S quantum dots, was reported. NIR light can penetrate deep into tissue with lower absorption and scattering compared to Vis light.[192] Therefore, NIR fluorescence materials are widely used for imaging in vivo, photoacoustic imaging, photodynamic therapy, and related biomedical fields.[193]

As reported in the previous chapter, we successfully synthesized silver thiolate coordination polymer with switchable blue to NIR optical transitions. we noticed *in situ* gelation of Ag-MPA in EG when carrying out the reaction with fifteen times higher precursor concentration. In this chapter, we further modified the structure of the silver thiolate coordination polymer and designed a silver thiolate supramolecular gel with a short thiol ligand, NIR fluorescence, and good water solubility. Furthermore, we blended it with poly(vinyl alcohol) (PVA) to obtain a robust, free-standing, and stretchable hydrogel. Its excellent compatibility with PVA aqueous solution expands the potential of these materials in biomedical and sensory applications.[194]

4.2 Experimental part

Chemicals: All reagents were purchased and used without further purification. Silver nitrate (Sigma-Aldrich, BioXtra, >99%), 3-mercaptopropionic acid (Aldrich, ≥99%), ethylene glycol (Acros organics, 99.5%, for analysis), diethylene glycol (Sigma Aldrich, ≥99.0%), poly(vinyl alcohol) (Aldrich, *M*w 89,000-98,000, 99+% hydrolyzed), citric acid trisodium salt (Acros organics, 98% anhydrous), acetone (Fisher Chemical, >=99.8%).

Methods:

Synthesis of Ag-MPA-EG/DEG (NIR): 0.645 g of $AgNO_3$ (3.75 mmol), 25 mL of ethylene glycol and 25 mL of diethylene glycol were added into a 100 mL 3-neck-flask. The mixture was degassed under vacuum at room temperature for 30 min. After stopping the vacuum and putting the flask to argon, 0.7 mL of 3-mercaptopropionic acid (7.5 mmol) was injected into the flask and the temperature was set to 125 °C. When the temperature of the solution reached 125 °C, the cloudy white solution changed to clear orange gradually (~5 min-10 min) and finally changed to dark brown (~15 min). Afterward, the mixture was cooled to room temperature using a water bath.

Purification of Ag-MPA-EG/DEG (NIR): 30 mL of acetone was added to 5 mL of the reaction solution. After shaking the centrifuge tube, a fiber-like structure flocculated from the solvent. The mixture was centrifuged for 5 min at 7000 rpm, the clear supernatant was discarded and the precipitated was washed by acetone at least two more times. Then the precipitate was dried by freeze drying (CHRIST, Alpha 2-4 LSCbasic) at -80 °C for 8 h.

Preparation of PVA based Ag-MPA-EG/DEG (NIR) hydrogel: Firstly, aqueous solutions of 8 wt% PVA with varying Ag-MPA-EG/DEG content. Specifically, the 8 wt% PVA aqueous solution was mixed with Ag-MPA-EG/DEG to achieve Ag-MPA-EG/DEG content of 0 wt%, 0.13 wt% (the weight ratio of Ag-MPA-EG/DEG : PVA = 0.016), and 0.4 wt% (the weight ratio of Ag-MPA-EG/DEG : PVA = 0.05). These solutions were poured into a polycarbonate container with a metal bottom for good thermal conductivity. The size of the cavity was 2 mm in thickness, 6.5 mm in height and 5.5 mm wide (the photographs of the container are shown in Figure 4.1). The filled container was slowly immersed into the -78 °C cooling bath (a mixture of ethanol and dry ice) from the bottom to the top for 1 h. Afterward, the frozen ice sample was

taken out of the cooling bath. The formed gel was removed from the container and immediately immersed and stored in 1.5 M trisodium citrate aqueous solution at 4 °C for 48 h.

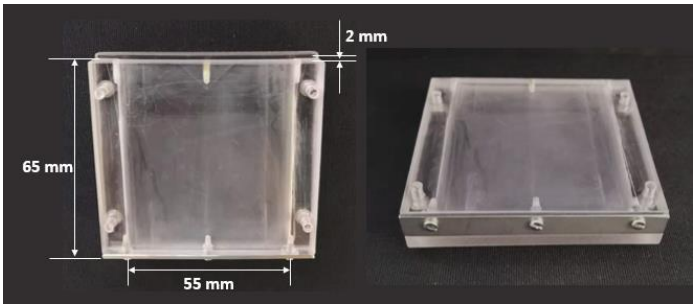

Figure 4.1. Photograph of the container to prepare PVA-based hydrogels.

Characterization:

Absorption measurements. 1 cm pathlength quartz cuvettes with a chamber volume of 3 mL were used for absorption measurements. The absorption spectra were conducted on an Agilent Cary 60 Spectrophotometer.

Photoluminescence measurements. Photoluminescence spectra were recorded using J&M TIDAS diode-array spectrometer with an XBO-lamp as the excitation source.

Atomic force microscopy. AFM samples were prepared by drop-casting the aqueous solution onto the silicon wafer. AFM imaging was performed on a Dimension Icon FS AFM in tapping mode with a scan rate of 0.595 Hz.

Scanning electron microscopy. SEM imaging was performed on a Zeiss LEO Gemini 1530 Scanning Electron Microscope (Zeiss) with an acceleration voltage of 3 kV.

X-ray diffraction. Powder XRD patterns were collected on a Rigaku SmartLab Diffractometer, operated with a Cu Kα radiation source (1.540593Å) with increment steps of 0.01° and at 0.3°/min.

Rheological experiments. Rheological characterization was carried out on Modular Compact Rheometer (Anton Paar) with a parallel plate (diameter: 25 mm) at room temperature. The storage modulus (*G*') and loss modulus (*G*'') were monitored under small-amplitude shear at an applied frequency of 10 rad/s.

Tensile strength testing. The mechanical tensile strength of the PVA-based hydrogels was determined using a Universal Testing Machine (Zwick/Roell Z2005). The PVA-based hydrogel film was cut to a 10 mm wide rectangle. The samples were stretched until they broke at a rate of 50 mm/min. The stress (σ) was obtained by dividing the loaded force (F) by the cross-sectional area (A_0) and the strain (ε) was obtained by dividing the deformed length (Δl) by the original length (l_0) ((l_0) is 20 mm in this testing).

$$\sigma = \frac{F}{A_0} \qquad Equation\ 4.1$$

$$\Delta l = l - l_0, \quad \varepsilon = \frac{\Delta l}{l_0} \qquad Equation\ 4.2$$

Solid state NMR. Solid state NMR measurements have been performed at 700.25 MHz ^{1}H Larmor frequency and 25 kHz magic angle spinning (MAS) frequency with a Bruker Avance III console using a commercial double resonance probe supporting zirconia rotors with 2.5 mm outer diameter. The radio frequency power for signal excitation and decoupling has been adjusted on both frequency channels, ^{1}H and ^{13}C, to a nutation frequency of 100 kHz corresponding to a duration of 90° excitation pulses of 2.5 µs.

4.3 Results and discussion

4.3.1 The gelation of Ag-MPA

Based on the work in chapter 3, we noticed that when using more than ten times the typical precursor concentration, both Ag-MPA(UV) and Ag-MPA(NIR) formed gels in EG, which can stay firmly on the top of an inverted bottle. Moreover, we noticed that after the samples were heated to ~80 °C, the gel collapsed to form a solution, but upon cooling the sol state sample to room temperature for around 10 min, the gel state was restored. Interestingly, this gel can also be reversibly converted into a solution by other external stimuli, such as shaking and stirring. Letting the solution stand led again to a gel. Therefore, the gel-sol transition can be triggered/recovered by heating/cooling and shaking/resting (see Figure 4.2).

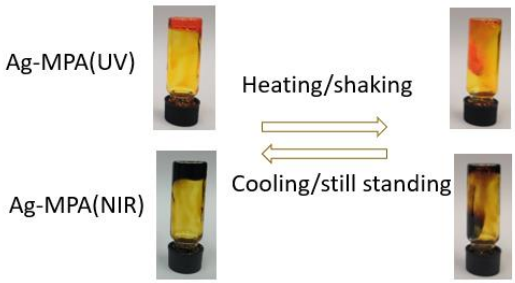

Figure 4.2. Photographs of the gel-sol transition of Ag-MPA(UV) and Ag-MPA(NIR).

Dynamic mechanical analysis can be used to analyze both elastic and viscous material responses simultaneously. A motor is used to apply a sinusoidal strain to a material, and the resulting stress is measured with a force measuring transducer. The force is then electronically separated into two components – and elastic stress and viscous stress. The elastic stress of the material is the component of the measured stress that is in phase with the applied strain, and the viscous stress is the component of the stress that is in phase with the strain rate or 90° out of phase with the strain. If the test is done in a sheer geometry, then shear moduli (*g*) are calculated. The elastic modulus (*G*') is defined as the ratio of the elastic stress to strain and relates to the material's ability to store energy elastically. The loss modulus (*G*") is the ratio of the viscous component to the strain, and relates to the material's ability to dissipate stress through viscous flow. The moduli (*G*"/*G*') ratio is defined as tan δ, which indicates the relative degree of viscous-to-elastic dissipation of the materials. The rheological analysis of Ag-MPA(UV) was shown in Figure 4.3a.

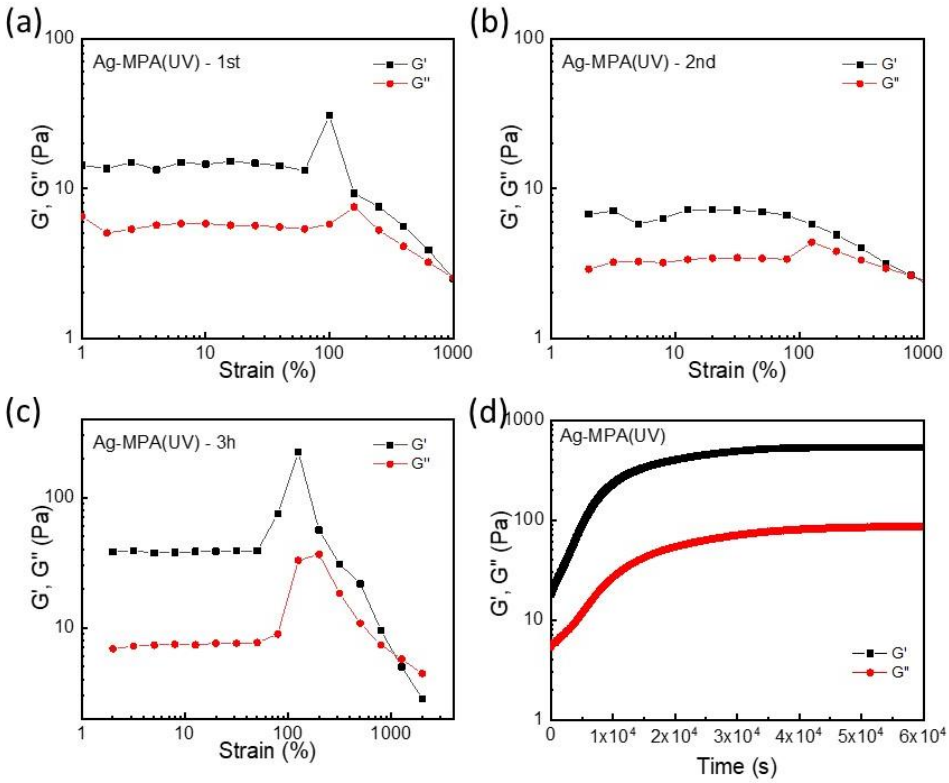

Figure 4.3. Rheology behaviour of Ag-MPA(UV) in strain sweep experiments from 1% to 1000%, (a) the 1st measurement from gel to sol, (b) the 2nd measurement performed after 30 s resting time after the 1st measurement, (c) a 3rd measurement was performed 3 h after the 1st measurement. (d) Time sweeps from 0 s to 6000 s with a constant strain of 0.1% (recover from 1000% strain).

In the linear viscoelastic zone (the strain less than ~180%), *G' > G"*, the sample responded elastically to the imposed strain. With the increase of the strain, *G'* and *G"* lost the linear property and eventually intersected at ~200% (flow point). When the strain was increased beyond the flow point, the gel broke down to form a solution with the typical viscous properties of a fluid. The strain was further increased until 1000%, then after 30 s resting, the second testing interval started (see Figure 4.3b). Clearly, Ag-MPA(UV) supramolecular gel exhibited similar viscoelastic properties in both testing runs for strains less than ~180%. Here *G' > G"* and the flow point was always at ~200% strain. However, the *G'* value decreased from 11 Pa to 7 Pa in the second testing cycle. Thus, Ag-MPA(UV) showed a fast yet uncompleted recovery of the gel state after breaking down by two much-applied strains. When testing again 3 h, a slight increase of the *G'* (13 Pa) was noticeable (see Figure 4.3c), most likely because some unordered EG molecules became aligned during the shear force operation. The temporal evolution of *G*' and *G*" was shown in Figure 4.3 d to exhibit the change of *G*' and *G*" during

the recovery progress, which determined by the recombination of hydrogen bonds. This time-dependent shear thinning property is called thixotropy, which is a common property of supramolecular gels due to the flexibility of the non-covalent bonds.

Importantly, Ag-MPA(NIR) supramolecular gels exhibited similar rheology and thixotropy properties as Ag-MPA(UV) (see Figure 4.4). This offered the possibility to design NIR fluorescent soft materials, which might be potentially interesting for some applications.

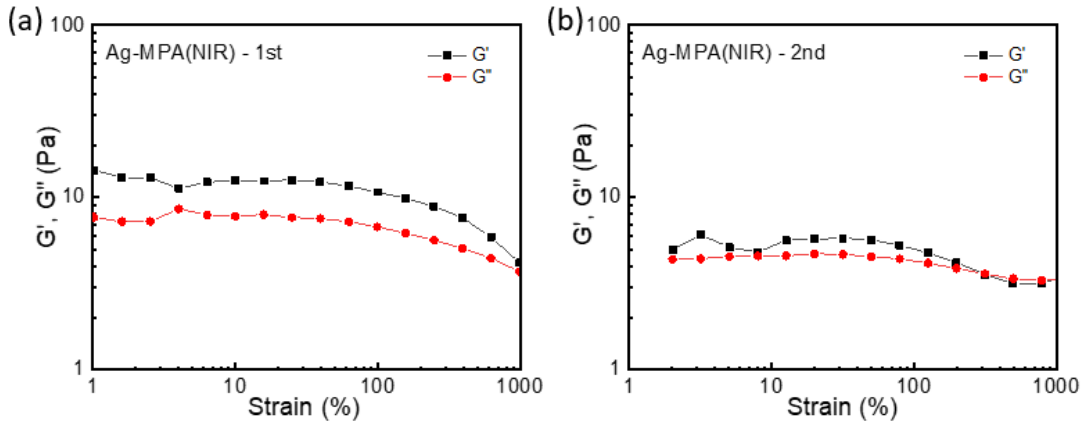

Figure 4.4. Rheological behaviour of Ag-MPA (NIR) in strain sweep experiments from 1% to 1000%, (a) the 1st measurement form gel to sol, (b) the 2nd measurement performed 10 s after the 1st measurement.

4.3.2 Tuning the properties by introducing diethylene glycol (DEG)

The introduction of a suitable co-solvent can be used to further tune the properties of Ag-MPA coordination polymer. This is because, like EG, the solvent can interact with the lamellar layers through hydrogen bonding, therefore potentially influencing the final properties. In this section, the modified the silver thiolate coordination polymer Ag-MPA by introducing diethylene glycol (DEG) as a co-solvent in the synthesis (we name the product Ag-MPA-EG/DEG from here on) was studied. An increase in the quantum yield as well as the mechanical properties was achieved.

4.3.2.1 Synthesis and reaction process

Firstly, EG and DEG are mixed homogenously before the addition of $AgNO_3$. After water and oxygen was removed by degassing, MPA was added to the reaction flask under argon atmosphere, and the reaction medium was slowly heated to 125 °C. When the temperature of the solution reached 125 °C, the turbid white mixture turned into a clear orange solution gradually (~5 min - 10 min) and eventually changed to a dark brown solution (~15min). Afterwards, the mixture was cooled to room temperature using a water bath. We monitored the products of this reaction. The first stage milk-white sample was obtained at 75 °C (Ag-MPA-EG/DEG (I)). After heated at 125 °C for 5 min, the second stage orange sample was obtained (Ag-MPA-EG/DEG (II)). Then, after heated at 125 °C for 15 min, the final stage dark brown sample was obtained (Ag-MPA-EG/DEG (NIR)).

The products were taken out of the flask and kept at room temperature for a week before purification and freezing-drying. After a week of aging, acetone was added to the sample with stirring to obtain a fiber-like precipitate. This precipitate was separated from the solvent by centrifuge. Then this process was repeated two more times to purify the sample from EG and DEG. After freeze-drying overnight, the obtained powder was characterized by solid state NMR and PXRD measurements (see Figure 4.5, 4.7).

^{1}H MAS NMR spectra of Ag-MPA-EG/DEG(II) and Ag-MPA-EG/DEG(NIR) showed distinct signals assigned to OH and O-CH_2 groups from EG and DEG at around 3.5 - 5 ppm (see Figure 4.5 c, d). The peak at 12.5 ppm in the spectra of Ag-MPA-EG/DEG(I) was assigned to acid dimer from the –COOH of MPA (see Figure 4.5 a). This signal from the acid dimer did not appear in the spectra of Ag-MPA-EG/DEG(II) and Ag-MPA-EG/DEG(NIR), indicating the hydrogen bond dissociated gradually while heating. The strong and sharp peak of Ag-MPA-EG/DEG(I) (~5 ppm) possibly came from water, which could be absorbed by the uncoordinated carboxyl groups.

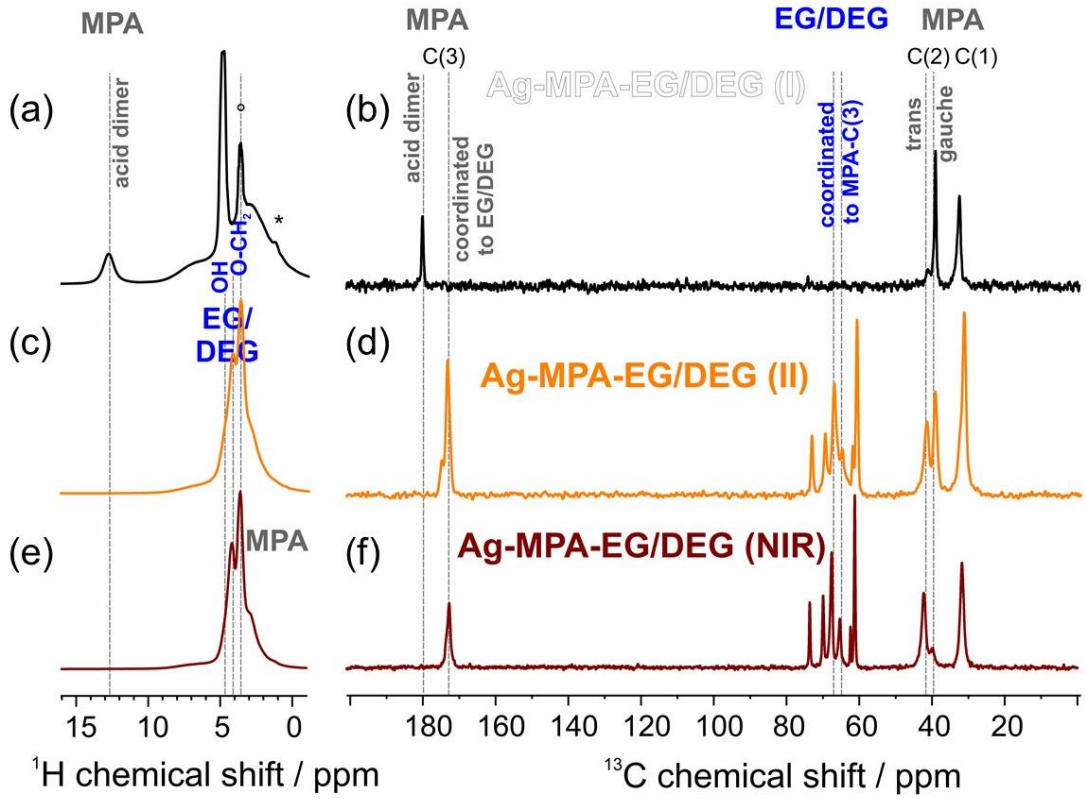

Figure 4.5 (a) ^{1}H MAS NMR spectra, and (b) ^{13}C NMR spectra of Ag-MPA-EG/DEG (I); (c) ^{1}H MAS NMR spectra, and (d) ^{13}C NMR spectra of Ag-MPA-EG/DEG (II); (e) ^{1}H MAS NMR spectra, and (f) ^{13}C NMR spectra of Ag-MPA-EG/DEG (NIR).

In the ^{13}C NMR spectra, the peak at ~172 ppm was assigned to acid sites coordinated to OH in EG and DEG (see Figure 4.5 d, f). The peak at ~29 ppm was assigned to MPA carbon sites C(1) S-CH_2. The MPA carbon sites C(2) at ~42 ppm split into two peaks responding to *trans* and *gauche* confirmations. As in the case of Ag-MPA(II), the ratio of *gauche : trans* of Ag-MPA-EG/DEG (II) was almost identical. Furthermore, regarding Ag-MPA-EG/DEG (NIR), most of the MPA was transferred to *trans* conformation. There was a group of signals stemming from O-CH_2 in the range of 58 – 75 ppm. For both Ag-MPA-EG/DEG (II) and Ag-MPA-EG/DEG (NIR), the peak at 67 ppm was assigned to O-CH_2 from EG coordinated to the carboxyl group of MPA, and the peak at 60.5 ppm was assigned to O-CH_2 from EG with uncoordinated free OH. The peak at 65 ppm was assigned to O-CH_2 from DEG coordinated to the carboxyl group of MPA, and the peak at 61.5 ppm was assigned to O-CH_2 from DEG with uncoordinated free OH. The peaks at 69 ppm and 73 ppm were possibly corresponding to CH_2-O-CH_2 in DEG. Naturally, it is difficult to distinguish these two signals.

The one-week aged sample was compared with the fresh purified sample immediately after synthesis. The sample purified immediately after synthesis exhibited weak coordination signals of EG and DEG in ^{1}H MAS and ^{13}C MAS NMR spectra (see Figure 4.6). Aging time is necessary for the formation of the hydrogen bonds, which might facilitate the formation of a higher-order assembled structure.

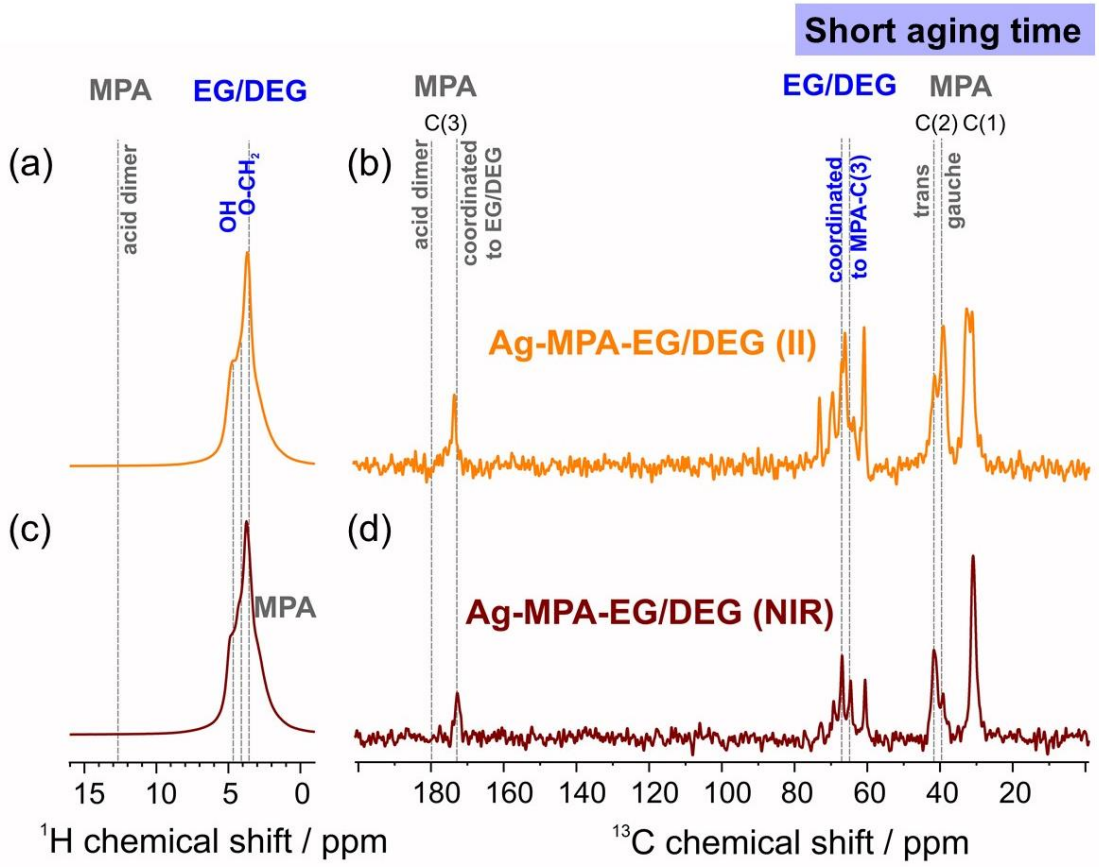

Figure 4.6. (a) ^{1}H MAS NMR spectra, and (b) ^{13}C NMR spectra of Ag-MPA-EG/DEG (II) with short aging time; (c) ^{1}H MAS NMR spectra, and (d) ^{13}C NMR spectra of Ag-MPA-EG/DEG (NIR) with short aging time.

The PXRD results agreed well with the results of NMR. The PXRD pattern of Ag-MPA-EG/DEG(I) showed a well-ordered lamellar structure. The pattern of Ag-MPA-EG/DEG(II) also showed a lamellar structure, but the opening of acid dimer resulting in an increased inter layer distance and the replacement of DEG with EG decreased the order between layers. Besides, the intensity of the pattern (020) and (030) decreased compared with Ag-MPA(UV)

(see Figure 4.7). With most parts of MPA arranged as *trans* confirmation, the distance further increased and order decreased, and only the signal of (010) was shown in the spectra.

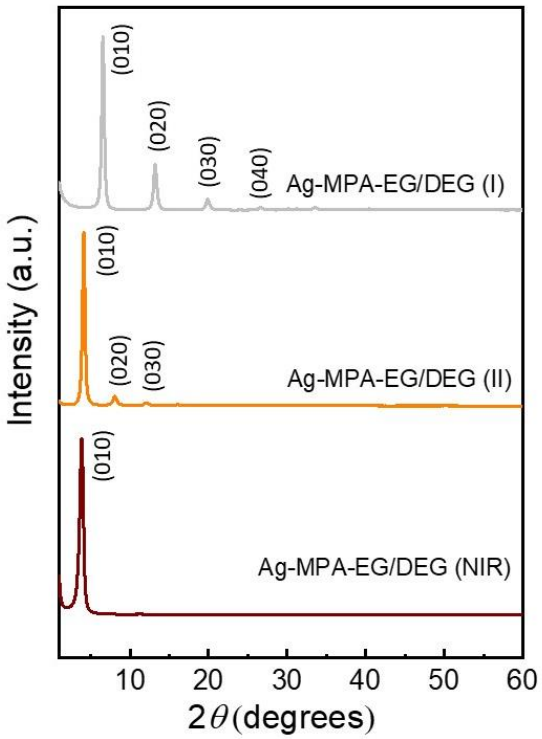

Figure 4.7. PXRD patterns of Ag-MPA-EG/DEG.

According to these results, the scheme of Ag-MPA-EG/DEG (NIR) was illustrated in Figure 4.8. Ag and S construct a plane with a distorted hexagonal, and the thiol ligands MPA distribute on both sides of the Ag-S plane. The terminal carboxyl group of MPA partially coordinated with EG and partially coordinated with DEG through hydrogen bonding. We noticed that with the introduction of DEG, Ag-MPA-EG/DEG possessed better solubility in water than Ag-MPA. Due to the introduction of DEG, the space between layers could be expanded to hold more water molecules.

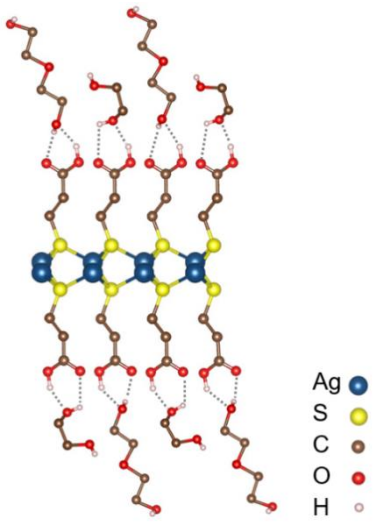

Figure 4.8. The scheme of Ag-MPA-EG/DEG(NIR).

Between two layers of Ag-MPA-EG/DEG, the solvent can be hosted and stabilized by hydrogen bonding and self-assemble into filament-like structures. With a larger number of filaments self-assembly, intersecting fibers could form, as shown in AFM images in Figure 4.9. The entanglement of nanofibers made the formation of a solid-like network possible.

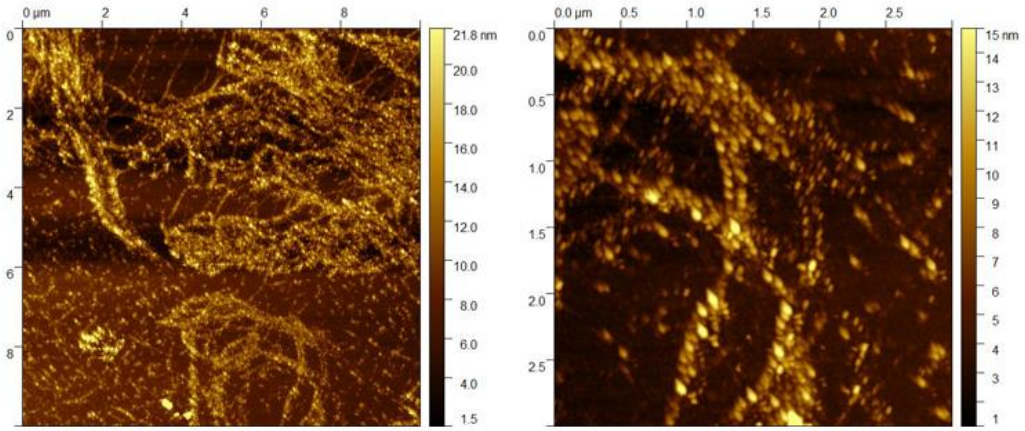

Figure 4.9. AFM images of Ag-MPA-EG/DEG(NIR).

4.3.2.2 Optic and rheological properties

After the introduction of DEG, Ag-MPA-EG/DEG (II) and Ag-MPA-EG/DEG (NIR) exhibited similar rheology properties, as well as thermoreversible and thixotropic properties. In an inverted glass vial, the gel can stay on the top of the bottle against gravity. Once heated up

to around 70 °C, the materials turned sol state. Cooling back to room temperature led back to gelation.

Additional experiments focused on exploring the rheological properties of Ag-MPA-EG/DEG (NIR) were conducted. Due to the absence of luminescence properties, the Ag-MPA-EG/DEG (II) was not researched any further. A motor with parallel plates was used to apply a sinusoidal strain to the material, and the resulting stress was measured by a force measuring transducer. Detailed experiment procedure was shown in section 4.3.1. In the first cycle of a multi-cycle strain-sweep measurement, when the strain was less than 60%, the elastic modulus (*G*') was higher than the loss modulus *G*" (see Figure 4.10 a). Thus, Ag-MPA-EG/DEG(NIR) supramolecular gels exhibit typical gel behavior. With the increase of strain, *G'* and *G"* loose the linear feature and the curves crossed at a strain at around 67%, known as the flow point. Beyond the flow point where $G' < G''$, the sample turned to its sol state. The second and third cycles of measurements were carried out after 20 min intervals to recover the gel state with similar rheological properties as observed in the first cycle. This result exhibited the dynamic and reversible nature of the Ag-MPA-EG/DEG(NIR) supramolecular gel, which is controlled by the breaking and recombination of hydrogen bonds. Both *G'* (increased from 17 Pa for the 1st measurement to 20 Pa for the 3rd measurement) and *G"* (increased from 15 Pa for the 1st measurement to 16 Pa for the 3rd measurement) increased since more unordered EG and DEG molecules became ordered under the shear force operation. Ag-MPA-EG/DEG(NIR) exhibited higher *G'* and *G"* than Ag-MPA, possibly attributed to the higher inter-molecule interactions of DEG (i.e., hydrogel bonding), indicated by the higher melting point and boiling point compared to the EG.

In order to further evaluate the recovery process of Ag-MPA-EG/DEG (NIR), a series of sweep experiments were conducted to monitor the recovery process from 1000% to 0.1% strain. The measurement was started at the point that strain changed from 1000% to 0.1%. Figure 4.10 b showed that the sample transformed from sol to gel immediately, then *G'* and *G"* increased gradually under the low strain 0.1%. These results showed the typical thixotropy of Ag-MPA-EG/DEG(NIR). The dynamic and reversible nature of the non-covalent interactions (e.g., hydrogen bonds), contributing to the formation of these network structures, gives these supramolecular gels the inherent ability to respond to external stimuli.[195]

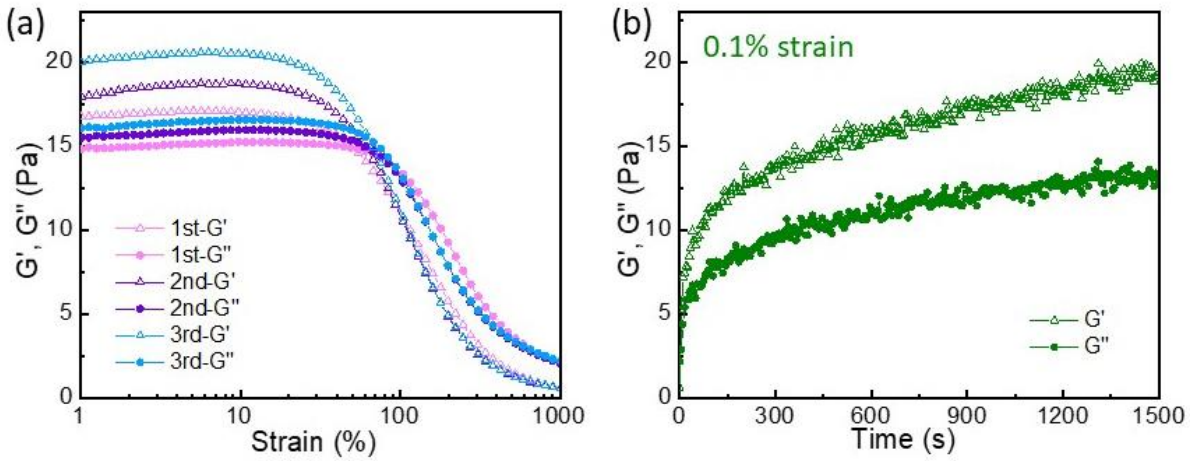

Figure 4.10. Rheology behavior of Ag-MPA-EG/DEG(NIR): (a) in strain sweep experiment from 1% to 1000%, (b) time sweep from 0 s to 1500 s with constant strain 0.1% (recover from 1000% strain).

The same as the previous sample Ag-MPA(NIR), Ag-MPA-EG/DEG (NIR) exhibited an absorbance peak at ~800 nm with corresponding photoluminescence at ~840 nm (see Figure 4.11), and the quantum yield increased from 5.4% for Ag-MPA(NIR) to 12.9% for Ag-MPA-EG/DEG (NIR). A possible reason could be that the relatively high rigidity of the DEG system could suppress the non-irradiation decay through the thermal relaxation pathway.[196]

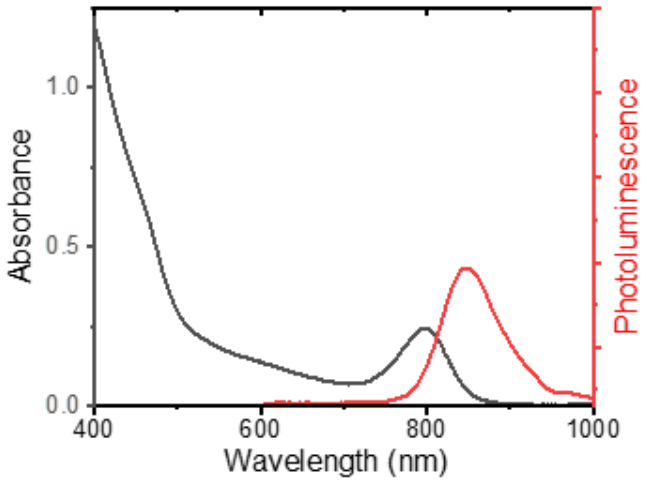

Figure 4.11. The absorption (black line) and photoluminescence (red line) spectra of Ag-MPA-EG/DEG.

4.3.2.3 Xerogels

Furthermore, the ice templating and freeze-drying methods were used to prepare xerogels with different concentrations of aqueous Ag-MPA-EG/DEG solutions in a 1 ml cubic mold. After freeze-drying, the solid xerogel can almost maintain the volume of the mold and exhibits a sponge-like structure with 1.6 wt% aqueous Ag-MPA-EG/DEG solutions (see Figure 4.12 b, c). The density was determined to be around 0.02 g/cm^3. When the concentration decreased from 1.6 wt% to 0.2 wt%, the volume shrank but still maintained the sponge-like structure (see Figure 4.12 a). A 0.1 wt% sample maintained almost ¼ of its original volume. When decreasing the concentration further, the volume of the xerogel monolith became smaller and eventually collapsed completely (see Figure 4.12 a,g).

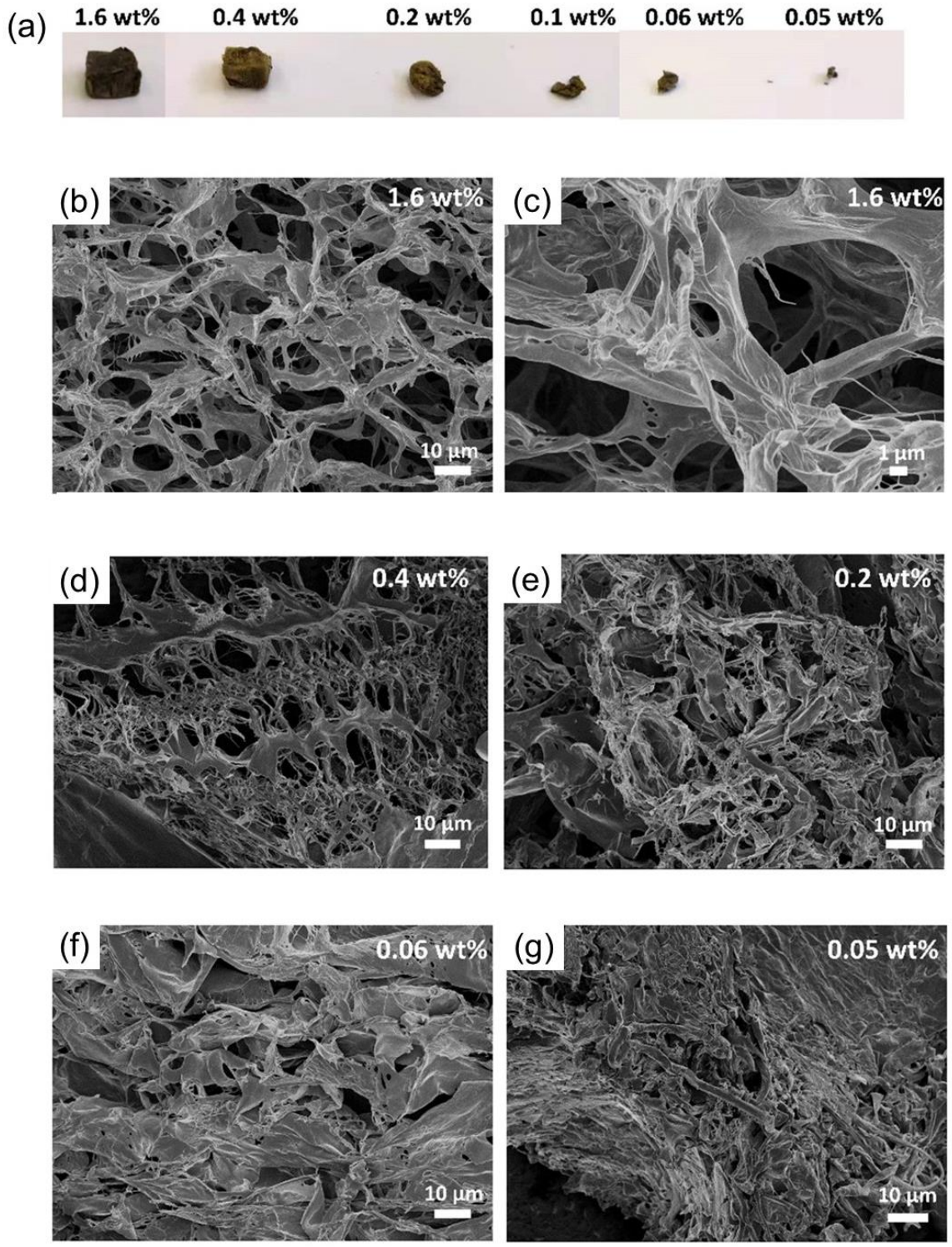

Figure 4.12. (a) Photographs and (b) SEM micrographs of Ag-MPA-EG/DEG(NIR) xerogels obtained by freeze-drying aqueous solutions of Ag-MPA-EG/DEG(NIR) at different concentrations.

4.3.3 PVA-based hydrogels

Limited by the non-covalent interactions nature of the supramolecular gel, Ag-MPA-EG/DEG(NIR) cannot exhibit available mechanical properties, such as stretchable and compressible. In order to extend the application of this NIR fluorescence supramolecular gel, it was blended with PVA to enhance the mechanical properties. PVA is a widely used, biocompatible, and low cell adhesion hydrogel, typically crosslinked by microcrystalline domains and hydrogen bonds. Firstly, we prepared 8 wt% PVA hydrogel. Then we blended different amounts of Ag-MPA-EG/DEG (NIR) with 8 wt% PVA based hydrogel, the weight ratios of Ag-MPA-EG/DEG (NIR) : PVA are 0, 0.016, and 0.05 we named as $PVA_{98.4wt\%}[Ag\text{-}MPA\text{-}EG/DEG]_{1.6wt\%}$ and $PVA_{95wt\%}[Ag\text{-}MPA\text{-}EG/DEG]_{5wt\%}$), to prepare toughness NIR emission hydrogel.

We used the freeze-casting and salting-out method to prepare PVA-based hydrogels (details of this method reported by He is shown in section 2.2.2.1).[136] The details of my experiment were shown in methods part of section 4.2. Briefly, an 8 wt% PVA aqueous solution (with the weight ratios of Ag-MPA-EG/DEG (NIR) : PVA are 0, 0.016, and 0.05) was cast in a designed polycarbonate (PC) container with a metal bottom for good thermal conductivity. Then this container was slowly immersed into the -78 °C cooling bath. PVA chains were fixed to a specific shape in the container during the first freezing process, and polymer chains were prepacked microscopically. At the same time, the densification of aligned micropore walls could be expected. During the subsequent thawing in sodium citrate aqueous solution, the preconcentrated PVA chains further aggregated and crystallized to create a mesh-like network (SEM images are shown in Figure 4.13 a,b). These mesh-like networks arranged out the directional backbone according to the freezing direction.

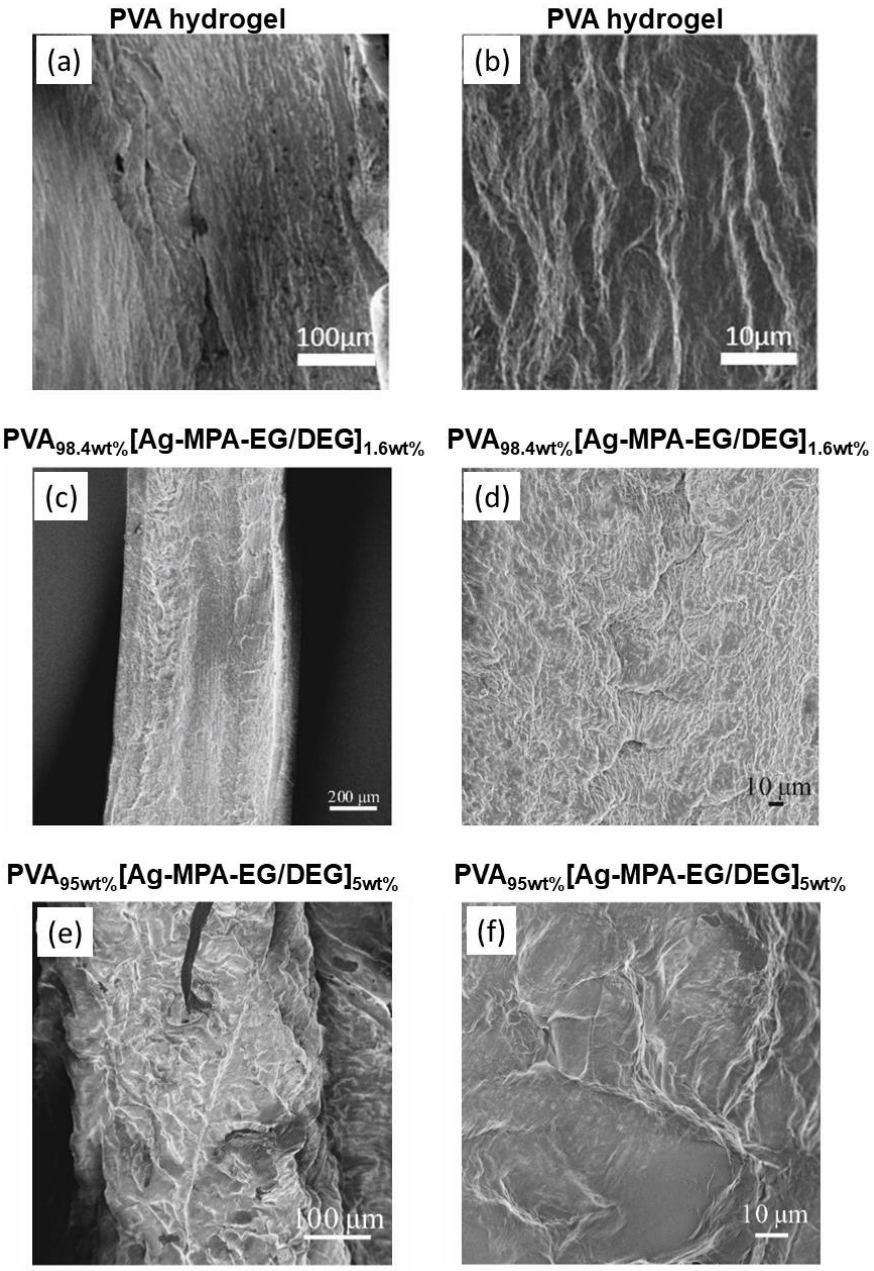

Figure 4.13. SEM images of PVA and PVA-based hydrogel: (a) and (b) PVA hydrogel; (c) and (d) $PVA_{98.4wt\%}[Ag\text{-}MPA\text{-}EG/DEG]_{1.6wt\%}$ hydrogel; (e) and (f) $PVA_{95wt\%}[Ag\text{-}MPA\text{-}EG/DEG]_{5wt\%}$ hydrogel.

The 8 wt% PVA hydrogel demonstrated excellent mechanical properties, with the maximum tensile strain of 730% and ultimate tensile strength of 7.4 MPa (see Figure 4.14), thanks to the densified structure of semicrystalline and aligned PVA fibers. The chain-fracture mechanism can explain the mechanism for dissipating energy in PVA hydrogels.

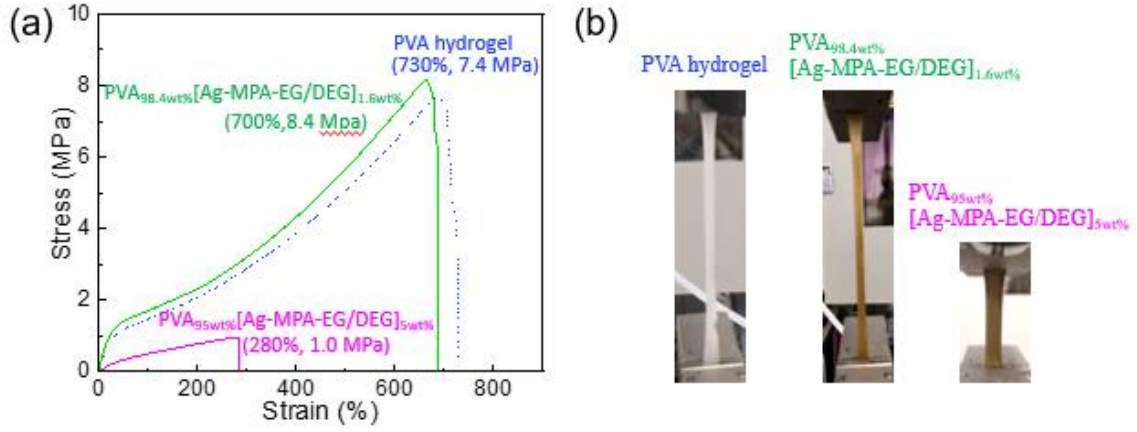

Figure 4.14. (a) Stress-strain curves for PVA hydrogel (blue dashed line), $PVA_{98.4wt\%}[Ag\text{-}MPA\text{-}EG/DEG]_{1.6wt\%}$ hydrogel (solid green line), and $PVA_{95wt\%}[Ag\text{-}MPA\text{-}EG/DEG]_{5wt\%}$ hydrogel (solid purple line), (b) the picture of PVA based hydrogel during the tensile test before fracture.

When the polymer chain is fractured, the mechanical energy stored in the chain is dissipated, the fracture energy in the process zone can be calculated according to the Lake-Thomas theory[197]:

$$\Gamma_D = 2U_f N_f h \qquad Equation\ 4.2$$

U_f: the energy required to rupture a polymer chain;

N_f: the number of polymer chains fractured per unit volume of the process zone;

h: the width of the process zone.

The aligned thicker chains increased U_f, and the nanometer fibers increased N_f. After being stretched, all the folded and entangled nanofibrils were straightened and aligned in the stretched direction to dissipate the fracture energy by breaking the intermolecular interaction (see Figure 4.16 a,b).[198]

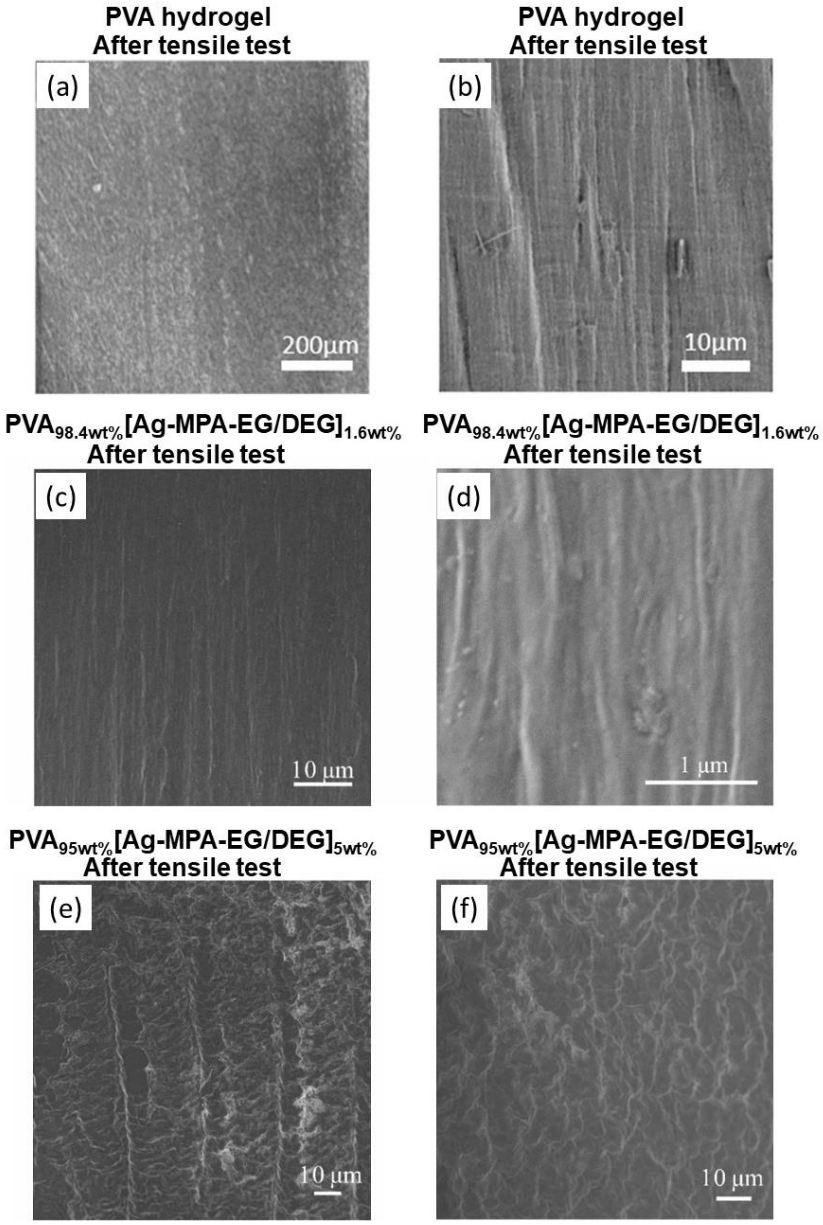

Figure 4.15. SEM images of PVA and PVA-based hydrogel after tensile test: (a) and (b) PVA hydrogel; (c) and (d) $PVA_{98.4wt\%}[Ag\text{-}MPA\text{-}EG/DEG]_{1.6wt\%}$ hydrogel; (e) and (f) $PVA_{95wt\%}[Ag\text{-}MPA\text{-}EG/DEG]_{5wt\%}$ hydrogel.

$PVA_{98.4wt\%}[Ag\text{-}MPA\text{-}EG/DEG]_{1.6wt\%}$ hydrogel demonstrated almost the same mechanical property as a pure PVA hydrogel, with the maximum tensile strain of 700% and ultimate strength of 8.4 MPa (see Figure 4.14). This could be expected because the addition of a small percentage of Ag-MPA-EG/DEG should not interfere too much with the crystallization PVA chains. One could expect that the Ag-MPA-EG/DEG networks simply adheres to the PVA fibers, possibly increasing U_f. Therefore, the tensile toughness slightly increased from 2750

MJ/m^3 of the PVA hydrogel to 2780 MJ/m^3. However, the addition of more supramolecular coordination polymer reduced the mechanical property of the PVA-based hydrogel. $PVA_{95wt\%}[Ag\text{-}MPA\text{-}EG/DEG]_{5wt\%}$ hydrogel exhibited lower ultimate tensile strength (0.95 MPa) and the maximum tensile strain (280%) (see Figure 4.14). The extra addition of supramolecular polymer partially broke the continuously connected network comprising crystallized region and longer polymer fibers. The frack energy cannot distribute to most fibrils, the tensile toughness rescued to 170 MJ/m^3. Therefore, the hydrogel was broken after being stretched, and these fibrils were still curly and loosely on the surface (see Figure 4.15 e,f).

The photoluminescence measurement exhibited that the PVA hydrogel without any luminescence signal, both $PVA_{98.4wt\%}[Ag\text{-}MPA\text{-}EG/DEG]_{1.6wt\%}$ and $PVA_{95wt\%}[Ag\text{-}MPA\text{-}EG/DEG]_{5wt\%}$ hydrogels have a stable NIR emission at ~850 nm before and after the tensile test (see Figure 4.16). The intensity of $PVA_{98.4wt\%}[Ag\text{-}MPA\text{-}EG/DEG]_{1.6wt\%}$ hydrogel decreased after the tensile test because the hydrogel film became narrow and thinner.

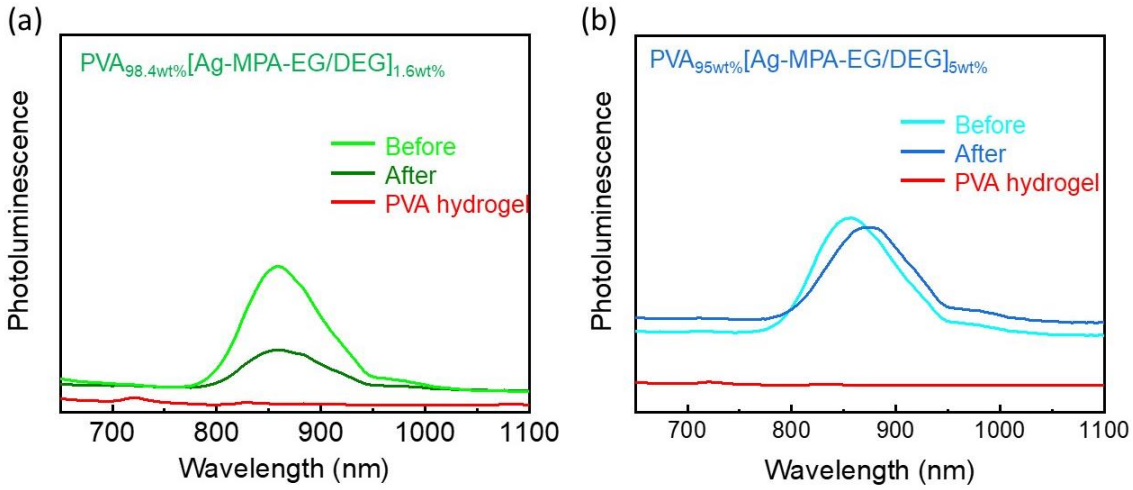

Figure 4.16. Photoluminescence spectra before and after tensile test of (a) $PVA_{98.4wt\%}[Ag\text{-}MPA\text{-}EG/DEG]_{1.6wt\%}$ hydrogel, (b) $PVA_{95wt\%}[Ag\text{-}MPA\text{-}EG/DEG]_{5wt\%}$ hydrogel compared with PVA hydrogel.

4.4 Conclusion

In conclusion, we modified the synthesis method to prepare Ag-MPA-EG/DEG supramolecular gels with an improved NIR emission quantum yield and mechanical properties with thermal reversible and thixotropy, similar to the Ag-MPA samples reported in chapter 3. Moreover, we prepared $PVA_{98.4wt\%}[Ag\text{-}MPA\text{-}EG/DEG]_{1.6wt\%}$ hydrogel, exhibiting excellent tensile strengths and NIR photoluminescence at the same time. Since generally PVA-based hydrogels are bio-compatible, the PVA-Ag-MPA hybrid materials have potential as materials in scaffolds for tissue engineering for biological imaging and sensors in soft machines.[199-200]

5. Silver thiolates as the precursors for Ag_2S thin films and their charge carrier dynamics

Chapter 5 is based on a manuscript under preparation for publication.

My contributions to the project are the synthesis of Ag-MPA coordination polymers, the preparation of Ag_2S films, the characterization of the samples with AFM, and the measurement of the absorption spectra. The THz measurements were done by Shuai Fu. The PXRD measurements were done by Christoph Sieber, SEM measurements were done by Gunnar Glasser, HRTEM was done by Katrin Kirchhoff, and XPS was done by Leon Prädel.

5.1 Introduction

Monoclinic Ag_2S has emerged as a promising class of transition metal chalcogenide (TMC) for optoelectronic and thermoelectric applications, such as sensitized solar cell,[201] photoswitch sensors,[202] IR detectors,[203] and photoelectrochemical cells,[204] thanks to its direct narrow bandgap (0.9 - 1.1eV)[38,37], high optical absorption and remarkable Seebeck coefficient.[32, 205-209] For instance, Jo et al.[210] pioneered the solution-processed synthesis of ductile semiconducting Ag_2S thin films with remarkable stretchability as high as 14.9%, enabling wrinkled Ag_2S-based memory devices with excellent mechanical stretchability and their further integration with motion sensors to form self-powered healthcare monitoring systems. Furthermore, using ductile-metal Ag as buffering layer, Lei et al.[211] demonstrated excellent photoelectric performance retentivity in a Ag_2S/Ag/polyimide heterojuction, where the conductivity remains almost the same after more than 100 cycles of bending tests, allowing robust photodetectors covering a broad spectral range from ultraviolet to near-infrared. Moreover, Feng et al.[212] prepared Ag_2S nanosheets by liquid-phase exfoliation and reported remarkable nonlinearity of 250.4 MW cm^{-2} saturated light intensity and 15.5% modulation depth using a double balance detection system.

Despite recent advances in optoelectronic and thermoelectric devices, facile and scalable synthesis of the thin α-Ag_2S film remains challenging due to the low solubility of Ag_2S in common solvents.[213] Over past decades, several methods have been raised to prepare Ag_2S thin

films such as chemical bath deposition (CBD),[46, 214] epitaxially growth,[215-216] chemical vapor deposition,[217] spray pyrolysis,[218] and electrodeposition.[219]

Chemical bath deposition is the most widely used method for thin Ag_2S film on glass, TiO_2, SnO_2, and oxidized polypropylene, since it was first studied by G. A. Kitaev in 1967.[46, 214, 220] The typical chemical bath deposition method is that the substrate is immersed into $Na_2S_2O_3$ and silver salt solution for the growing of Ag_2S on the surface. The thickness of Ag_2S layer can be partially tuned by the volume of the complexing agent and reaction time.[221,222] Using the same precursor as the spray pyrolysis, chemical bath deposition avoids high temperatures at the substrate and also avoid the high requirement of devices and specific substrate, compared with epitaxial growth, which need high pure silver and sulfur source and NaCl or MgO cleavage surface as substrate.[215-216, 223]

Shen et al.[220] used the CBD method to fabricate SnO_2/Ag_2S sensitized solar cells with a conversion efficiency of 0.41%. Modified from CBD, Lei et al.[224] fabricated poly(3-hexylthiophen-2,5-diyl) (P3HT) : Ag_2S hybrid solar cell with conversion efficiency of 2.04%. They covered elemental silver on the Indium tin oxide (ITO) firstly with 60-80 nm silver grains. Then it was immersed into the sulfur dimethylformamide (DMF) solution. These silver grains transformed into ordered Ag_2S nanosheet arrays with a thickness of 50-60 nm. However, since these Ag_2S nanosheets do not densely stack, it possibly impedes the mobility of the electron-hole pair in the whole film. Chen et al.[225] fabricated phenyl-C61-butyric acid methyl ester (PCBM)/P3HT:Ag_2S solar cell with improved conversion efficiency to 3.21%. They spin-coated the $AgNO_3$ and AgOAc solution on the ITO firstly. Na_2S and thiourea solution was dropped on the substrate afterward. After the excess of solution was removed by water, the Ag_2S covered substrate was heated to 150 °C to improve the crystallinity. The obtained Ag_2S nanoparticles had the size range of 15-70nm and a RMS roughness of 6.8 – 11.2 nm. The possible reasons of the improvement of the conversion efficiency are not only the more appropriate p-type materials, but also the quality of Ag_2S film.

According to the Shockley-Oueisser theory, the maximum efficiency is found to be 30% for an energy gap of 1.1 eV.[226] The reported conversion efficiency of Cu_2S can reach 10.2%,[227] SnS can reach 4.63%,[228] PbS/CdS can reach 5.59%.[229] However, the reported conversion efficiency of Ag_2S is lower (3.21%), and not much research literature is found related to Ag_2S in photovoltaics devices. One of the important reasons is the difficulty in preparing high quality films with good optoelectric properties produced by facile and scalable methods.

Therefore, we aimed to design a method to prepare high quality Ag_2S thin film, which can be applied easily on different substrates for optoelectronic applications. To this end, an aqueous silver thiolate precursor solution was distributed uniformly on a substrate by spin-coating to form a thin film with thicknesses ranging from 30 nm to 200 nm. After thermal treatment of the film, the continuous and highly crystalline Ag_2S film was obtained.

To investigate their charge transport properties, we performed time- and frequency-resolved photoconductivity measurements by ultrafast THz spectroscopy. The results disclosed outstanding mobility of ~150 $cm^2V^{-1}s^{-1}$ and a diffusion length on the order of sub-micrometer in as-synthesized α-Ag_2S thin films. Remarkably, the photoconductivity of α-Ag_2S increased with decreasing temperature, manifesting band-like transport signatures. Notwithstanding the addition of PVA as the rigid component into Ag-MPA inevitably resulted in a decrease in charge transport properties, likely by perturbing the crystallization process of α-Ag_2S and separating the conducting domains. The freestanding α-Ag_2S thin films still exhibited satisfactory mobility of ~ 35 $cm^2V^{-1}s^{-1}$, competitive with the highest values reached by other well-developed TMC thin films.[230]

5.2 Experimental part

Chemicals:

All reagents were purchased and used without further purification. Silver nitrate (Sigma-Aldrich, BioXtra, >99%), 3-mercaptopropionic acid (Aldrich, ≥99%), ethylene glycol (Acros organics, 99.5%, for analysis), diethylene glycol (Sigma Aldrich, ≥99.0%), acetone (Fisher Chemical, >=99.8%), poly(vinyl alcohol) (Aldrich, *M*w 9000 – 10000, 80% hydrolyzed), poly(dimethylsiloxane) (PDMS) (Sylgard 184 silicone elastomer kit).

Methods:

Synthesis of precursor Ag-MPA: 0.645 g of $AgNO_3$ (3.75 mmol), 25 mL of ethylene glycol, and 25 ml diethylene glycol were added to 100 mL 3-neck-flask. After degassing under vacuum, 0.7 mL of 3-mercaptopropionic acid (7.5 mmol) was injected into the flask under argon atmosphere, and the temperature was raised to 125 °C. The reaction proceeds for 10 min at 125 °C. Afterward, the mixture was cooled to room temperature to obtain orange precursor Ag-MPA (we named it as Ag-MPA-EG/DEG(II) in chapter 4. Here, we named it Ag-MPA for the sake of brevity).

Purification and preparation of Ag-MPA aqueous solution: 30 mL of methyl acetate was added to 5 mL of the reaction solution. After shaking, the mixture was centrifuged for 5 min at 7000 rpm, the clear supernatant was discarded, and the orange precipitate was washed by acetone two more times. Then 5 mL of water was added to the precipitate to obtain the aqueous Ag-MPA solution.

Preparation of thin Ag_2S film: An aqueous Ag-MPA solution was drop-cast on the substrate and spun at 1300 rpm for 30 s to obtain an Ag-MPA film. Afterward, the Ag-MPA film on the substrate was heated to 180 °C for 10 min to obtain an Ag_2S film.

Preparation of PVA-based Ag_2S film: 0.55 g poly(vinyl alcohol) (PVA) were dissolved in 5 mL water to prepare 10 wt% PVA aqueous solution. Then 5 mL prepared Ag-MPA aqueous solution was mixed with 5 mL 10% PVA aqueous solution to obtain Ag-MPA/PVA aqueous solution. The prepared Ag-MPA/PVA aqueous solution was dropped on a PDMS substrate and

dried at 50 °C. Then this film was heated to 180 °C by a hot air dryer to obtain PVA-based Ag_2S film.

PDMS substrate was prepared by casting a PDMS pre-polymer and curing agent (10:1 ratio) into a petri dish, then curing it at 90 °C for 30 min.

Characterization:

High resolution transmission electron microscopy. HRTEM imaging were recorded using a FEI Tecnai F20 transmission electron microscope operated at an acceleration voltage of 200 kV.

X-ray diffraction. Powder XRD patterns were collected on a Rigaku SmartLab Diffractometer, operated with a Cu Kα radiation source (1.540593Å) with increment steps of 0.01° and at 0.3°/min.

Absorption measurements. The absorption spectra were conducted on an Agilent Cary 60 Spectrophotometer.

X-ray photoelectron spectroscopy. XPS measurements were carried out on an Axis Ultra DLD by Kratos Analytical spectrometer. XPS data were collected with the anode at 10 mA and 15 kV; the analyzer was kept in hybrid mode, and the resolutions were 80eV pass energy for the survey scans and 20eV pass energy for the high-resolution scans. The binding energy (BE) scale was referenced to the value of 284.8 eV for the C 1s peak. The standard spin-orbit splitting of 1.18 eV and a branching ratio of 2:1 (S $2p_{3/2}$: S2 $p_{1/2}$) was used to fit the S $2p_{3/2,1/2}$ doublet. The standard spin-orbit splitting of 6 eV, and a branching ratio of 3:2 ($Ag3d_{5/2}$: $Ag3d_{3/2}$) was used to fit the Ag $3d_{5/2,3/2}$ doublet.

Atomic force microscopy. AFM was performed on a Dimension Icon FS AFM, with tapping mode at a scan rate of 0.595 Hz.

Surface profile measurement. The thickness of the film was measured with a OXT-E surface profile measuring system (Bruker Nano Surfaces Division).

Optical pump-terahertz probe (OPTP) spectroscopy. Time- and frequency-resolved THz photoconductivity measurements were conducted by an optical pump-terahertz probe (OPTP)

scheme. A regenerative Ti:sapphire amplifier system generated fundamental laser pulses with a duration of 50 fs, a repetition rate of 1 kHz, and a central wavelength of 800 nm. The generated pulses were then splitted into three branches for THz generation, sampling, and optical excitation. By shedding 800 nm ultrafast laser pulses on a 1 mm thick (110) ZnTe crystal, single-cycle THz pulses of ~1 ps duration were generated via optical rectification. 400 nm pulses were used for optical excitation and were generated by frequency doubling the 800 nm fundamental pulses via a BiB_3O_6 (BBO) crystal. The time-dependent electrical field of the THz pulse was mapped out by the electro-optic sampling method.

5.3 Results and discussion

5.3.1 Preparation and characterization of the Ag_2S films

The synthesis of the precursor for the Ag_2S films was based on the work shown in chapter 4. Using $Ag(NO)_3$ as the silver source and 3-mercaptopropionic acid (MPA) as thiol ligand, we synthesized silver thiolates (Ag-MPA) in ethylene glycol and diethylene glycol and purified and transferred this sample to the water. This aqueous Ag-MPA solution was spin-coated on slid substrates to prepare thin films (see Figure 5.1 a).

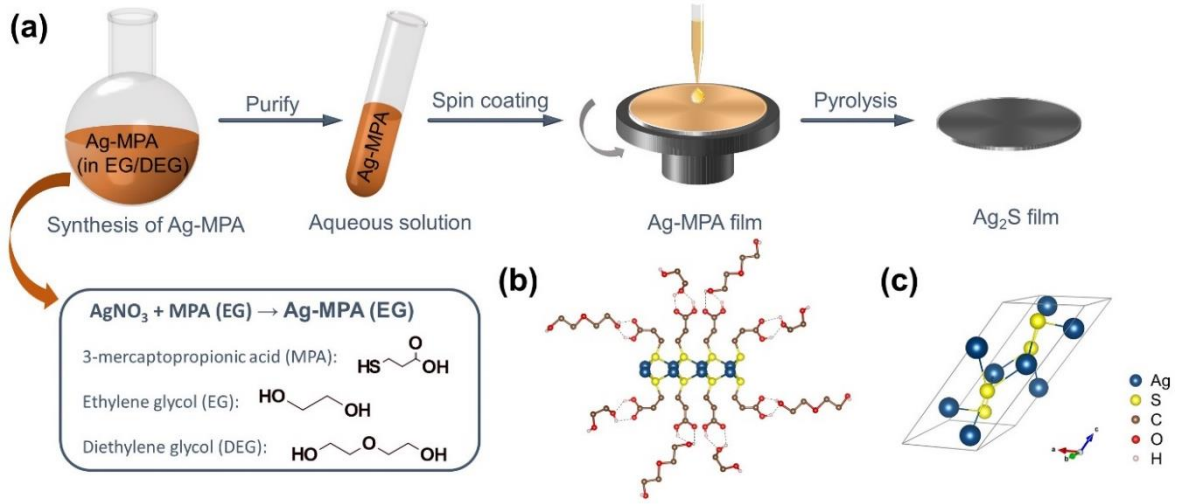

Figure 5.1. (a) Schematic presentation of solution-processed synthesis of Ag-MPA and Ag_2S thin films. Schematic representation of the crystal structures of (b) Ag-MPA and (c) Ag_2S. Monoclinic (space group $P2_1/c$) unit cell of Ag_2S with an acanthite structure (only the atoms entering into the unit cell and the nearest bonds between them,

The PXRD measurements revealed regular diffraction signals at ~4.1°, 8.1°, and 12.1° (see Figure 5.2 a), which can be interpreted in terms of a thin film of Ag-MPA with a lamellar microstructure, in which the Ag and S atoms occur regularly stacked layers with an interlayer distance of ~20 Å.[166] In this configuration, the thiol ligand MPA evenly distributed on both sides of the Ag-S layer exhibiting *gauche* and *trans* conformation (see Figure 5.2 b). The terminating carboxyl groups partially coordinated to EG and partially coordinated to DEG via hydrogen bonds, which "hold together" the Ag-MPA layers.

By heating the thin films of Ag-MPA to 180 °C for 10 min, the Ag-MPA precursor decomposed and was transformed to Ag_2S. The absorption spectra of the thin Ag_2S films exhibited an intense absorption in the visible range. At the same time, the two characteristic absorption shoulders typically presented in Ag-MPA spectra (that were associated with a donor-acceptor charge transfer from sulfur atoms to silver ions and metallophilic attraction between silver atoms, see chapter 3) disappeared, which means the pyrolysis of the Ag-MPA precursor was efficient.[173-174] PXRD showed the disappearance of the regular stacking peaks in Ag-MPA and the appearance of the characteristic α-Ag_2S diffraction signals (see Figure 5.2 a).

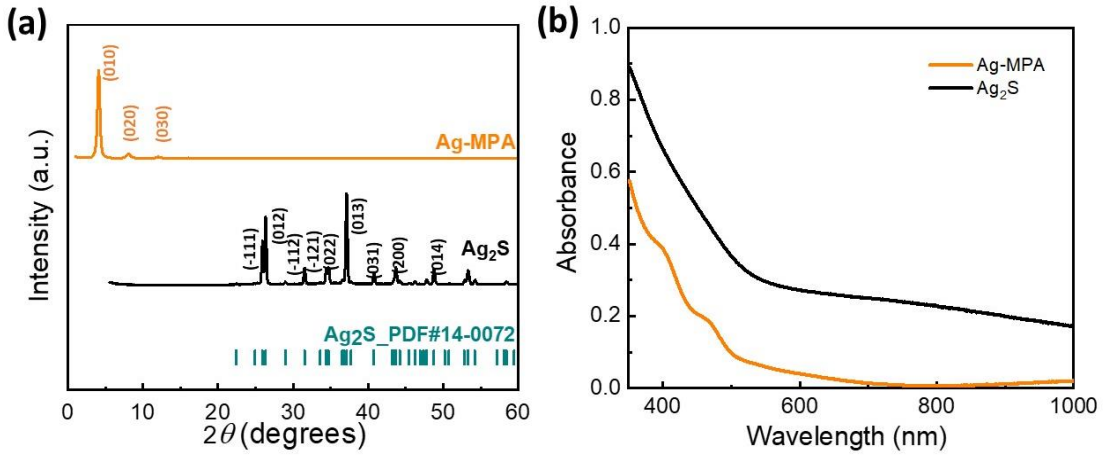

Figure 5.2. (a) PXRD patterns of Ag-MPA and Ag_2S. (b) Absorption spectra of Ag-MPA and Ag_2S.

The prepared film of Ag_2S was polycrystal. The HRTEM images showed that the interplanar crystal spacing is 2.4 Å and 3.39 Å, corresponding to the (013) and (012) crystal lattice of α-Ag_2S (see Figure 5.3).

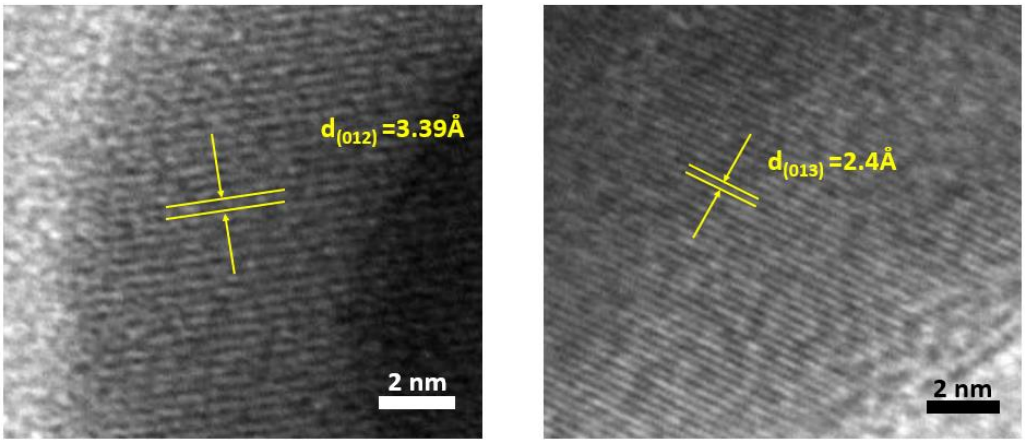

Figure 5.3. HRTEM images of Ag_2S.

The XP spectra of S 2p of the Ag_2S film showed that the dominant state of S stems from Ag_2S (~86%), with a small amount of Ag-MPA (~14%) left (see Figure 5.4).

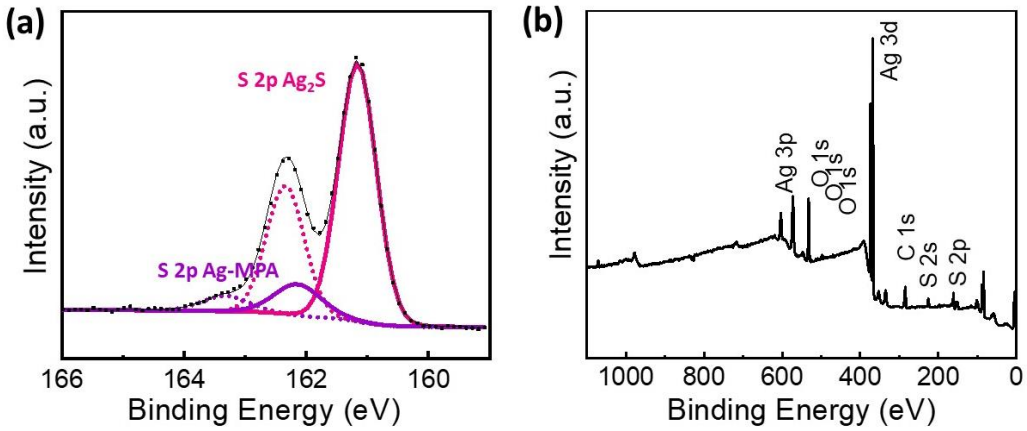

Figure 5.4. (a) High-resolution XP-spectra of S 2p of Ag_2S, solid lines represent the signals stemming from S $2p_{3/2}$, dash lines represent the signals stemming from S $2p_{1/2}$; (b) Overall XPS survey spectra for Ag_2S.

By employing AFM before and after thermal treatment, I aimed to get a better picture of the films' surface. The Ag-MPA film exhibited a microscopic fibers-like structure with a root mean square (RMS) roughness of 7 nm. After thermal treatment, relatively coarse crystals could be seen, and the RMS roughness increased a little bit to 11 nm (see Figure 5.5), demonstrating its potential for device-relevant applications (as shown above, Chen et al.[225] improved the conversion efficiency of Ag_2S based solar cell by preparation film with RMS roughness 6.8 – 11.2 nm).[231-232]

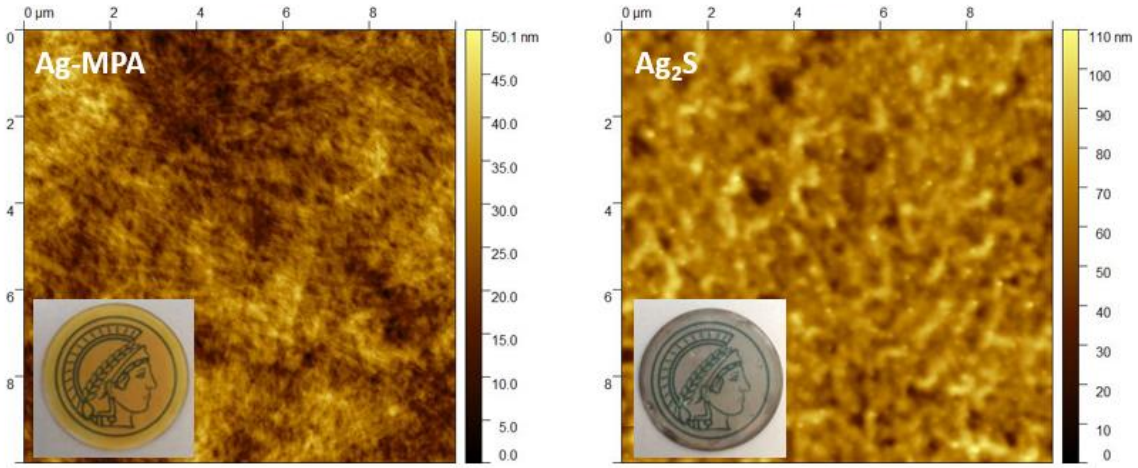

Figure 5.5. AFM image of Ag-MPA and Ag_2S film on the glass substrate, insert is the picture of Ag-MPA and Ag_2S film on the glass substrate.

The SEM image of the Ag_2S film was measured to assess the surface morphology (see Figure 5.6). The fiber-like structure seems to be partially retained in the recrystallized Ag_2S particles, which densely covered the ITO surface.

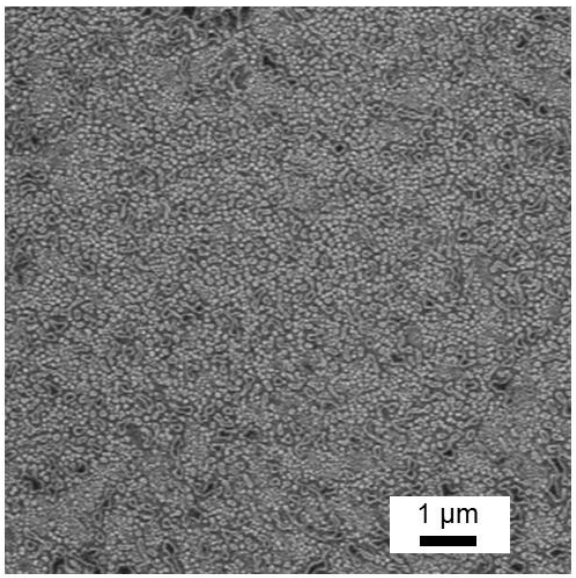

Figure 5.6. SEM image of Ag_2S thin film on ITO. The average Ag_2S grain size is ~80 nm.

5.3.2 The charge carrier dynamics of Ag_2S film

To shed light on the microscopic charge transport properties of Ag-MPA and α-Ag_2S thin films, we employed ultrafast optical pump-THz probe (OPTP) spectroscopy to probe their time- and frequency-resolved photoconductivity. As an all-optical technique, OPTP spectroscopy accesses the conductivity of materials of interest in a contact-free fashion and thus is in particular powerful for exploring the nature of charge transport in nanomaterials.[233] In a typical OPTP measurement, an ultrafast (~50 fs) laser pulse of 3.1 eV optically injects charge carriers into α-Ag_2S films following the interband transition. Subsequently, a collinearly propagating, single-cycle THz pulse (~1 ps) drives photogenerated free charge carriers oscillating, leading to THz attenuation due to free carrier absorption. The relative change of the THz electric field ($-\Delta E/E$) is proportional to the photoconductivity ($\Delta\sigma$) following the thin film approximation[234](as shown in Equation 5.1):

$$\Delta\sigma = -\frac{n+1}{Z_0 \cdot l} \cdot \frac{\Delta E}{E} \qquad \text{Equation 5.1}$$

n: represents the refractive index of the fused silica substrate in the THz range, n = 1.95;

Z_0: the impedance of vacuum, Z_0 = 377 Ω;

l: the optical penetration depth.

Figure 5.7 compares the photoconductivity dynamics of Ag-MPA and α-Ag_2S thin films at the same absorbed photon density of ~3.4 × 10^{14} cm^{-2}. Upon excitation, the optically injected charge carriers in Ag-MPA thin film exhibited a finite photoconductivity of ~20 S/m and a lifetime of ~1 ps. By contrast, photogenerated charge carriers in the α-Ag_2S thin film showed as ~300 times higher photoconductivity and a substantially longer lifetime, demonstrating their bright perspectives in photovoltaic and optoelectronic applications.

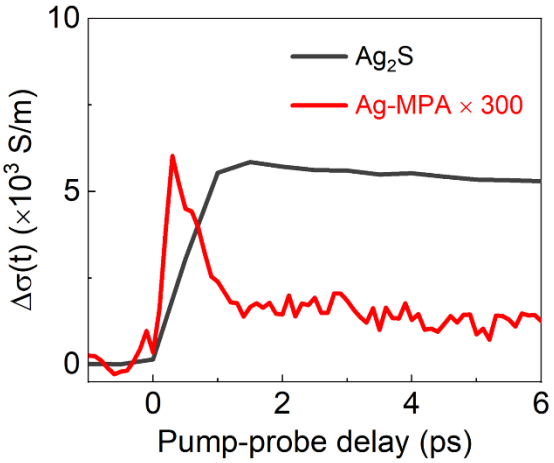

Figure 5.7. THz photoconductivity of Ag_2S and Ag-MPA thin films. Time-resolved THz photoconductivity of Ag_2S thin film (black line) and Ag-MPA thin film (red line, 300 times multiplied amplitude). Samples are excited by a 400 nm pulsed laser with the same absorbed photon density of ~3.4 × 10^{14} cm^{-2}, and their photoconductivity is probed by a single-cycle THz pulse under the dry N_2 environment.

To further elucidate their charge transport properties, we measured the frequency-resolved complex photoconductivity at ~1 ps after the maximum photoconductivity. Figure 5.8 shows the real and imaginary components as a function of frequency for α-Ag_2S and Ag-MPA thin films, respectively. In both cases, the frequency-resolved complex photoconductivity manifested a real positive component and a negative imaginary component and could be phenomenologically described by the Drude-Smith (DS) model (represented by the solid and dash lines in Figure 5.8 a and Figure 5.8 b). The DS model considers charge transport restricted by the spatial confinement, e.g. preferential backscattering at grain boundaries or defects in the materials, and can be written as Equation 5.2:

$$\sigma(\omega) = \frac{\omega_p^2 \varepsilon_0 \tau}{1-i\omega\tau}\left(1 + \frac{c}{1-i\omega\tau}\right) \qquad \text{Equation 5.2}$$

ω_P: the plasma frequency;

τ: effective carrier scattering time;

ε_0: vacuum permittivity;

c: the probability of backscattering, with values spanning from 0 (for isotropic scattering) to -1 (for preferential scattering).

The DS fit to the data yields τ of 39 ± 2 fs and 42 ± 4 fs, and c parameters of -0.49 ± 0.01 and -0.92 ± 0.02 for α-Ag_2S and Ag-MPA thin films, respectively. Given the inferred scattering time and c parameter, we estimated the DC mobility (μ) of α-Ag_2S thin film to be ~150 $cm^2\ V^{-1}\ s^{-1}$ following Equation 5.3.

$$\mu = \frac{e\tau}{m^*} \times (1 + c) \qquad Equation\ 5.3$$

e: the elementary charge;

m^*: the effective charge carrier mass obtained from reference $m^* = 0.23\ m_0$.[235]

To justify the obtained mobility based on the DS analysis, we further calculated the mobility by thin film approximation, as shown in Equation 5.1. This gives rise to $\varphi \cdot \mu$ = 17.3 $cm^2\ V^{-1}\ s^{-1}$, with φ ranging from 0 to 1 stands for the photon-to-charge conversion ratio.

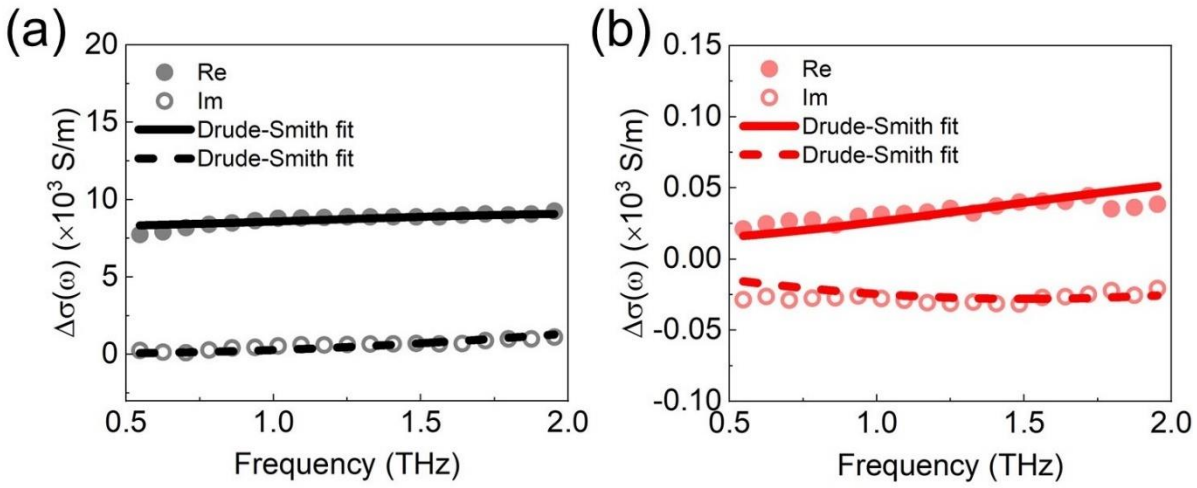

Figure 5.8. Frequency-resolved THz photoconductivity of (a) Ag_2S thin film and (b) Ag-MPA thin film measured at ~1 ps after the maximum photoconductivity. The solid and dash lines represent the Drude-Smith model describing the real and imaginary components of the complex THz photoconductivity, respectively.

Along with the remarkable charge mobility, another figure of merit of α-Ag_2S that would benefit photovoltaic applications lies in the long charge carrier lifetime or the low decay rate. Depending on the charge carrier density in the material, charge carriers can recombine via distinct channels such as monomolecular recombination, bimolecular recombination, and Auger recombination. To unveil the charge recombination rates associated with different recombination channels, we performed pump-fluence dependent photoconductivity dynamics

for an α-Ag_2S thin film with incident pump fluences ranging from 4.4 to 82.5 μJ/cm^2. As shown in Figure 5.9, the photoconductivity decayed faster at elevated pump fluences, as a result of the more pronounced contributions from the higher-order decay channels (e.g. bimolecular and Auger recombination).[148, 236]

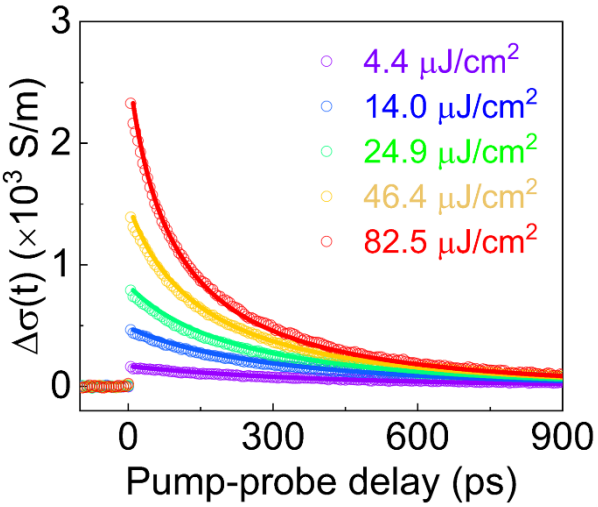

Figure 5.9. Charge carrier dynamics of Ag_2S thin films at varied charge carrier concentrations. Fluence-dependent THz photoconductivity dynamics of Ag_2S thin film following 3.1 eV excitations, with incident pump fluences ranging from 4.4 to 82.5 μJ/cm^2. The solid lines represent a global fitting to the recombination rates equation as discussed in the main text. The recombination rates k_1, k_2 and k_3 are extracted to be 2.08×10^9 s^{-1}, 7.13×10^{-10} cm^3 s^{-1} and 1.19×10^{-29} cm^6 s^{-1}, respectively.

To clarify the charge carrier density-dependent recombination rates, we globally fitted the pump fluence dependent photoconductivity dynamics with the coupled rate Equation 5.4:

$$\frac{dn(t)}{dt} = -k_1 n - k_2 n^2 - k_3 n^3 \qquad \text{Equation 5.4}$$

$n(t)$: the charge carrier density at the pump-probe delay t;

k_1: the monomolecular recombination rate coefficient accounting for the trapping-related process;

k_2: the bimolecular recombination rate coefficient originating from the recombination of electron-hole pairs;

k_3: the Auger recombination rate coefficient.

Based on the global fitting, k_1, k_2, and k_3 were calculated to be 2.08×10^{9} s^{-1}, 7.13×10^{-10} $cm^3\,s^{-1}$, and 1.19×10^{-29} $cm^6\,s^{-1}$, respectively. This gives rise to the total decay rate (R_{total}), as shown in Figure 5.10 a (black line). The high charge mobility μ and the low recombination rate R_{total} motivated us to further estimate the diffusion length L in α-Ag_2S thin film (Equation 5.5).

$$L(n) = \sqrt{\frac{\mu k_B T e}{R_{total}(n)}} \qquad \text{Equation 5.5}$$

k_B: the Boltzmann constant;

T: the measurement temperature.

Figure 5.10 b, plotted the lower bound limit of L as a function of carrier density by adopting the photon to charge branching ratio φ = 1. We found that the lower bound limit of L was already around 500 nm at relatively low charge carrier densities (< 10^{19} cm^{-3}).

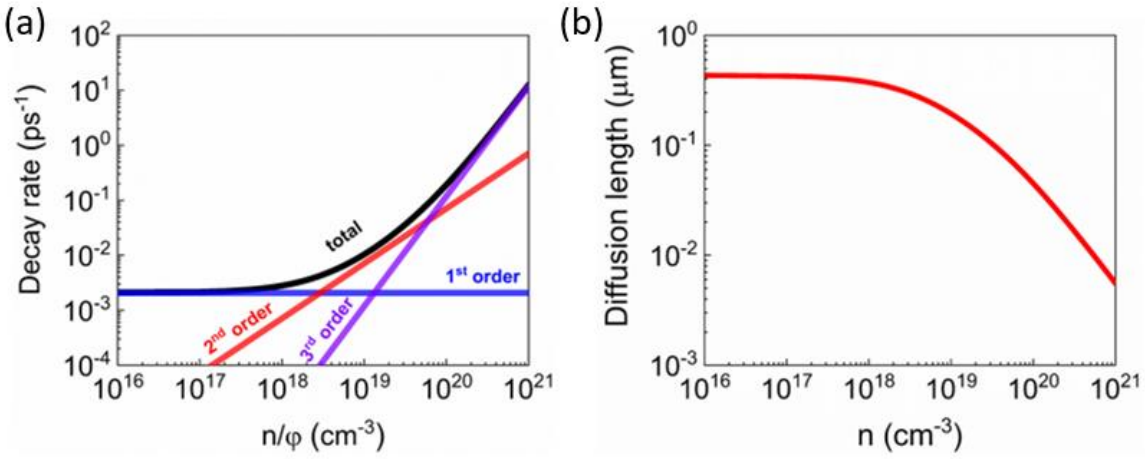

Figure 5.10. (a) Charge carrier decay rates of Ag_2S thin films at varied charge carrier concentrations. Here φ stands for the photon-to-charge conversion ratio representing the number of charges created per absorbed photon. (b) Charge carrier diffusion length of Ag_2S thin films as a function of charge carrier concentration.

To provide more insights into the charge transport mechanism, we recorded photoconductivity dynamics of α-Ag_2S thin film at varying temperatures, ranging from 350 K to 78 K. As shown in Figure 5.11 a, the photoconductivity increased with decreasing temperature. The negative temperature coefficient of conductivity ($\frac{d\mu}{dT} < 0$) suggests that photogenerated charge carriers migrated in α-Ag_2S thin films following band-like transport.

The power law fitting between the maximum photoconductivity and temperature (see Figure 5.10 b) yielded a power index close to -1, implying that both phonon and impurity scattering limited the motion of charge carriers in α-Ag_2S.[237]

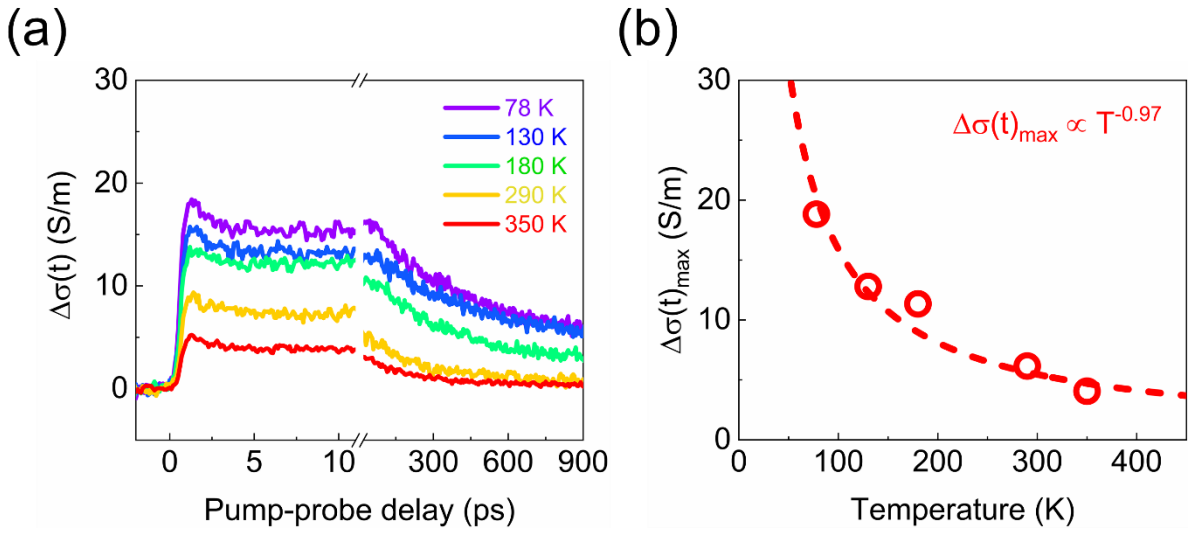

Figure 5.11. Temperature-dependent THz photoconductivity of Ag_2S thin films. (a) Temperature-dependent time-resolved THz photoconductivity dynamics of Ag_2S thin films following 400 nm excitation with a fixed incident pump fluence of 1.8 μJ/cm^2. (b) The maximum THz photoconductivity as a function of temperature. The dashed line represents the power law fitting to the data.

5.3.3 The characterization of freestanding Ag_2S film

To realize freestanding Ag_2S films, I mixed aqueous Ag-MPA solutions with PVA, similar to what I outlined in chapter 4. Here the idea is that the PVA component provides excellent mechanical stability and a scaffold for the formation of Ag_2S from Ag-MPA in order to realize self-supported films with all the beneficial features of Ag_2S films after pyrolysis of Ag-MPA on the PVA matrix. The PXRD spectra of as-synthesized PVA-Ag_2S film exhibited a broad halo at ~19.3° associated with the semicrystalline nature of PVA and diffraction signal of crystalline α-Ag_2S (Figure 5.12 a).

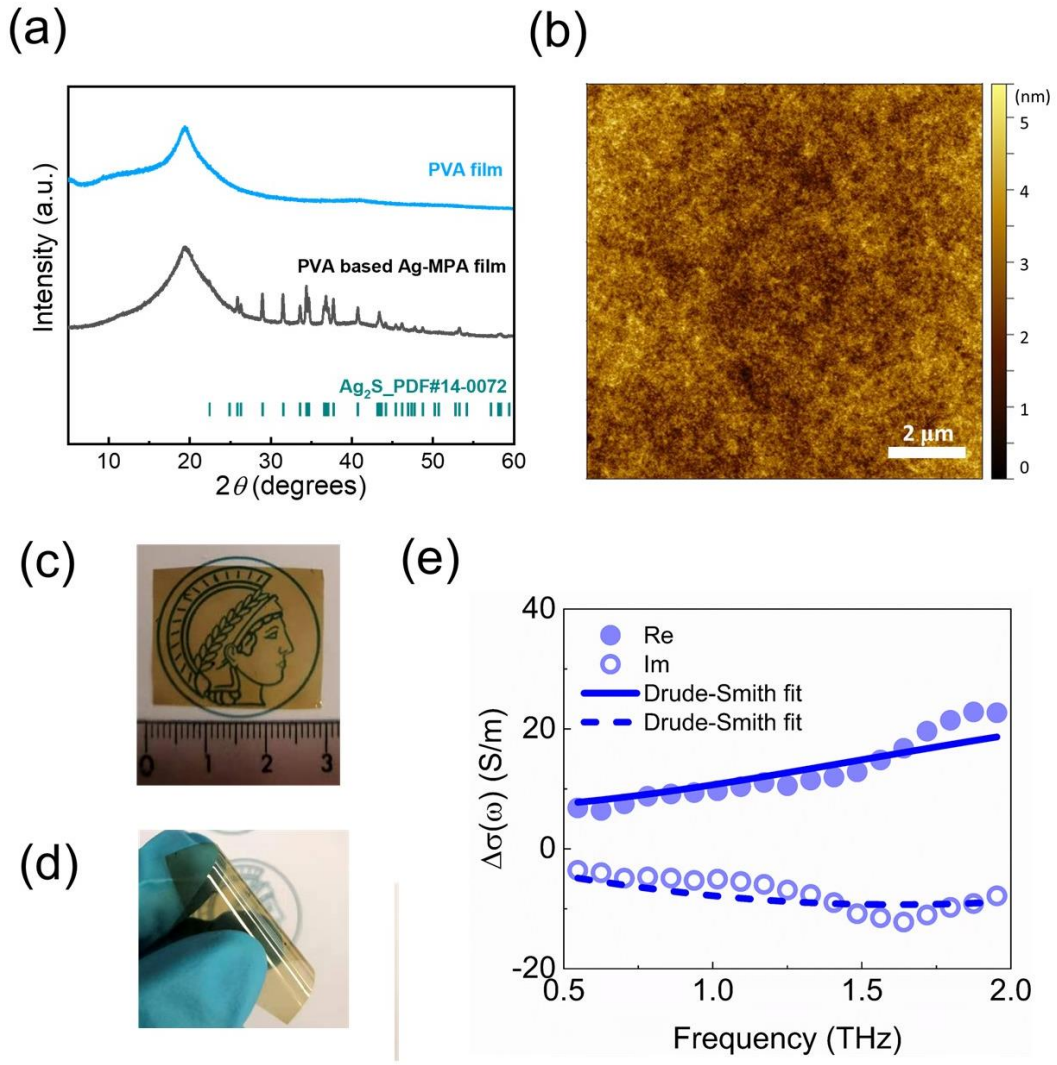

Figure 5.12. Synthesis and THz photoconductivity of Ag_2S-PVA thin film. (a) PXRD patterns of pure PVA thin film and Ag_2S-PVA thin film. (b) AFM image of Ag_2S-PVA thin film. (c) A picture of an as-synthesized freestanding PVA-Ag_2S thin film with a length of ~3 cm. (d) A picture of bending an as-synthesized freestanding PVA-Ag_2S thin film with exceptional flexibility. (e) Frequency-resolved THz photoconductivity of freestanding PVA-Ag_2S thin film measured at ~1 ps after the maximum photoconductivity. The sample is excited by a 400 nm pulsed laser with an incident pump fluence of 3.3 μJ/cm^2. The solid and dash lines represent the Drude-Smith model describing the real and imaginary components of the complex THz photoconductivity, respectively.

The resulting PVA-Ag_2S film exhibited a flat surface with an extremely low RMS roughness of 635 pm (Figure 5.12 b), a lateral length of ~3 cm (Figure 5.12 c), and retained structural integrity during bending (Figure 5.12 d). Frequency-resolved complex photoconductivity for the freestanding Ag_2S-PVA thin film could also be well-described by the Drude-Smith model

as discussed above, yielding τ of 42 ± 4 fs and c of -0.92 ± 0.02, respectively. Compared to the supported α-Ag_2S film, the addition of PVA led to an increase in the absolute value of c parameter, while τ remains almost the same within the experimental error. This led to a decrease of mobility of ~35 $cm^2V^{-1}s^{-1}$ in the DC limit, still exceptional for typical conducting polymers that used for flexible electronics. The reduced mobility may arise from the disturbed crystallization process of α-Ag_2S and the separation of the conducting α-Ag_2S domains, as consequences of the introduction of PVA. Further tailoring the relative ratio between the aqueous Ag-MPA solution and PVA and optimizing the crystallization conditions may help to increase the mobility of freestanding Ag_2S-PVA thin films.

5.4 Conclusion

In this chapter, we demonstrated a solution-processed synthesis path for α-Ag_2S thin films by employing aqueous Ag-MPA solutions as the precursor and subsequently investigated their charge transport properties by ultrafast THz spectroscopy. During heating, Ag-MPA converted into α-Ag_2S by pyrolysis of S-C bonds and rearrangement of Ag and S atoms, producing wafer-sized, highly crystalline α-Ag_2S thin films. Further improvements can be expected when the thermal treatment is optimized for removing all Ag-MPA to obtain higher purified Ag_2S thin films. THz photoconductivity measurements revealed that the photogenerated charge carriers migrated in α-Ag_2S thin films by band-like transport with exceptional mobility of ~150 $cm^2V^{-1}s^{-1}$. To produce free-standing films, we blended Ag-MPA with PVA in thin films and converted the Ag-MPA into α-Ag_2S. While this approach indeed yielded free-standing films, the introduction of PVA slightly hampered the charge transport properties. Nevertheless, the freestanding α-Ag_2S/PVA thin film still exhibited decent mobility of ~35 $cm^2V^{-1}s^{-1}$, promising for flexible electronics and optoelectronics.

6. Conclusion

In this thesis, new lamellar silver thiolates (Ag-MPA) were designed and produced with reversible temperature-dependent, blue-to-near infrared optical transitions. The structural flexibility of Ag-MPA is responsible for the *gauche* - *trans* conformation transitions that lead to the thermally addressable optical transitions. The polymer-like nature of Ag-MPA makes up-scaling the reaction feasible and allows for facile processing. The temperature-dependent, fully reversible optical transitions, spanning the blue-to-NIR range, unveil many new possibilities for applications ranging from bio-imaging to optoelectronics. Furthermore, reactions carried out at high precursor concentrations lead to the *in situ* formation of Ag-MPA gels.

With further modifications, silver thiolate supramolecular gels were obtained with enhanced NIR fluorescence quantum yield without sacrificing the intrinsically low toxicity and good water solubility. The mechanical properties could be improved and tuned significantly by the blending of Ag-MPA with poly(vinyl alcohol) due to its excellent compatibility with aqueous poly(vinyl alcohol) solution. This bio-compatible strong gel can be applied in many biomedical fields, such as drug delivery, imaging in vivo, and wound dressing.

Furthermore, since the product after thermal treatment of silver thiolate coordination polymer is silver sulfide, silver thiolates are interesting precursors to prepare silver sulfide thin films. Thin film from silver thiolates can be easily prepared by spin-coating thanks to the polymer character. The thickness can be controlled by the concentration and spinning speed. This, the pyrolysis route of silver thiolates for smooth Ag_2S thin films, is versatile and can be applied on different substrates. Employing ultrafast terahertz spectroscopy, it was revealed that photogenerated charge carriers migrate in supported α-Ag_2S thin films following band-like transport, with a high intrinsical mobility of ~150 $cm^2V^{-1}s^{-1}$ and a diffusion length exceeding 0.4 μm. A new method was developed to synthesize self-supported films of α-Ag_2S by first blending Ag-MPA with PVA, followed by pyrolysis to obtain freestanding α-Ag_2S thin films, which exhibit decent mobility of ~35 $cm^2V^{-1}s^{-1}$, being competitive with the highest values achieved by flexible films based on TMCs. These results pave the way for utilizing α-Ag_2S thin films as flexible and versatile materials towards wearable optoelectronic and thermoelectric devices.

Curriculum vitae

PERSONAL INFORMATION

Junren Wang

Sex: female

Date of birth: 13.08.1992

Nationality: Chinese

Email: wang01@mpip-mainz.mpg.de

shuoyuechenzhixing@163.com

EDUCATION AND TRAINING

09/2018 – present

Doctoral Candidate at the Department of Physical Chemistry of Polymers

Max Planck Institute for Polymer Research, Mainz, Germany

Supervised by Prof. Dr. Katharina Landfester, Dr. Andreas Riedinger and Dr. Calum Ferguson

Title: Silver Sulfide Compounds and their Optical and Mechanical Properties and Charge Carrier Dynamics

09/2015 – 03/2018

Master of Science at the Department of Materials Science and Engineering

Beihang University, Beijing, China

Supervised by Prof. Dr. Huimin Lu

Title: Electrochemical Performance and Controllable Preparation of Cathode Catalysts for Aluminum-Air Battery

09/2011 – 06/2015

Bachelor of Science at the Department of Materials Science and Engineering

Shandong University, Jinan, China

Supervised by Dr. Haibin Zhao

Title: Design and Optimization of Microcellular Plastic Foaming Experimental Device

PUBLICATIONs

Junren Wang, Robert Graf, Kaloian Koynov, Xuyang Yao, Long Yang, Riedinger Andreas*. Silver thiolate supramolecular gel with near infrared emission and enhanced mechanical property. In preparation.

Junren Wang[1], Shuai Fu[1], Heng Zhang, Henry Halim, Shuai Chen, Wenhao Zheng, Mischa Bonn, Katharina Landfester, Riedinger Andreas*, Hai I. Wang*. Solution-Processed Wafer-Scale Ag_2S Thin Films: Synthesis and Superior Charge Transport Properties. In preparation.

Junren Wang, Robert Graf, Riedinger Andreas*. Lamellar silver thiolate coordination polymers with reversibly switchable blue-to-near infrared optical transitions. ***J. Mater. Chem. C***, 2021, 9(34): 11079-11084.. (SCI, IF=7.393, Q1)

Publications from master thesis:

Junren Wang, Huimin Lu*, Qingshui Hong, Yuan Cao, Xudong Li, Junjie Bai. Porous N, S-codoped carbon architectures with bimetallic sulphide nanoparticles encapsulated in graphitic layers: highly active and robust electrocatalysts for the oxygen reduction reaction in Al-air batteries. ***Chem. Eng. J.***, 2017, *330*, 1342-1350. (SCI, IF=10.652, Q1)

Hong Qingshui, Lu Huimin*, **Wang Junren**. CuO Nanoplatelets with Highly Dispersed Ce-Doping Derived from Intercalated Layered Double Hydroxides for Synergistically Enhanced Oxygen Reduction Reaction in Al–Air Batteries. ***ACS Sustain. Chem. Eng.***, 2017, 5, 9169-9175. (SCI, IF=7.632, Q1)

References

1. Heine, J.; Müller-Buschbaum, K., Engineering Metal-Based Luminescence in Coordination Polymers and Metal–Organic Frameworks. *Chem. Soc. Rev.* **2013**, *42*, 9232-9242.

2. Kreno, L. E.; Leong, K.; Farha, O. K.; Allendorf, M.; Van Duyne, R. P.; Hupp, J. T., Metal–Organic Framework Materials as Chemical Sensors. *Chem. Rev.* **2012**, *112*, 1105-1125.

3. Perry Iv, J. J.; Perman, J. A.; Zaworotko, M. J., Design and Synthesis of Metal–Organic Frameworks Using Metal–Organic Polyhedra as Supermolecular Building Blocks. *Chem. Soc. Rev.* **2009**, *38*, 1400-1417.

4. Linton, B.; Hamilton, A. D., Formation of Artificial Receptors by Metal-Templated Self-Assembly. *Chem. Rev.* **1997**, *97*, 1669-1680.

5. Batten, S. R.; Neville, S. M.; Turner, D. R., Coordination Polymers: Design, Analysis and Application; *Royal Society of Chemistry*, 2008.

6. Venkataraman, D.; Du, Y.; Wilson, S. R.; Hirsch, K. A.; Zhang, P.; Moore, J. S., A Coordination Geometry Table of the D-Block Elements and Their Ions. *J. Chem. Educ.* **1997**, *74*, 915.

7. Yam, V. W.-W.; Lo, K. K.-W., Luminescent Polynuclear D 10 Metal Complexes. *Chem. Soc. Rev.* **1999**, *28*, 323-334.

8. Yam, V. W.-W.; Lo, K. K.-W.; Wong, K. M.-C., Luminescent Polynuclear Metal Acetylides. *J. Organomet. Chem.* **1999**, *578*, 3-30.

9. Alarcon, E. I.; Udekwu, K.; Skog, M.; Pacioni, N. L.; Stamplecoskie, K. G.; González-Béjar, M.; Polisetti, N.; Wickham, A.; Richter-Dahlfors, A.; Griffith, M., The Biocompatibility and Antibacterial Properties of Collagen-Stabilized, Photochemically Prepared Silver Nanoparticles. *Biomaterials* **2012**, *33*, 4947-4956.

10. Hebb, M. H., Electrical Conductivity of Silver Sulfide. *J. Chem. Phys.* **1952**, *20*, 185-190.

11. Wagner, C., Investigations on Silver Sulfide. *J. Chem. Phys.* **1953**, *21*, 1819-1827.

12. Berger, L. I., *Semiconductor Materials*; *CRC press*, **2020.**

13. Parrott, J., The High Temperature Thermal Conductivity of Semiconductor Alloys. *Proc. Phys., Soc. (1958-1967)* **1963**, *81*, 726.

14. Tricoli, A.; Righettoni, M.; Teleki, A., Semiconductor Gas Sensors: Dry Synthesis and Application. *Angew. Chem. Int. Ed.* **2010**, *49*, 7632-7659.

15. Palacios-Berraquero, C.; Kara, D. M.; Montblanch, A. R.-P.; Barbone, M.; Latawiec, P.; Yoon, D.; Ott, A. K.; Loncar, M.; Ferrari, A. C.; Atatüre, M., Large-Scale Quantum-Emitter Arrays in Atomically Thin Semiconductors. *Nat. commun.* **2017**, *8*, 1-6.

16. Zaidi, B., Introductory Chapter: Introduction to Photovoltaic Effect. *Sol. Energy Mater Sol. Cells* **2018**, 1-8.

17. Nelson, W. E. Area Photoconductivity in Lithium Fluoride. *Kansas State University*, 1974.

18. Łukasiak, L.; Jakubowski, A., History of Semiconductors. *J. Telecommun. Inf. Technol.* **2010**, 3-9.

19. Hoddeson, L., The Discovery of the Point-Contact Transistor. *His.t Stud. Phy. Sci.* **1981**, *12*, 41-76.

20. Ekimov, A.; Onuschenko, A., The Quantum Size Effect in Three-Dimensional Microscopic Semiconductors. *JETP Lett* **1981**, *34*, 363.

21. Nozik, A. J., Quantum Dot Solar Cells. *Physica E Low Dimens. Syst. Nanostruct.* **2002**, *14*, 115-120.

22. Kamat, P. V., Quantum Dot Solar Cells. The Next Big Thing in Photovoltaics. *J. Phys. Chem. Lett.* **2013**, *4*, 908-918.

23. Nozik, A. J.; Beard, M. C.; Luther, J. M.; Law, M.; Ellingson, R. J.; Johnson, J. C., Semiconductor Quantum Dots and Quantum Dot Arrays and Applications of Multiple Exciton Generation to Third-Generation Photovoltaic Solar Cells. *Chem. Rev.* **2010**, *110*, 6873-6890.

24. He, D.; Garg, S.; Wang, Z.; Li, L.; Rong, H.; Ma, X.; Li, G.; An, T.; Waite, T. D., Silver Sulfide Nanoparticles in Aqueous Environments: Formation, Transformation and Toxicity. *Environ. Sci. Nano* **2019**, *6*, 1674-1687.

25. Yahua, B. J. Y., Retrieve Silver Nitrate Agent from Waste Solution of Silver Sulfide Use Aluminium as Reducing Agent [J]. *J. Hefei University Tech. (Nat. Sci.)* **1996**, *4*.

26. Zhang, X.; Liu, M.; Liu, H.; Zhang, S., Low-Toxic Ag2s Quantum Dots for Photoelectrochemical Detection Glucose and Cancer Cells. *Biosens. Bioelectron.* **2014**, *56*, 307-312.

27. Tang, R.; Xue, J.; Xu, B.; Shen, D.; Sudlow, G. P.; Achilefu, S., Tunable Ultrasmall Visible-to-Extended near-Infrared Emitting Silver Sulfide Quantum Dots for Integrin-Targeted Cancer Imaging. *ACS nano* **2015**, *9*, 220-230.

28. Sharma, R.; Chang, Y., The Ag− S (Silver-Sulfur) System. *Bull. alloy phase diagr.* **1986**, *7*, 263-269.

29. Sadovnikov, S.; Gusev, A.; Chukin, A.; Rempel, A., High-Temperature X-Ray Diffraction and Thermal Expansion of Nanocrystalline and Coarse-Crystalline Acanthite A-Ag2s and Argentite B-Ag2s. *Phys. Chem. Chem. Phys.* **2016**, *18*, 4617-4626.

30. Sadanaga, R.; Sueno, S., X-Ray Study on the A-B Transition of Ag2s. *Mineral. Mag.* **1967**, *5*, 124-143.

31. Sadovnikov, S. a.; Gusev, A.; Rempel, A., Artificial Silver Sulfide Ag2s: Crystal Structure and Particle Size in Deposited Powders. *Superlattices Microstruct.* **2015**, *83*, 35-47.

32. Shi, X.; Chen, H.; Hao, F.; Liu, R.; Wang, T.; Qiu, P.; Burkhardt, U.; Grin, Y.; Chen, L., Room-Temperature Ductile Inorganic Semiconductor. *Nat. Mater.* **2018**, *17*, 421-426.

33. Cava, R.; Reidinger, F.; Wuensch, B., Single-Crystal Neutron Diffraction Study of the Fast-Ion Conductor B-Ag2s between 186 and 325° C. *J. Solid State Chem.* **1980**, *31*, 69-80.

34. Sadovnikov, S.; Gusev, A.; Rempel, A., Nonstoichiometry of Nanocrystalline Monoclinic Silver Sulfide. *Phys. Chem. Chem. Phys.* **2015**, *17*, 12466-12471.

35. Sadovnikov, S.; Gusev, A.; Rempel, A., An in Situ High-Temperature Scanning Electron Microscopy Study of Acanthite–Argentite Phase Transformation in Nanocrystalline Silver Sulfide Powder. *Phys. Chem. Chem. Phys.* **2015**, *17*, 20495-20501.

36. Blanton, T.; Misture, S.; Dontula, N.; Zdzieszynski, S., In Situ High-Temperature X-Ray Diffraction Characterization of Silver Sulfide, Ag2S. *Powder Diffr.* **2011**, *26*, 114.

37. Junod, P.; Hediger, H.; Kilchör, B.; Wullschleger, J., Metal-Non-Metal Transition in Silver Chalcogenides. *Philos. Mag.* **1977**, *36*, 941-958.

38. Junod, P. Relations Entre La Structure Cristalline Et Les Propriétés Électroniques Des Combinaisons Ag-2S, Ag-2Se, Cu-2Se. *ETH Zurich*, 1959.

39. O'Reilly, E. P., Valence Band Engineering in Strained-Layer Structures. *Semicond. Sci. Technol.* **1989**, *4*, 121.

40. Takagahara, T.; Takeda, K., Theory of the Quantum Confinement Effect on Excitons in Quantum Dots of Indirect-Gap Materials. *Phy. Rev. B* **1992**, *46*, 15578.

41. Thambidurai, M.; Muthukumarasamy, N.; Agilan, S.; Murugan, N.; Vasantha, S.; Balasundaraprabhu, R.; Senthil, T., Strong Quantum Confinement Effect in Nanocrystalline Cds. *J. Mater. Sci.* **2010**, *45*, 3254-3258.

42. Zhang, Y.; Liu, Y.; Li, C.; Chen, X.; Wang, Q., Controlled Synthesis of Ag2s Quantum Dots and Experimental Determination of the Exciton Bohr Radius. *J. Phys. Chem. C* **2014**, *118*, 4918-4923.

43. Bayart, F.; Pellegrino, D.; Seoane-Sepúlveda, J. B., The Bohr Radius of the N-Dimensional Polydisk Is Equivalent to (Log f_0 N)/N. *Adv. Math.* **2014**, *264*, 726-746.

44. Kholod, A., Soviet Newspaper Editors 1941 as a Semiotic-Color Spectrum from the Point of View of Quantum Theory. *LBC 83.56 я73*.

45. Rabouw, F. T.; de Mello Donega, C., Excited-State Dynamics in Colloidal Semiconductor Nanocrystals. *Springer* **2017**, 1-30.

46. Meherzi-Maghraoui, H.; Dachraoui, M.; Belgacem, S.; Buhre, K.; Kunst, R.; Cowache, P.; Lincot, D., Structural, Optical and Transport Properties of Ag2s Films Deposited Chemically from Aqueous Solution. *Thin Solid Films* **1996**, *288*, 217-223.

47. Hirsch, M. P., Toxicity of Silver Sulfide-Spiked Sediments to the Freshwater Amphipod (Hyalella Azteca). *Environ. Toxicol. Chem.* **1998**, *17*, 601-604.

48. Du, Y.; Xu, B.; Fu, T.; Cai, M.; Li, F.; Zhang, Y.; Wang, Q., Near-Infrared Photoluminescent Ag2s Quantum Dots from a Single Source Precursor. *J. Am. Chem. Soc.* **2010**, *132*, 1470-1471.

49. Fox, B. S.; Beyer, M. K.; Bondybey, V. E., Coordination Chemistry of Silver Cations. *J. Am. Chem. Soc.* **2002**, *124*, 13613-13623.

50. Becke, A. D., Density-Functional Exchange-Energy Approximation with Correct Asymptotic Behavior. *Phy. rev. A* **1988**, *38*, 3098.

51. Wang, F.; Wang, Y.-T.; Yu, H.; Chen, J.-X.; Gao, B.-B.; Lang, J.-P., One Unique 1d Silver (I)-Bromide-Thiol Coordination Polymer Used for Highly Efficient Chemiresistive Sensing of Ammonia and Amines in Water. *Inorg. Chem.* **2016**, *55*, 9417-9423.

52. Huang, X.; Li, H.; Tu, Z.; Liu, L.; Wu, X.; Chen, J.; Liang, Y.; Zou, Y.; Yi, Y.; Sun, J., Highly Conducting Neutral Coordination Polymer with Infinite Two-Dimensional Silver–Sulfur Networks. *J. Am. Chem. Soc.* **2018**, *140*, 15153-15156.

53. Li, B.; Huang, R. W.; Qin, J. H.; Zang, S. Q.; Gao, G. G.; Hou, H. W.; Mak, T. C., Thermochromic Luminescent Nest-Like Silver Thiolate Cluster. *Chem. Eur. J* **2014**, *20*, 12416-12420.

54. Xie, Y. P.; Jin, J. L.; Lu, X.; Mak, T. C., High-Nuclearity Silver Thiolate Clusters Constructed with Phosphonates. *Angew. Chem. Int. Ed.* **2015**, *54*, 15176-15180.

55. Allen, F. H.; Davies, J. E.; Galloy, J. J.; Johnson, O.; Kennard, O.; Macrae, C. F.; Mitchell, E. M.; Mitchell, G. F.; Smith, J. M.; Watson, D. G., The Development of Versions 3 and 4 of the Cambridge Structural Database System. *J. Chem. Inf. Model.* **1991**, *31*, 187-204.

56. Young, A. G.; Hanton, L. R., Square Planar Silver (I) Complexes: A Rare but Increasingly Observed Stereochemistry for Silver (I). *Coord. Chem. Rev.* **2008**, *252*, 1346-1386.

57. Silva, R. M.; Smith, M. D.; Gardinier, J. R., Anion-and Solvent-Directed Assembly in Silver Bis (Thioimidazolyl) Methane Chemistry and the Silver− Sulfur Interaction. *Inorg. Chem.* **2006**, *45*, 2132-2142.

58. Lin, S.; Cui, Y.-Z.; Qiu, Q.-M.; Han, H.-L.; Li, Z.-F.; Liu, M.; Xin, X.-L.; Jin, Q.-H., Synthesis, Characterization, Luminescent Properties of Silver (I) Complexes Based on Organic P-Donor Ligands and Mercaptan Ligands. *Polyhedron* **2017**, *134*, 319-329.

59. Udris, J., The Analysis of Tin Stabilisers Used in Poly (Vinyl Chloride) Compositions. *Analyst* **1971**, *96*, 130-139.

60. Awaleh, M. O.; Badia, A.; Brisse, F.; Bu, X.-H., Synthesis and Characterization of Silver (I) Coordination Networks Bearing Flexible Thioethers: Anion Versus Ligand Dominated Structures. *Inorg. Chem.* **2006**, *45*, 1560-1574.

61. Hadjikakou, S.; Ozturk, I.; Xanthopoulou, M.; Zachariadis, P.; Zartilas, S.; Karkabounas, S.; Hadjiliadis, N., Synthesis, Structural Characterization and Biological Study of New Organotin (Iv), Silver (I) and Antimony (Iii) Complexes with Thioamides. *J. Inorg. Biochem.* **2008**, *102*, 1007-1015.

62. Okano, A.; James, R. C.; Pierce, J. G.; Xie, J.; Boger, D. L., Silver (I)-Promoted Conversion of Thioamides to Amidines: Divergent Synthesis of a Key Series of Vancomycin Aglycon Residue 4 Amidines That Clarify Binding Behavior to Model Ligands. *J. Am. Chem. Soc.* **2012**, *134*, 8790-8793.

63. Tong, M. C.; Chen, W.; Sun, J.; Ghosh, D.; Chen, S., Dithiocarbamate-Capped Silver Nanoparticles. *J. Phys. Chem. B* **2006**, *110*, 19238-19242.

64. Lerchi, M.; Reitter, E.; Simon, W.; Pretsch, E.; Chowdhury, D. A.; Kamata, S., Bulk Optodes Based on Neutral Dithiocarbamate Ionophores with High Selectivity and Sensitivity for Silver and Mercury Cations. *Anal. Chem.* **1994**, *66*, 1713-1717.

65. Webster, J., The Solubility of Gold and Silver in the System Au□ Ag□ S□ O2□ H2o at 25° C and 1 Atm. *Geochim. Cosmochim. Acta* **1986**, *50*, 1837-1845.

66. Martell, A. E.; Smith, R. M., Critical Stability Constants; *Springer*, **1974**; Vol. 1.

67. Yam, V. W.-W.; Au, V. K.-M.; Leung, S. Y.-L., Light-Emitting Self-Assembled Materials Based on D8 and D10 Transition Metal Complexes. *Chem. Rev.* **2015**, *115*, 7589-7728.

68. Wang, Q.; Dong, S.-L.; Tao, D.-D.; Li, Z.; Jiang, Y.-B., Ag (I)-Thiolate Coordination Polymers: Synthesis, Structures and Applications as Emerging Sensory Ensembles. *Coord. Chem. Rev.* **2020**, 213717.

69. Bell, R. A.; Kramer, J. R., Structural Chemistry and Geochemistry of Silver-Sulfur Compounds: Critical Review. *Environ. Toxicol. Chem.* **1999**, *18*, 9-22.

70. Li, M.-Q.; Zhao, M.; Bi, L.-Y.; Hu, Y.-Q.; Gou, G.; Li, J.; Zheng, Y.-Z., Two-Dimensional Silver (I)-Dithiocarboxylate Coordination Polymer Exhibiting Strong near-Infrared Photothermal Effect. *Inorg. Chem.* **2019**, *58*, 6601-6608.

71. Dance, I. G.; Fisher, K. J.; Banda, R. H.; Scudder, M. L., Layered Structure of Crystalline Compounds Silver Thiolates (Agsr). *Inorg. Chem.* **1991**, *30*, 183-187.

72. Veselska, O.; Dessal, C.; Melizi, S.; Guillou, N.; Podbevšek, D.; Ledoux, G.; Elkaim, E.; Fateeva, A.; Demessence, A., New Lamellar Silver Thiolate Coordination Polymers with Tunable Photoluminescence Energies by Metal Substitution. *Inorg. Chem.* **2018**, *58*, 99-105.

73. Chen, Y.-B.; Chen, L.; Wu, L.-M., Structure-Controlled Solventless Thermolytic Synthesis of Uniform Silver Nanodisks. *Inorg. Chem.* **2005**, *44*, 9817-9822.

74. Vogler, A.; Kunkely, H., Charge Transfer Excitation of Coordination Compounds. Generation of Reactive Intermediates: In *Photosensitization and Photocatalysis Using Inorganic and Organometallic Compounds*, *Springer*: **1993;** pp 71-111.

75. Sabin, F.; Ryu, C.; Ford, P.; Vogler, A., Photophysical Properties of Hexanuclear Copper (I) and Silver (I) Clusters. *Inorg. Chem.* **1992**, *31*, 1941-1945.

76. Jones, W. B.; Yuan, B. J.; Narayanaswamy, R.; Young, M. A.; Elder, R.; Bruce, A. E.; Bruce, M. R., Solid State Exafs and Luminescence Studies of Neutral, Dinuclear Gold (I) Complexes. Gold (I)-Gold (I) Interactions in the Solid State. *Inorg. Chem.* **1995**, *34*, 1996-2001.

77. Wang, C.-R.; Lo, K. K.-W.; Yam, V. W.-W., Ab Initio Study of Luminescent Chalcogenido Silver (I) Clusters [Ag4 (M-H2pch2ph2) 4 (M4-E)] 2+. *Chem. Phys. Lett.* **1996**, *262*, 91-96.

78. Yam, V. W.-W.; Lo, K. K.-W.; Wang, C.-R.; Cheung, K.-K., The First Series of Luminescent (M4-Chalcogenido) Silver (I) Clusters. *Inorg. Chem.* **1996**, *35*, 5116-5117.

79. Wang, C.-R.; Lo, K. K.-W.; Yam, V. W.-W., Molecular Orbital Studies of Luminescent Silver (I) Chalcogenido Clusters [Ag 4 (μ-Dppm) 4 (μ 4-E)] 2+(Dppm= Ph 2 Pch 2 Pph 2). *Journal of the Chemical Society, Dalton Trans.* **1997**, 227-230.

80. Raju, S.; Singh, H. B.; Butcher, R. J., Metallophilic Interactions: Observations of the Shortest Metallophilicinteractions between Closed Shell (D $10^{\cdots}$ D 10, D $10^{\cdots}$ D 8, D $8^{\cdots}$ D 8) Metal Ions [M$^{\cdots}$ M′ M= Hg (Ii) and Pd (Ii) and M′= Cu (I), Ag (I), Au (I), and Pd (Ii)]. *Dalton Trans.* **2020**, *49*, 9099-9117.

81. Hunks, W. J.; Jennings, M. C.; Puddephatt, R. J., Supramolecular Gold (I) Thiobarbiturate Chemistry: Combining Aurophilicity and Hydrogen Bonding to Make Polymers, Sheets, and Networks. *Inorg. Chem.* **2002**, *41*, 4590-4598.

82. Pyykkö, P., Strong Closed-Shell Interactions in Inorganic Chemistry. *Chem. rev.* **1997**, *97*, 597-636.

83. Wheaton, C. A.; Jennings, M. C.; Puddephatt, R. J., Complexes of Gold (I) with a Chiral Diphosphine Ligand: A Polymer with Both Au⋯ Ag and Ag⋯ Ag Metallophilic Bonds. *Z Naturforsch B* **2009**, *64*, 1469-1477.

84. Jansen, M., Homoatomic D10–D10 Interactions: Their Effects on Structure and Chemical and Physical Properties. *Angew. Chem. Int. Ed.* **1987**, *26*, 1098-1110.

85. Attenberger, B.; El Sayed Moussa, M.; Brietzke, T.; Vreshch, V.; Holdt, H. J.; Lescop, C.; Scheer, M., Discrete Polymetallic Arrangements of Agi and Cui Ions Based on Multiple

Bridging Phosphane Ligands and Π–Π Interactions. *Eur. J. Inorg. Chem.* **2015**, *2015*, 2934-2938.

86. Kim, M.; Taylor, T. J.; Gabbaï, F. P., Hg (Ii)⋯ Pd (Ii) Metallophilic Interactions. *J. Am. Chem. Soc.* **2008**, *130*, 6332-6333.

87. Zheng, Q.; Borsley, S.; Nichol, G. S.; Duarte, F.; Cockroft, S. L., The Energetic Significance of Metallophilic Interactions. *Angew. Chem. Int. Ed.* **2019**, *58*, 12617-12623.

88. Schmidbaur, H.; Schier, A., Argentophilic Interactions. *Angew. Chem. Int. Ed.* **2015**, *54*, 746-784.

89. Che, C.-M.; Tse, M.-C.; Chan, M. C.; Cheung, K.-K.; Phillips, D. L.; Leung, K.-H., Spectroscopic Evidence for Argentophilicity in Structurally Characterized Luminescent Binuclear Silver (I) Complexes. *J. Am. Chem. Soc.* **2000**, *122*, 2464-2468.

90. Huang, R.-W.; Zhu, Y.; Zang, S.-Q.; Zhang, M.-L., Construction of Silver–Organic Framework with Silver Rods of Repeated Ag-Triangle Units: Synthesis, Structure, and Properties. *Inorg. Chem. Commun.* **2013**, *33*, 38-42.

91. Su, Z.; Bai, Z.-S.; Fan, J.; Xu, J.; Sun, W.-Y., Synthesis and Characterization of 3d-3d Homo-and Heterometallic Coordination Polymers with Mixed Ligands. *Cryst. Growth Des.* **2009**, *9*, 5190-5196.

92. Rawashdeh-Omary, M. A.; Omary, M. A.; Patterson, H. H., Oligomerization of Au (Cn) 2-and Ag (Cn) 2-Ions in Solution Via Ground-State Aurophilic and Argentophilic Bonding. *J. Am. Chem. Soc.* **2000**, *122*, 10371-10380.

93. Omary, M. A.; Hall, D. R.; Shankle, G. E.; Siemiarczuk, A.; Patterson, H. H., Luminescent Homoatomic Exciplexes in Dicyanoargentate (I) Ions Doped in Alkali Halide Crystals. 2."Exciplex Tuning" by Varying the Dopant Concentration. *J. Phys. Chem. B* **1999**, *103*, 3845-3853.

94. Omary, M. A.; Patterson, H. H., Luminescent Homoatomic Exciplexes in Dicyanoargentate (I) Ions Doped in Alkali Halide Crystals. 1."Exciplex Tuning" by Site-Selective Excitation. *J. Am. Chem. Soc.* **1998**, *120*, 7696-7705.

95. Omary, M. A.; Patterson, H. H., Temperature-Dependent Photoluminescence Properties of Tl [Ag (Cn) 2]: Formation of Luminescent Metal− Metal-Bonded Inorganic Exciplexes in the Solid State. *Inorg. Chem.* **1998**, *37*, 1060-1066.

96. Almdal, K.; Dyre, J.; Hvidt, S.; Kramer, O., Towards a Phenomenological Definition of the Term 'Gel'. *Polym. gels netw.* **1993**, *1*, 5-17.

97. Sutar, P.; Maji, T. K., Coordination Polymer Gels: Soft Metal–Organic Supramolecular Materials and Versatile Applications. *Chem. Commun.* **2016**, *52*, 8055-8074.

98. Estroff, L. A.; Hamilton, A. D., Water Gelation by Small Organic Molecules. *Chem.l rev.* **2004**, *104*, 1201-1218.

99. Zhang, J.; Hu, Y.; Li, Y., *Gel Chemistry: Interactions, Structures and Properties*; *Springer*, **2018**; Vol. 96.

100. Chakma, P.; Konkolewicz, D., Dynamic Covalent Bonds in Polymeric Materials. *Angew. Chem. Int. Ed.* **2019**, *131*, 9784-9797.

101. Li, Z.-T.; Wu, L.-Z., Hydrogen Bonded Supramolecular Materials; *Springer*, 2015; Vol. 88.

102. Chivers, P. R.; Smith, D. K., Shaping and Structuring Supramolecular Gels. *Nat. Rev. Mater.* **2019**, *4*, 463-478.

103. Tam, A. Y.-Y.; Yam, V. W.-W., Recent Advances in Metallogels. *Chem. Soc. Rev.* **2013**, *42*, 1540-1567.

104. Wang, H.; Zhang, W.; Dong, X.; Yang, Y., Thermo-Reversibility of the Fluorescence Enhancement of Acridine Orange Induced by Supramolecular Self-Assembly. *Talanta* **2009**, *77*, 1864-1868.

105. Yu, X.; Chen, L.; Zhang, M.; Yi, T., Low-Molecular-Mass Gels Responding to Ultrasound and Mechanical Stress: Towards Self-Healing Materials. *Chem. Soc. Rev.* **2014**, *43*, 5346-5371.

106. Duan, P.; Yanai, N.; Nagatomi, H.; Kimizuka, N., Photon Upconversion in Supramolecular Gel Matrixes: Spontaneous Accumulation of Light-Harvesting Donor–Acceptor Arrays in Nanofibers and Acquired Air Stability. *J. Am. Chem. Soc.* **2015**, *137*, 1887-1894.

107. Zhang, S.; Bellinger, A. M.; Glettig, D. L.; Barman, R.; Lee, Y.-A. L.; Zhu, J.; Cleveland, C.; Montgomery, V. A.; Gu, L.; Nash, L. D., A Ph-Responsive Supramolecular Polymer Gel as an Enteric Elastomer for Use in Gastric Devices. *Nat. mater.* **2015**, *14*, 1065-1071.

108. Liu, Q.; Wang, Y.; Li, W.; Wu, L., Structural Characterization and Chemical Response of a Ag-Coordinated Supramolecular Gel. *Langmuir* **2007**, *23*, 8217-8223.

109. He, P.; Liu, J.; Liu, K.; Ding, L.; Yan, J.; Gao, D.; Fang, Y., Preparation of Novel Organometallic Derivatives of Cholesterol and Their Gel-Formation Properties. *Colloids Surf. A Physicochem. Eng. Asp.* **2010**, *362*, 127-134.

110. Pauling, L., *The Nature of the Chemical Bond*; Cornell university press Ithaca, *NY*, **1960;** Vol. 260.

111. Moore, T. S.; Winmill, T. F., Clxxvii.—the State of Amines in Aqueous Solution. *J. Chem. Soc., Trans.* **1912**, *101*, 1635-1676.

112. Li, Y.; Zhou, F.; Wen, Y.; Liu, K.; Chen, L.; Mao, Y.; Yang, S.; Yi, T., (−)-Menthol Based Thixotropic Hydrogel and Its Application as a Universal Antibacterial Carrier. *Soft Matter* **2014**, *10*, 3077-3085.

113. Piepenbrock, M.; Clarke, N.; Steed, J. W., Metal Ion and Anion-Based "Tuning" of a Supramolecular Metallogel. *Langmuir* **2009**, *25*, 8451-8456.

114. Shen, J.-S.; Li, D.-H.; Cai, Q.-G.; Jiang, Y.-B., Highly Selective Iodide-Responsive Gel–Sol State Transition in Supramolecular Hydrogels. *J. Am. Chem. Soc.* **2009**, *19*, 6219-6224.

115. Hao, L.; Mansour, M. A.; Lachicotte, R. J.; Gysling, H. J.; Eisenberg, R., A Gold (I) Mononuclear Complex and Its Association into Binuclear and Cluster Compounds by Hydrogen Bonding or Metal Ion Coordination. *Inorg. Chem.* **2000**, *39*, 5520-5529.

116. Sillen, L. G.; Martell, A., Stability Constants of Metal-Ion Complexes. Section I: Inorganic Ligands. *Special publication* **1964**.

117. Adams, N. W.; Kramer, J. R., Potentiometric Determination of Silver Thiolate Formation Constants Using a Ag2s Electrode. *Aquat. Geochem.* **1999**, *5*, 1-11.

118. Kishimura, A.; Yamashita, T.; Aida, T., Phosphorescent Organogels Via "Metallophilic" Interactions for Reversible Rgb− Color Switching. *J. Am. Chem. Soc.* **2005**, *127*, 179-183.

119. Tubbs, R. K., Sequence Distribution of Partially Hydrolyzed Poly (Vinyl Acetate). *J. Polym. Sci. A Polym. Chem.* **1966**, *4*, 623-629.

120. Mansur, H. S.; Sadahira, C. M.; Souza, A. N.; Mansur, A. A., Ftir Spectroscopy Characterization of Poly (Vinyl Alcohol) Hydrogel with Different Hydrolysis Degree and Chemically Crosslinked with Glutaraldehyde. *Mater. Sci. Eng. C* **2008**, *28*, 539-548.

121. Bo, J., Study on Pva Hydrogel Crosslinked by Epichlorohydrin. *J. Appl. Polym. Sci.* **1992**, *46*, 783-786.

122. Zheng, C.; Liu, C.; Chen, H.; Wang, N.; Liu, X.; Sun, G.; Qiao, W., Effective Wound Dressing Based on Poly (Vinyl Alcohol)/Dextran-Aldehyde Composite Hydrogel. *Int. J. Biol. Macromol.* **2019**, *132*, 1098-1105.

123. Mondino, A.; Gonzalez, M.; Romero, G.; Smolko, E., Physical Properties of Gamma Irradiated Poly (Vinyl Alcohol) Hydrogel Preparations. *Radiat. Phys. Chem.* **1999**, *55*, 723-726.

124. Kumar, A.; Han, S. S., Pva-Based Hydrogels for Tissue Engineering: A Review. *Int. J. Polym. Mater.* **2017**, *66*, 159-182.

125. Song, K.; Zhu, W.; Li, X.; Yu, Z., A Novel Mechanical Robust, Self-Healing and Shape Memory Hydrogel Based on Pva Reinforced by Cellulose Nanocrystal. *Mater. Lett.* **2020**, *260*, 126884.

126. Wang, T.; Gunasekaran, S., State of Water in Chitosan–Pva Hydrogel. *J. Appl. Polym. Sci.* **2006**, *101*, 3227-3232.

127. Yang, J. M.; Chiu, H. C., Preparation and Characterization of Polyvinyl Alcohol/Chitosan Blended Membrane for Alkaline Direct Methanol Fuel Cells. *J. Membr. Sci.* **2012**, *419*, 65-71.

128. Hassan, C. M.; Peppas, N. A., Structure and Applications of Poly (Vinyl Alcohol) Hydrogels Produced by Conventional Crosslinking or by Freezing/Thawing Methods. *springer* **2000**, 37-65.

129. Peppas, N. A., Turbidimetric Studies of Aqueous Poly (Vinyl Alcohol) Solutions. *Makromol. Chem.* **1975**, *176*, 3433-3440.

130. Zhang, L.; Zhao, J.; Zhu, J.; He, C.; Wang, H., Anisotropic Tough Poly (Vinyl Alcohol) Hydrogels. *Soft Matter* **2012**, *8*, 10439-10447.

131. Holloway, J. L.; Lowman, A. M.; Palmese, G. R., The Role of Crystallization and Phase Separation in the Formation of Physically Cross-Linked Pva Hydrogels. *Soft Matter* **2013**, *9*, 826-833.

132. Bunn, C., Crystal Structure of Polyvinyl Alcohol. *Nature* **1948**, *161*, 929-930.

133. Yokoyama, F.; Masada, I.; Shimamura, K.; Ikawa, T.; Monobe, K., Morphology and Structure of Highly Elastic Poly (Vinyl Alcohol) Hydrogel Prepared by Repeated Freezing-and-Melting. *Colloid. Polym. Sci.* **1986**, *264*, 595-601.

134. Wu, S.; Hua, M.; Alsaid, Y.; Du, Y.; Ma, Y.; Zhao, Y.; Lo, C. Y.; Wang, C.; Wu, D.; Yao, B., Poly (Vinyl Alcohol) Hydrogels with Broad-Range Tunable Mechanical Properties Via the Hofmeister Effect. *Adv. Mater.* **2021**, *33*, 2007829.

135. Jungwirth, P.; Cremer, P. S., Beyond Hofmeister. *Nat. Chem.* **2014**, *6*, 261-263.

136. Hua, M.; Wu, S.; Ma, Y.; Zhao, Y.; Chen, Z.; Frenkel, I.; Strzalka, J.; Zhou, H.; Zhu, X.; He, X., Strong Tough Hydrogels Via the Synergy of Freeze-Casting and Salting Out. *Nature* **2021**, *590*, 594-599.

137. Li, J.; Suo, Z.; Vlassak, J. J., Stiff, Strong, and Tough Hydrogels with Good Chemical Stability. *J. Mater. Chem. B* **2014**, *2*, 6708-6713.

138. Fukunaga, K.; Hosako, I.; Duling, I.; Picollo, M., Terahertz Imaging Systems: A Non-Invasive Technique for the Analysis of Paintings; *SPIE*, **2009**; Vol. 7391.

139. Sirtori, C., Bridge for the Terahertz Gap. *Nature* **2002**, *417*, 132-133.

140. Auston, D. H.; Cheung, K. P.; Smith, P. R., Picosecond Photoconducting Hertzian Dipoles. *Appl. Phys. Lett.* **1984**, *45*, 284-286.

141. Fattinger, C.; Grischkowsky, D., Terahertz Beams. *Appl. Phys. Lett.* **1989**, *54*, 490-492.

142. Van Exter, M.; Fattinger, C.; Grischkowsky, D., High-Brightness Terahertz Beams Characterized with an Ultrafast Detector. *Appl. Phys. Lett.* **1989**, *55*, 337-339.

143. DeFonzo, A. P.; Jarwala, M.; Lutz, C., Transient Response of Planar Integrated Optoelectronic Antennas. *Appl. Phys. Lett.* **1987**, *50*, 1155-1157.

144. DeFonzo, A. P.; Lutz, C. R., Optoelectronic Transmission and Reception of Ultrashort Electrical Pulses. *Appl. Phys. Lett.* **1987**, *51*, 212-214.

145. Smith, P. R.; Auston, D. H.; Nuss, M. C., Subpicosecond Photoconducting Dipole Antennas. *IEEE J. Quantum Electron.* **1988**, *24*, 255-260.

146. Andrejewski, J.; De Marco, F.; Willer, K.; Noichl, W.; Gustschin, A.; Koehler, T.; Meyer, P.; Kriner, F.; Fischer, F.; Braun, C., Whole-Body X-Ray Dark-Field Radiography of a Human Cadaver. *Eur. Radiol. Exp.* **2021**, *5*, 1-9.

147. Ulbricht, R.; Hendry, E.; Shan, J.; Heinz, T. F.; Bonn, M., Carrier Dynamics in Semiconductors Studied with Time-Resolved Terahertz Spectroscopy. *Rev. Mod. Phys.* **2011**, *83*, 543.

148. Wehrenfennig, C.; Eperon, G. E.; Johnston, M. B.; Snaith, H. J.; Herz, L. M., High Charge Carrier Mobilities and Lifetimes in Organolead Trihalide Perovskites. *Adv. Mater.* **2014**, *26*, 1584-1589.

149. Wang, H. Ultrafast Carrier Dynamics in Quantum Dot Sensitized Systems. *Johannes Gutenberg-Universität Mainz*, **2016**.

150. Nienhuys, H.-K.; Sundström, V., Intrinsic Complications in the Analysis of Optical-Pump, Terahertz Probe Experiments. *Phy. Rev. B* **2005**, *71*, 235110.

151. Baskoutas, S.; Terzis, A. F., Size-Dependent Band Gap of Colloidal Quantum Dots. *J. Appl. Phys.* **2006**, *99*, 013708.

152. Dai, X.; Deng, Y.; Peng, X.; Jin, Y., Quantum-Dot Light-Emitting Diodes for Large-Area Displays: Towards the Dawn of Commercialization. *Adv. Mater.* **2017**, *29*, 1607022.

153. Zhang, Y.; Hong, G.; Zhang, Y.; Chen, G.; Li, F.; Dai, H.; Wang, Q., Ag2s Quantum Dot: A Bright and Biocompatible Fluorescent Nanoprobe in the Second near-Infrared Window. *ACS nano* **2012**, *6*, 3695-3702.

154. Gui, R.; Wan, A.; Liu, X.; Yuan, W.; Jin, H., Retracted Article: Water-Soluble Multidentate Polymers Compactly Coating Ag2s Quantum Dots with Minimized Hydrodynamic Size and Bright Emission Tunable from Red to Second near-Infrared Region. *Nanoscale* **2014**, *6*, 5467-5473.

155. Chen, G.; Tian, F.; Zhang, Y.; Zhang, Y.; Li, C.; Wang, Q., Tracking of Transplanted Human Mesenchymal Stem Cells in Living Mice Using near-Infrared Ag2s Quantum Dots. *Adv. Funct. Mater.* **2014**, *24*, 2481-2488.

156. Tan, L.; Wan, A.; Li, H., Conjugating S-Nitrosothiols with Glutathiose Stabilized Silver Sulfide Quantum Dots for Controlled Nitric Oxide Release and near-Infrared Fluorescence Imaging. *ACS Appl. Mater. Interfaces* **2013**, *5*, 11163-11171.

157. Aydemir, D.; Hashemkhani, M.; Acar, H. Y.; Ulusu, N. N., In Vitro Interaction of Glutathione S-Transferase-Pi Enzyme with Glutathione-Coated Silver Sulfide Quantum Dots: A Novel Method for Biodetection of Glutathione S-Transferase Enzyme. *Chem. Biol. Drug. Des.* **2019**, *94*, 2094-2102.

158. Jiang, P.; Zhu, C. N.; Zhang, Z. L.; Tian, Z. Q.; Pang, D. W., Water-Soluble Ag(2)S Quantum Dots for near-Infrared Fluorescence Imaging in Vivo. *Biomaterials* **2012**, *33*, 5130-5.

159. Kubie, L.; King, L. A.; Kern, M. E.; Murphy, J. R.; Kattel, S.; Yang, Q.; Stecher, J. T.; Rice, W. D.; Parkinson, B. A., Synthesis and Characterization of Ultrathin Silver Sulfide Nanoplatelets. *ACS Nano* **2017**, *11*, 8471-8477.

160. Kubie, L.; Martinez, M. S.; Miller, E. M.; Wheeler, L. M.; Beard, M. C., Atomically Thin Metal Sulfides. *J Am Chem Soc* **2019**, *141*, 12121-12127.

161. Yu, W.; Yin, J.; Li, Y.; Lai, B.l Jiang, T.; Li, Y., Ag2S Quantum Dots as an Infrared Excited Photocatalyst for Hydrogen Production. *ACS Appl. Energy Mater.* **2019**, *2*, 2751-2759.

162. Sadovnikov, S.; Gusev, A., Recent Progress in Nanostructured Silver Sulfide: From Synthesis and Nonstoichiometry to Properties. *J. Mater. Chem. A* **2017**, *5*, 17676-17704.

163. Vinod Chandran, C.; Madhu, P.; Kurur, N. D.; Bräuniger, T., Swept-Frequency Two-Pulse Phase Modulation (Swf-Tppm) Sequences with Linear Sweep Profile for Heteronuclear Decoupling in Solid-State Nmr. *Magn. Reson. Chem.* **2008**, *46*, 943-947.

164. Bielecki, A.; Burum, D. P., Temperature Dependence Of207pb Mas Spectra of Solid Lead Nitrate. An Accurate, Sensitive Thermometer for Variable-Temperature Mas. *J. magn. reson., Ser. A* **1995**, *116*, 215-220.

165. Guan, X.; Stark, R. E., A General Protocol for Temperature Calibration of Mas Nmr Probes at Arbitrary Spinning Speeds. *Solid State Nucl. Magn. Reson.* **2010**, *38*, 74-76.

166. Ye, Z.; Lito, P.; Efremov, M. Y.; Zuo, J.-M.; Allen, L. H., Approaching the Size Limit of Organometallic Layers: Synthesis and Characterization of Highly Ordered Silver–Thiolate Lamellae with Ultra-Short Chain Lengths. *Dalton Trans.* **2016**, *45*, 18954-18966.

167. Duan, J.; Ma, J.; Wu, B.; Li, Q.; Fang, J.; Chen, D., Formation of Persistent Ordered Lamellar Mesophases in Azobenzene-Containing Silver Thiolates and Their Application in the Controlled Synthesis of Silver Nanomaterials. *J. Mater. Chem. C* **2014**, *2*, 2375-2386.

168. Gwak, G.-H.; Kim, M.-K.; Lee, W.-J.; Jeung, D.-G.; Park, J. K.; Paek, S.-M.; Oh, J.-M., Facile Synthetic Route to Prepare Ultrathin Silver Nanosheets by Reducing Silver Thiolates in Interlayer Surface of Layered Double Hydroxides. *Inorg. Chem.* **2019**, *59*, 2163-2170.

169. Veselska, O.; Dessal, C.; Melizi, S.; Guillou, N.; Podbevšek, D.; Ledoux, G.; Elkaim, E.; Fateeva, A.; Demessence, A., New Lamellar Silver Thiolate Coordination Polymers with Tunable Photoluminescence Energies by Metal Substitution. *Inorg. Chem.* **2019**, *58*, 99-105.

170. Li, Y.; Jiang, X.; Fu, Z.; Huang, Q.; Wang, G.-E.; Deng, W.-H.; Wang, C.; Li, Z.; Yin, W.; Chen, B., Coordination Assembly of 2d Ordered Organic Metal Chalcogenides with Widely Tunable Electronic Band Gaps. *Nat. Commun.* **2020**, *11*, 1-9.

171. Beers, J.; Parikh, A.; Gillmor, S.; Beardmore, K.; Cutts, R.; Swanson, B., Stepwise Assembly of Silver (N-Alkane) Thiolates: An Example of Hierarchical or Cooperative Self-Assembly. *J. Young Investig.* **1998**.

172. Saalwächter, K.; Lange, F.; Matyjaszewski, K.; Huang, C.-F.; Graf, R., Baba-Xy16: Robust and Broadband Homonuclear Dq Recoupling for Applications in Rigid and Soft Solids up to the Highest Mas Frequencies. *J. Magn. Reson.* **2011**, *212*, 204-215.

173. Khizhnyak, S. D.; Komarov, P. V.; Ovchinnikov, M. M.; Zherenkova, L. V.; Pakhomov, P. M., Mechanism of Gelation in Low-Concentration Aqueous Solutions of Silver Nitrate with L-Cysteine and Its Derivatives. *Soft matter* **2017**, *13*, 5168-5184.

174. Casuso, P.; Carrasco, P.; Loinaz, I.; Grande, H. J.; Odriozola, I., Converting Drugs into Gelators: Supramolecular Hydrogels from N-Acetyl-L-Cysteine and Coinage-Metal Salts. *Org. Biomol. Chem.* **2010**, *8*, 5455-5458.

175. Heister, K.; Zharnikov, M.; Grunze, M.; Johansson, L., Adsorption of Alkanethiols and Biphenylthiols on Au and Ag Substrates: A High-Resolution X-Ray Photoelectron Spectroscopy Study. *J. Phys. Chem. B* **2001**, *105*, 4058-4061.

176. Kaushik, V. K., Xps Core Level Spectra and Auger Parameters for Some Silver Compounds. *J. Electron Spectrosc. Relat. Phenom.* **1991**, *56*, 273-277.

177. Battocchio, C.; Meneghini, C.; Fratoddi, I.; Venditti, I.; Russo, M. V.; Aquilanti, G.; Maurizio, C.; Bondino, F.; Matassa, R.; Rossi, M., Silver Nanoparticles Stabilized with Thiols: A Close Look at the Local Chemistry and Chemical Structure. *J. Phys. Chem. C* **2012**, *116*, 19571-19578.

178. Rabchinskii, M. K.; Dideikin, A. T.; Kirilenko, D. A.; Baidakova, M. V.; Shnitov, V. V.; Roth, F.; Konyakhin, S. V.; Besedina, N. A.; Pavlov, S. I.; Kuricyn, R. A., Facile Reduction of Graphene Oxide Suspensions and Films Using Glass Wafers. *Sci. Rep.* **2018**, *8*, 1-11.

179. Dietrich, P. M.; Horlacher, T.; Girard-Lauriault, P.-L.; Gross, T.; Lippitz, A.; Min, H.; Wirth, T.; Castelli, R.; Seeberger, P.; Unger, W. E., Multimethod Chemical Characterization of Carbohydrate-Functionalized Surfaces. *J. Carbohydr. Chem.* **2011**, *30*, 361-372.

180. Sangeetha, N. M.; Maitra, U., Supramolecular Gels: Functions and Uses. *Chem. Soc. Rev.* **2005**, *34*, 821-836.

181. Cao, X.; Gao, A.; Hou, J.-t.; Yi, T., Fluorescent Supramolecular Self-Assembly Gels and Their Application as Sensors: A Review. *Coord. Chem. Rev.* **2021**, *434*, 213792.

182. Kawano, S.-i.; Fujita, N.; Shinkai, S., A Coordination Gelator That Shows a Reversible Chromatic Change and Sol− Gel Phase-Transition Behavior Upon Oxidative/Reductive Stimuli. *J. Am. Chem. Soc.* **2004**, *126*, 8592-8593.

183. Zhang, S.; Yang, S.; Lan, J.; Yang, S.; You, J., Helical Nonracemic Tubular Coordination Polymer Gelators from Simple Achiral Molecules. *Chem. Commun.* **2008**, 6170-6172.

184. Au, V. K.-M.; Zhu, N.; Yam, V. W.-W., Luminescent Metallogels of Bis-Cyclometalated Alkynylgold(Iii) Complexes. *Inorg. Chem.* **2013**, *52*, 558-567.

185. Su, C.-Y.; Cai, Y.-P.; Chen, C.-L.; Smith, M. D.; Kaim, W.; zur Loye, H.-C., Ligand-Directed Molecular Architectures: Self-Assembly of Two-Dimensional Rectangular

Metallacycles and Three-Dimensional Trigonal or Tetragonal Prisms. *J. Am. Chem. Soc.* **2003**, *125*, 8595-8613.

186. Sun, D.; Cao, R.; Bi, W.; Li, X.; Wang, Y.; Hong, M., Self-Assembly of Novel Silver Polymers Based on Flexible Sulfonate Ligands. *Eur. J. Inorg. Chem.* **2004**, *2004*, 2144-2150.

187. Dong, Y.-B.; Zhao, X.; Huang, R.-Q.; Smith, M. D.; zur Loye, H.-C., New Ag (I)-Containing Coordination Polymers Generated from Multidentate Schiff-Base Ligands. *Inorg. Chem.* **2004**, *43*, 5603-5612.

188. Chen, C.-L.; Su, C.-Y.; Cai, Y.-P.; Zhang, H.-X.; Xu, A.-W.; Kang, B.-S.; Zur Loye, H.-C., Multidimensional Frameworks Assembled from Silver (I) Coordination Polymers Containing Flexible Bis (Thioquinolyl) Ligands: Role of the Intra-and Intermolecular Aromatic Stacking Interactions. *Inorg. Chem.* **2003**, *42*, 3738-3750.

189. Carlucci, L.; Ciani, G.; Porta, F.; Proserpio, D. M.; Santagostini, L., Crystal Engineering of Mixed-Metal Ru–Ag Coordination Networks by Using the Trans-[Rucl2 (Pyz) 4](Pyz= Pyrazine) Building Block. *Angew. Chem. Int. Ed.* **2002**, *41*, 1907-1911.

190. Chen, W.; Chen, H.; Zheng, D.; Zhang, H.; Deng, L.; Cui, W.; Zhang, Y.; Santos, H. A.; Shen, H., Gene-Hydrogel Microenvironment Regulates Extracellular Matrix Metabolism Balance in Nucleus Pulposus. *Adv. Sci.* **2020**, *7*, 1902099.

191. Fromm, K. M., Give Silver a Shine. *Nat. Chem.* **2011**, *3*, 178-178.

192. del Rosal, B.; Benayas, A., Strategies to Overcome Autofluorescence in Nanoprobe-Driven in Vivo Fluorescence Imaging. *Small Methods* **2018**, *2*, 1800075.

193. Jin, T.; Huang, C.; Cui, M.; Yang, Y.; Wang, Z.; Zhu, W.; Qian, X., Supramolecular Ensembles Modified by near-Infrared Dyes and Their Biological Applications. *J. Mater. Chem. B* **2020**, *8*, 10686-10699.

194. Liu, Y.; Li, F.; Guo, Z.; Xiao, Y.; Zhang, Y.; Sun, X.; Zhe, T.; Cao, Y.; Wang, L.; Lu, Q., Silver Nanoparticle-Embedded Hydrogel as a Photothermal Platform for Combating Bacterial Infections. *Chem. Eng. J.* **2020**, *382*, 122990.

195. Yu, G.; Yan, X.; Han, C.; Huang, F., Characterization of Supramolecular Gels. *Chem. Soc. Rev.* **2013**, *42*, 6697-6722.

196. Yao, X.; Wang, J.; Jiao, D.; Huang, Z.;Mhirsl, O.; Lossada, F., Room-Temperature Phosphorescence Enabled through Nacre-Mimetic Nanocomposite Design. *Adv. Mater.* **2021**, *33*, 2005973.

197. Lake, G.; Thomas, A., The Strength of Highly Elastic Materials. *Proc. R. Soc. Lond., A Math. phys. sci.* **1967**, *300*, 108-119.

198. Kysar, J. W., Energy Dissipation Mechanisms in Ductile Fracture. *J. Mech. Phys.* **2003**, *51*, 795-824.

199. Lee, K. Y.; Mooney, D. J., Hydrogels for Tissue Engineering. *Chem. rev.* **2001**, *101*, 1869-1880.

200. Calvert, P., Hydrogels for Soft Machines. *Adv.Mater.* **2009**, *21*, 743-756.

201. Hwang, I.; Seol, M.; Kim, H.; Yong, K., Improvement of Photocurrent Generation of Ag2s Sensitized Solar Cell through Co-Sensitization with Cds. *Appl. Phys. Lett.* **2013**, *103*, 023902.

202. Wang, D.; Hao, C.; Zheng, W.; Peng, Q.; Wang, T.; Liao, Z.; Yu, D.; Li, Y., Ultralong Single-Crystalline Ag2s Nanowires: Promising Candidates for Photoswitches and Room-Temperature Oxygen Sensors. *Adv. Mater.* **2008**, *20*, 2628-2632.

203. Tretyakov, I.; Shurakov, A.; Perepelitsa, A.; Kaurova, N.; Svyatodukh, S.; Zilberley, T.; Ryabchun, S.; Smirnov, M.; Ovchinnikov, O.; Goltsman, G., Room Temperature Silicon Detector for Ir Range Coated with Ag2s Quantum Dots. *Phys. Status Solidi Rapid Res. Lett.* **2019**, *13*, 1900187.

204. Pathan, H.; Salunkhe, P.; Sankapal, B.; Lokhande, C., Photoelectrochemical Investigation of Ag2s Thin Films Deposited by Silar Method. *Mater. Chem. Phys.* **2001**, *72*, 105-108.

205. Ngoc Nam, H.; Yamada, R.; Okumura, H.; Nguyen, T. Q.; Suzuki, K.; Shinya, H.; Masago, A.; Fukushima, T.; Sato, K., Intrinsic Defect Formation and the Effect of Transition Metal Doping on Transport Properties in a Ductile Thermoelectric Material A-Ag2s: A First-Principles Study. *Phys. Chem. Chem. Phys.* **2021**, *23*, 9773-9784.

206. Fouddad, F. Z.; Hiadsi, S.; Bouzid, L.; Ghrici, Y. F.; Bekhadda, K., Low Temperature Study of the Structural Stability, Electronic and Optical Properties of the Acanthite A-Ag2s: Spin-Orbit Coupling Effects and New Important Ultra-Refraction Property. *Mater. Sci. Semicond. Process.* **2020**, *107*, 104801.

207. Zhou, W.-X.; Wu, D.; Xie, G.; Chen, K.-Q.; Zhang, G., A-Ag2s: A Ductile Thermoelectric Material with High Zt. *ACS Omega* **2020**, *5*, 5796-5804.

208. Yang, S.; Qiu, P.; Chen, L.; Shi, X., Recent Developments in Flexible Thermoelectric Devices. *Small Sci.* **2021**, *1*, 2100005.

209. Li, G.; An, Q.; Morozov, S. I.; Duan, B.; Goddard, W. A.; Zhang, Q.; Zhai, P.; Snyder, G. J., Ductile Deformation Mechanism in Semiconductor A-Ag2s. *NPJ Comput. Mater.* **2018**, *4*, 44.

210. Jo, S.; Cho, S.; Yang, U. J.; Hwang, G.-S.; Baek, S.; Kim, S.-H.; Heo, S. H.; Kim, J.-Y.; Choi, M. K.; Son, J. S., Solution-Processed Stretchable Ag2s Semiconductor Thin Films for Wearable Self-Powered Nonvolatile Memory. *Adv. Mater.* **2021**, *33*, 2100066.

211. Lei, Y.; Gu, L.; Yang, X.; Lin, Y.; Zheng, Z., Ductile-Metal Ag as Buffer Layer for Flexible Self-Powered Ag2s Photodetectors. *Adv. Mater. Interfaces* **2021**, *8*, 2002255.

212. Feng, J.; Li, X.; Shi, Z.; Zheng, C.; Li, X.; Leng, D.; Wang, Y.; Liu, J.; Zhu, L., 2d Ductile Transition Metal Chalcogenides (Tmcs): Novel High-Performance Ag2s Nanosheets for Ultrafast Photonics. *Adv. Opt. Mater.* **2020**, *8*, 1901762.

213. Kaur, J.; Gupta, A.; Pandey, O., Photocatalytic Study of Zns-Ag2s Nanocomposites-Effect of Thioglycerol. *Sol. Energy* **2018**, *176*, 678-687.

214. Krylova, V.; Milbrat, A.; Embrechts, A.; Baltrusaitis, J., Ag2S Deposited on Oxidized Polypropylene as Composite Material for Solar Light Absorption. *Appl. Surf. Sci.* **2014**, *301*, 134-141.

215. Karashanova, D.; Nihtianova, D.; Starbova, K.; Starbov, N., Crystalline Structure and Phase Composition of Epitaxially Grown Ag2s Thin Films. *Solid State Ion.* **2004**, *171*, 269-275.

216. Haefke, H.; Panov, A.; Dimov, V., Thin Film Growth of Silver Sulphide I: Initial Stages of Heteroepitaxy on Nacl. *Thin Solid Films* **1990**, *188*, 133-142.

217. Panneerselvam, A.; Malik, M. A.; O'Brien, P.; Raftery, J., The Cvd of Silver Sulfide and Silver Thin Films from a Homoleptic Crystalline Single-Source Precursor. *J. Mater. Chem* **2008**, *18*, 3264-3269.

218. Dlala, H.; Amlouk, M.; Belgacem, S.; Girard, P.; Barjon, D., Structural and Optical Properties of Ag2s Thin Films Prepared by Spray Pyrolysis. *EPJ Appl. Phys.* **1998**, *2*, 13-16.

219. Guo, X. Y.; Cheng, S. Y.; Lu, P. M.; Zhou, H. F. In Preparation of Ag2s Thin Films by Electro-Deposition, *Mater. Sci. Forum, Trans Tech Publ*: **2011**; pp 910-913.

220. Shen, H.; Jiao, X.; Oron, D.; Li, J.; Lin, H., Efficient Electron Injection in Non-Toxic Silver Sulfide (Ag2s) Sensitized Solar Cells. *J. Power Sources* **2013**, *240*, 8-13.

221. Rodriguez, A. N.; Nair, M.; Nair, P., Structural, Optical and Electrical Properties of Chemically Deposited Silver Sulfide Thin Films. *Semicond. Sci. Technol.* **2005**, *20*, 576.

222. Ezenwa, I.; Okereke, N.; Egwunyenga, N., Optical Properties of Chemical Bath Deposited Ag2s Thin Films. *Int. J. Sci. Technol. Eng.* **2012**, *2*, 101-106.

223. Nozaki, H.; Onoda, M.; Kurashima, K.; Yao, T., Epitaxial Growth of Ag2s Film on Cleaved Surface of Mgo (001). *J. Solid State Chem.* **2001**, *157*, 86-93.

224. Lei, Y.; Jia, H.; He, W.; Zhang, Y.; Mi, L.; Hou, H.; Zhu, G.; Zheng, Z., Hybrid Solar Cells with Outstanding Short-Circuit Currents Based on a Room Temperature Soft-Chemical Strategy: The Case of P3ht:Ag2s. *J. Am. Chem. Soc.* **2012**, *134*, 17392-17395.

225. Chen, C.; Zhai, Y.; Li, F.; Yue, G., Fabrication of Silver Sulfide Thin Films for Efficient Organic Solar Cells with High Short-Circuit Currents Based on Double Heterojunctions. *J. Power Sources* **2015**, *298*, 259-268.

226. Shockley, W.; Queisser, H. J., Detailed Balance Limit of Efficiency of P-N Junction Solar Cells. *J. Appl. Phys.* **1961**, *32*, 510-519.

227. Hall, R. B.; Birkmire, R. W.; Phillips, J. E.; Meakin, J. D., Thin-Film Polycrystalline Cu2s/Cd1-Xznx S Solar Cells of 10% Efficiency. *Appl. Phys. Lett.* **1981**, *38*, 925-926.

228. Sinsermsuksakul, P.; Sun, L.; Lee, S. W.; Park, H. H.; Kim, S. B.; Yang, C.; Gordon, R. G., Overcoming Efficiency Limitations of Sns-Based Solar Cells. *Adv. Energy Mater.* **2014**, *4*, 1400496.

229. Yeon, D. H.; Mohanty, B. C.; Lee, C. Y.; Lee, S. M.; Cho, Y. S., High-Efficiency Double Absorber Pbs/Cds Heterojunction Solar Cells by Enhanced Charge Collection Using a Zno Nanorod Array. *ACS Omega* **2017**, *2*, 4894-4899.

230. Li, S.-L.; Tsukagoshi, K.; Orgiu, E.; Samorì, P., Charge Transport and Mobility Engineering in Two-Dimensional Transition Metal Chalcogenide Semiconductors. *Chem. Soc. Rev.* **2016**, *45*, 118-151.

231. Okamura, K.; Mechau, N.; Nikolova, D.; Hahn, H., Influence of Interface Roughness on the Performance of Nanoparticulate Zinc Oxide Field-Effect Transistors. *Applied Physics Letters* **2008**, *93*, 083105.

232. Lekshmi, I.; Berera, G.; Afsar, Y.; Miao, G.; Nagahama, T.; Santos, T.; Moodera, J., Controlled Synthesis and Characterization of Ag 2 S Films with Varied Microstructures and Its Role as Asymmetric Barrier Layer in Trilayer Junctions with Dissimilar Electrodes. *J. Appl. Phys.* **2008**, *103*, 093719.

233. Ulbricht, R.; Hendry, E.; Shan, J.; Heinz, T. F.; Bonn, M., Carrier Dynamics in Semiconductors Studied with Time-Resolved Terahertz Spectroscopy. *Rev. Mod. Phys.* **2011**, *83*, 543-586.

234. Neu, J.; Regan, K. P.; Swierk, J. R.; Schmuttenmaer, C. A., Applicability of the Thin-Film Approximation in Terahertz Photoconductivity Measurements. *Appl. Phys. Lett.* **2018**, *113*, 233901.

235. Geserich, H. P.; Suppanz, W., Optical Effects of Free Carriers in Thin A-Ag2S Films. *Phys. Status Solidi B Basic Res.* **1969**, *35*, 381-387.

236. Yang, Y.; Yang, M.; Li, Z.; Crisp, R.; Zhu, K.; Beard, M. C., Comparison of Recombination Dynamics in Ch3nh3pbbr3 and Ch3nh3pbi3 Perovskite Films: Influence of Exciton Binding Energy. *The Journal of Physical Chemistry Letters* **2015**, *6*, 4688-4692.

237. Conwell, E.; Weisskopf, V. F., Theory of Impurity Scattering in Semiconductors. *Physical Review* **1950**, *77*, 388-390.